UNIVERSITY OF LIVERPOOL

THE UNIVERSITY *of* LIVERPOOL

Motion Control of Voice Coil Motor Based High Frequency Reciprocating Rig in Tribotest Application

Thesis submitted in accordance with the
requirements of the University of Liverpool
for the degree of Doctor of Philosophy

in

Electrical Engineering and Electronics

by

Ruotong Wang, MSc

April 2020

Motion Control of Voice Coil Motor Based High Frequency Reciprocating Rig in Tribotest Application

by

Ruotong Wang

Acknowledgements

I would like to give my heartfelt thanks to my primary supervisor, Dr Lin Jiang, whose encouragement, guidance and support enabled me to develop a deep understanding of my work. His dynamism, vision, sincerity and motivation have deeply inspired me. He has taught me the methodology to carry out the research and to present the research works as clearly as possible. It was a great privilege and honour to work and study under his guidance. I am extremely grateful for what he has offered me. Without his consistent and illuminating instruction, my research work could not proceed to this stage. I would also like to thank him for his friendship, empathy, and a great sense of humour. I am extending my heartfelt thanks to his wife, family for their acceptance and patience during the discussion I had with him on research work and thesis preparation. The research skill, writing skill and presenting skill he taught me will benefit me throughout my life.

I would like to show my gratitude to my secondary supervisor, Dr Jeremy Smith for his kind guidance and encouragement. I would also like to thank Dr Shiming Liu, Dr Jiarong Kan, Dr Ning Li, Dr Yihua Hu, Dr Roberto Ferrero, Dr Xu Zhu, Prof Yi Huang, Mr Jun Cheng, Mr Xizhen Li and Mr Dalong Xiao for their invaluable advice and emotional support throughout my four-year PhD research, which not only helped me to overcome obstacles in my research, but also boosted my self-confidence and self-esteem when facing the fear of failure.

I offer my regards and blessings to all of the members of smart grid control and renewable energy sub-group, the University of Liverpool. Special thanks also go to my friends and colleagues, Dr Xin Yin, Dr Shuaihu Li, Dr Yaxing Ren, Dr Liuying Li, Dr Kai Shi, Dr Qi Zhu, Dr Shuji Chen, Dr Saqib Jamshed Rind, Dr Yiyan Sang and Dr Haotiao Xu for their support and friendship. Doing a PhD can be a lonely business. However, it was their encouragements that made me feel that I am not alone.

My thanks also go to the Department of Electrical Engineering and Electronics at the University of Liverpool, for providing the research facilities that made it possible for me to carry out this research. Special thanks go to Ms Hannah Fosh, Mrs Alison

Goodyear, Mr Jim Black, Mr David Donaghy, Mrs Jane Williams, Mrs Lindsey Clark, Mr Richard Grant, Mr Jim Humphries and Ms Jill Anson for providing their professional advice and assistance to me during the period of my research.

I am particularly grateful to the incredible staff of NHS who have been standing on the front lines of the nation's battle against coronavirus during the time I am writing this thesis. They share the same fears, uncertainties and anxieties that all of us do. But, they put the safety and well-being of all of us in front of their own.

Finally, I would like to express my deep gratitude to my beloved family for giving me strength and support during these years. My special thanks go to Xiaoyu for being my sunshine through the most dramatic year 2020. You makes the horrible days bearable not only for me, but also for the whole family.

Abstract

Friction and wear are common in manufacturing and transportation applications that lead to considerable losses in economics, of which the impact can be mitigated through the practice of lubrication. That is where tribology as a subject that concentrates on the study of friction, wear and lubrication comes in. A number of tribotest rigs have been introduced to the researches on tribological properties of materials in order to contribute to a good understanding of friction and wear that helps us to make the right choices for materials, contact geometry, motion and chemistry. In this thesis, we focus on the control of high frequency reciprocating rig (HFRR) in the application of pin-on-flat reciprocating tribotest. HFRR as a widely used tribotest rig utilises direct drive linear voice coil motor (VCM) to emulate the reciprocating motion of components in a tribosystem. The main aim of the control of HFRR is to realise some predefined relative reciprocating motions between specimens with lubricant under the impact of frictional force. Due to the complexity of the dynamics of frictional force that exerts directly on VCM, the problem of the control of VCM on HFRR has been challenging and not solved satisfactorily using traditional control methods. The relative error of amplitude obtained by commercial HFRR according to HFRR standard can be more than 30%.

In our study, we investigate the dynamics of HFRR and develop the model of HFRR considering the impact of frictional load on system output. A digital signal processor (DSP) based experimental platform for HFRR is built up for the purpose of verification of control methods. The existing controllers for VCM based HFRR are aimed to track the reference signal with tolerable position error. However, the industrial standard on the operation of HFRR in tribotests states that it is the amplitude and frequency of the reciprocating motion driven by VCM that be regulated

when conducting experiments. To fulfil such requirement, we propose direct amplitude control method to maintain the amplitude of high frequency reciprocating motion of VCM on HFRR subjects to frictional load in tribotest. It takes the error of amplitude rather than the error of position as performance index in the design of the controller. It outperforms PI control in terms of amplitude keeping and harmonics suppression in high frequency reciprocating motion. The relative error of amplitude given by the proposed controller is less than 0.5%.

Furthermore, we consider the frictional load as an external disturbance to HFRR as a plant under control in the view of control system design. To mitigate its effect to the output of the plant, disturbance observer based control techniques are applied to the control system design, which can estimate the lumped input disturbance and compensate it at the input of the plant. To apply disturbance observer techniques to HFRR, acceleration based control is studied and employed to the control of VCM based HFRR. It takes the plant under control as a double integrator by introducing compensation given by a reduced order disturbance observer. It involves the design of a task controller that synthesises the desired system acceleration and the construction of a disturbance compensation module that estimates and compensates for the input disturbance. The acceleration based control outperforms PI control in terms of minimising tracking error.

In addition, it is found that the frictional load that dominates the external disturbances to the VCM on HFRR follows a periodic manner in reciprocating motions. Therefore, internal model disturbance observer that takes the generating model of the input disturbance into account is studied and applied to the control of VCM on HFRR. Compared with classical disturbance observer based control, the internal model disturbance observer based control shows a significant improvement in harmonics suppression of tracking error.

In this thesis, the model of HFRR is presented and aforementioned control methods are discussed and verified through both simulations and experiments using the developed DSP based experimental platform. Suggestions on future study are given in the conclusion chapter.

Declaration

The author hereby declares that this thesis is a record of work carried out in the Department of Electrical Engineering and Electronics at the University of Liverpool during the period from May 2016 to April 2020. The thesis is original in content except where otherwise indicated.

Contents

List of Figures

List of Tables

List of Abbreviations

Abbreviations

AB	Acceleration Based
AC	Alternating Current
AD	Analogue-to-Digital
ADC	Analogue-to-Digital Conversion
ADSFC	Adaptive Dynamic Sliding-mode Fuzzy CMAC
BNPC	B-spline Neural Position Control
CCS	Code Composer Studio
CMAC	Cerebellar Model Articulation Controller
CPU	Central Processing Unit
CRC	Cyclic Redundancy Check
DC	Direct Current
DISO	Dual Input Single Output
DOB	Disturbance Observer
DSP	Digital Signal Processor
ePWM	Enhanced Pulse Width Modulation
eQEP	Enhanced Quadrature Encoder Pulse
FOSMC	Fractional Order Sliding Mode Controller
GPIO	General-Purpose Input/Output
GUI	Graphical User Interface
HDD	Hard Disk Drive
HFRR	High Frequency Reciprocating Rig
IDE	Integrated Development Environment
IM	Internal Model
IMDOB	Internal Model Disturbance Observer
LMI	Linear Matrix Inequality

LuGre	Lund and Grenoble
MIMO	Multiple Input Multiple Output
MOSFET	Metal-Oxide-Semiconductor Field Effect Transistor
MWSD	Mean Wear Scar Diameter
NN	Neural Network
PC	Personal Computer
PCB	Printed Circuit Board
PI	Proportional Integral
PR	Proportional Resonant
PTOS	Proximate Time-Optimal Servomechanism
PWM	Pulse Width Modulation
PZT	Piezoelectric
SCI	Serial Communications Interface
SISO	Single Input Single Output
SMC	Sliding Mode Control
SPI	Serial Peripheral Interface
STFT	Short Time Fourier Transform
THD	Total Harmonics Distortion
TI	Texas Instruments
TMU	Trigonometric Math Unit
USB	Universal Serial Bus
VCM	Voice Coil Motor
VCU	Viterbi, Complex Math, and CRC Unit
WFCMAC	Wavelet Fuzzy Cerebellar Model Articulation Controller

Notations

u_a	VCM terminals voltage
e	counter-Electro-Motive Force
i	current flows into the coil
R	resistance of the equivalent circuit
L	inductance of the equivalent circuit
B	magnetic field flux density
l	total length of the coil
K_s	motor constant
M	total mass of the moving part

k	spring factor
C	damping factor
x	position of motor shaft
F_a	Ampere's force
F_f	friction force
z	average deflection of bristles
v	velocity
σ_0	asperity stiffness of frictional interface
$S(v)$	function of velocity accounts for Stribeck effect
F_c	Coulomb friction force
F_s	Static friction force
v_s	Stribeck velocity
σ_{vs}	shape factor
σ_1	damping coefficient of frictional interface
$F_{bristle}$	component of friction force due to bristle effect
u	controller output
s	complex variable
T	sampling period
$G(s)$	transfer function of continuous system
$G_T(s)$	transfer function of sampled system
ω	angular frequency
$G_{pi}(s)$	transfer function for PI controller
$G_{pr}(s)$	transfer function for PR controller
k_p	proportional gain
k_i	integral gain
u_c	control output by direct amplitude controller
e_a	error of amplitude
s_{ref}	built-in sinusoidal wave generator
k_{pb}	proportional gain of offset regulator module
k_{ib}	integral gain of offset regulator module
x_{dc}	DC component of the output position signal
a_r	desired amplitude of vibration
a	calculated amplitude of output position signal
$w_{TS}(t)$	Hamming window
f_r	desired frequency

$P(s)$	denominator of the transfer function of HFRR without friction
p_1	first pole of the transfer function of HFRR without friction
p_2	second pole of the transfer function of HFRR without friction
p_3	third pole of the transfer function of HFRR without friction
$C(s)$	transfer function of the direct amplitude controller
$E_a(s)$	error of amplitude in s domain
$X_{dc}(s)$	DC component of the output position signal in s domain
$X_{ac}(s)$	AC component of the output position signal in s domain
$X_{dis}(s)$	generalised ouput distubance in s domain
$D(s)$	Equivalent input disturbance in s domain
Δ	equivalent uncertainty of the control input of HFRR
$L_p(s)$	loop transfer function using proportional control
$L_{pr}(s)$	loop transfer function using proportional resonant control
ω_0	angular frequency of the resonant term
F_d	lumped input disturbance with the unit of Newton
$y^{ref}(x, \dot{x})$	reference output function
$y(x, \dot{x})$	output function
$e(x, \dot{x})$	error of the output function
$S(x, \dot{x})$	manifold around equilibrium
c_1	partial derivative of error with respect to position
c_2	partial derivative of error with respect to velocity
$\ddot{x}^{eq}$	equivalent acceleration
F^{eq}	equivalent force
$\dot{e}^{des}$	desired rate of change of the error
$\ddot{x}^{des}$	desired acceleration
$\ddot{x}_e^{des}$	desired exponential acceleration
$\ddot{x}_f^{des}$	desired finite-time acceleration
$\ddot{x}^{con}$	convergence acceleration
$\ddot{x}_e^{con}$	exponential convergence acceleration
$\ddot{x}_f^{con}$	finite-time convergence acceleration
F^{des}	desired control force
F^{con}	convergence control force
V	Lyapunov function
$\lambda(V)$	scalar function of Lyapunov function
$sign$	sign function

K_λ	convergence coefficient
t_{re}	approximate convergence time for exponential convergence
t_{rf}	convergence time for finite-time convergence
α	convergence factor
β	amplitude adjustment factor
ϑ_x	x-th state of the disturbance state space model
F_{dm}	output of the disturbance state space model of $m-1$ order
x_a	measurable state
$\mathbf{x}_b$	unmeasurable state vector
$\hat{\mathbf{x}}_b$	estimated unmeasurable state vector
$\mathbf{A}_{aa}$	submatrix of matrix **A**
$\mathbf{A}_{ab}$	submatrix of matrix **A**
$\mathbf{A}_{ba}$	submatrix of matrix **A**
$\mathbf{A}_{bb}$	submatrix of matrix **A**
$\mathbf{B}_a$	submatrix of matrix **B**
$\mathbf{B}_b$	submatrix of matrix **B**
$\mathbf{L}$	gain matrix of Luenberger-style observer
l_1	element in gain matrix of Luenberger-style observer
l_2	element in gain matrix of Luenberger-style observer
$\mathbf{z}$	intermediate vector for reduced order observer
z_1	element in intermediate vector for reduced order observer
z_2	element in intermediate vector for reduced order observer
F^*	normalised Ampere's force
$\hat{F}_d(s)$	estimated lumped input disturbance with the unit of Newton
$\hat{v}(s)$	estimated velocity of the motor shaft
p_{o1}	first pole of the reduced order observer
p_{o2}	second pole of the reduced order observer
$Q(s)$	transfer function of a low-pass filter
$E_{F_d}(s)$	dynamics of the error of disturbance estimation in s domain
$G_{nd}(s)$	nominal transfer function of the plant in the form of double integrator
$Y(s)$	output of the plant in s domain
$U(s)$	plant input in s domain
$W(s)$	unmeasurable external disturbance
$G_n(s)$	nominal transfer function of the plant
$\Delta G_n(s)$	uncertainty of the plant in s domain

$U_n(s)$	controller output without disturbance compensation
$U_d(s)$	disturbance compensation at plant input
$\hat{D}(s)$	estimated lumped input disturbance
$T_{yr}(s)$	relation between output and reference in s domain
$T_{yd}(s)$	relation between output and disturbance in s domain
$Y_r(s)$	reference signal in s domain
$H(j\Omega)$	frequency function of analog filter
$T_N(x)$	Chebyshev polynomial of order N
Ω_C	cut-off angular frequency
Ω_P	passband edge angular frequency
ε	ripple factor
R_N	n-th order elliptic rational function
ξ	selectivity factor
$Q_{but}(j\omega)$	frequency function for Butterworth filter
K_{but}	gain for Butterworth filter
x_{ref}	reference trajectory
A_{ref}	desired amplitude
f_{ref}	desired frequency
v_{ref}	desired velocity
d_h	periodic disturbance
N_h	order of the highest harmonic component
ω_0	fundamental angular frequency
φ_k	phase corresponding to k-th harmonic component
f_0	fundamental frequency
$R_k(s)$	k-th resonant term in s domain
a_k	gain of k-th resonant term
$Q_B(s)$	transfer function of third order Butterworth Filter
$Q_{BR_k}(s)$	transfer function of third order Butterworth Filter with built-in resonant term
n_0	coefficient for numerator of third order Butterworth Filter
d_0	coefficient for denominator of third order Butterworth Filter
d_1	coefficient for denominator of third order Butterworth Filter
d_2	coefficient for denominator of third order Butterworth Filter
d_3	coefficient for denominator of third order Butterworth Filter
$R_h(s)$	lumped resonant terms in series form
$MR_k(s)$	approximated resonant term used in digital implementation

$MR_h(s)$	approximated lumped resonant terms used in digital implementation
$Q_{IM}(s)$	internal model low-pass filter for disturbance observer
d_{n1}	normalised coefficient for denominator of internal model low-pass filter
d_{n2}	normalised coefficient for denominator of internal model low-pass filter
d_{n3}	normalised coefficient for denominator of internal model low-pass filter

Chapter 1

Introduction

1.1 Background

1.1.1 Tribology and Tribotest

Achieving the relative movement of one solid surface with respect to another is fundamentally important for the functioning of a variety of mechanisms [1]. The arising of friction in such process is unavoidable, which is defined as the tangential reaction force between two surfaces in contact. It has been widely accepted that the interactions between asperities on the two surfaces coming into contact contribute to the generation of friction. The above concept of asperities provides a physical explanation for various friction-related observations. On the one hand, high friction is desirable in some cases such as brakes and clutches, where adequate and controlled friction is necessary to dissipate kinetic energy and transfer torque. On the other hand, low friction is desirable in some cases such as bearings and gears, where work that is done in overcoming friction in machines is dissipated as heat. By reducing the unwanted friction we can achieve an increase in overall efficiency. Furthermore, the unwanted friction can lead to not only the waste of energy but also the damage of contacting surfaces due to the progressive removal of material from a surface in sliding or rolling contact against a counter-surface [2]. In fact, friction and wear in manufacturing and transportation lead to considerable losses. It is estimated that 25% of the energy input in industry is spent on overcoming friction forces. On a

large scale, the losses connected with friction and wear in machines are estimated in 3% to 5% of the gross national product [3]. These costs are not inevitable as they can be addressed and reduced by appropriate engineering actions. Lubrication is regarded as an effective measure to mitigate the impact of friction and wear, which is related to the process or technique of using a lubricant to reduce friction and wear in contact between two surfaces. It reduces friction by introducing between the sliding surfaces a layer of material with a lower shear strength than either of the surfaces. Thus, the industrial significance of the study on phenomena of friction, wear and lubrication has long been recognised by researchers. In order to cover the aforementioned issues that encompass interdisciplinary science and technology, the concept of tribology was proposed in 1966 in a report of the UK Department of Education and Science. The subject tribology is defined as the study of science and engineering of interacting surfaces in relative motion, which includes the study and application of the principles of friction, wear and lubrication [4]. The word tribology comes from the Greek word “tribos” , which means “to rub”.

As a relatively new interdisciplinary subject, the science of tribology is still far from having a complete picture of how friction works in all extent. The theories in tribology are mostly based on empirical experiences, rather than the deep scientific background. The obstacles for the study of tribology include but not limited to the fact that friction and wear are not static numbers one can look up in a reference manual. They are system properties rather than material properties, which means that the interactions between surfaces are influenced by not only the materials couple but also the characteristics of the whole tribosystem, such as contact geometry, loading, temperature, etc. Therefore, tribological properties that follow the system aspects of friction and wear call for tribotest in the process of tribological study [2].

As the nature of tribological tests is complicated, there are numerous ways to perform tribotests and the process of selecting the most appropriate test for a specific purpose is fundamentally important to make meaningful interpretations. Tribotests can be classified according to the degree of realism, trajectory, conformation, and test geometries, etc. According to the degree of realism, the tribotests can be classified into the following types: field test, bench test, sub-system test, component test,

simplified component test and model test. Fig.1.1 shows an example of studying the wear mechanism of the cylinder-piston system in a car engine with different levels of the degree of realism [2]. In a field test, the whole vehicle should be driven under realistic service conditions; in a bench test, the whole vehicle can be 'driven' in a laboratory; in a sub-system test, only the engine will be included in the test; in a component test, only the important machine components of the engine should be evaluated; in a simplified component test, we can further reduce the number of components included; in a model test, there is even no necessity to include any real components. In general, we want a tribotest to imitate the conditions of a real application closely. However, considering the cost, test time and accurate control of test conditions, tribotest with a lower degree of realism can be preferable in some cases.

In addition, the model tests can be further classified according to the contact geometries applied in the tests. The examples on contact geometries are shown in Fig.1.2 [1]. In this thesis, we focus on the application of pin-on-flat tribotest, where a plate is driven to achieve reciprocating motion with respect to a pin or ball component being pushed against it as depicted by Fig.1.2.(c).

1.1.2 Tribotester and Voice Coil Motor (VCM)

A number of friction and wear test apparatuses have been developed for different tribological applications. In this study, we focus on a test apparatus applied in pin-on-flat tribotest called high frequency reciprocating rig (HFRR), which is primarily designed for the assessment of the lubricity of diesel oil [5]. It was proposed by Imperial College London in 1990s as a solution for highly reproducible and accurate measurement of lubricity in diesel fuels. The diesel oil used by combustion engine acts as a lubricant in all diesel fuel injection equipment. In fact, a fuel with poor lubricity will lead to catastrophic wear to critical pump components, which is one of the causes of fuel pump failure [6]. The standard ISO-12156-1:2016 on HFRR gives the guidelines for the conduction of reciprocating tribotests for diesel fuels and presents a suggested appearance of HFRR as shown in Fig.1.3 [7]. On HFRR, a plate component moves relative to a stationary pin or ball component in reciprocating motion or vice versa [4]. Both the frequency of the reciprocating motion and the

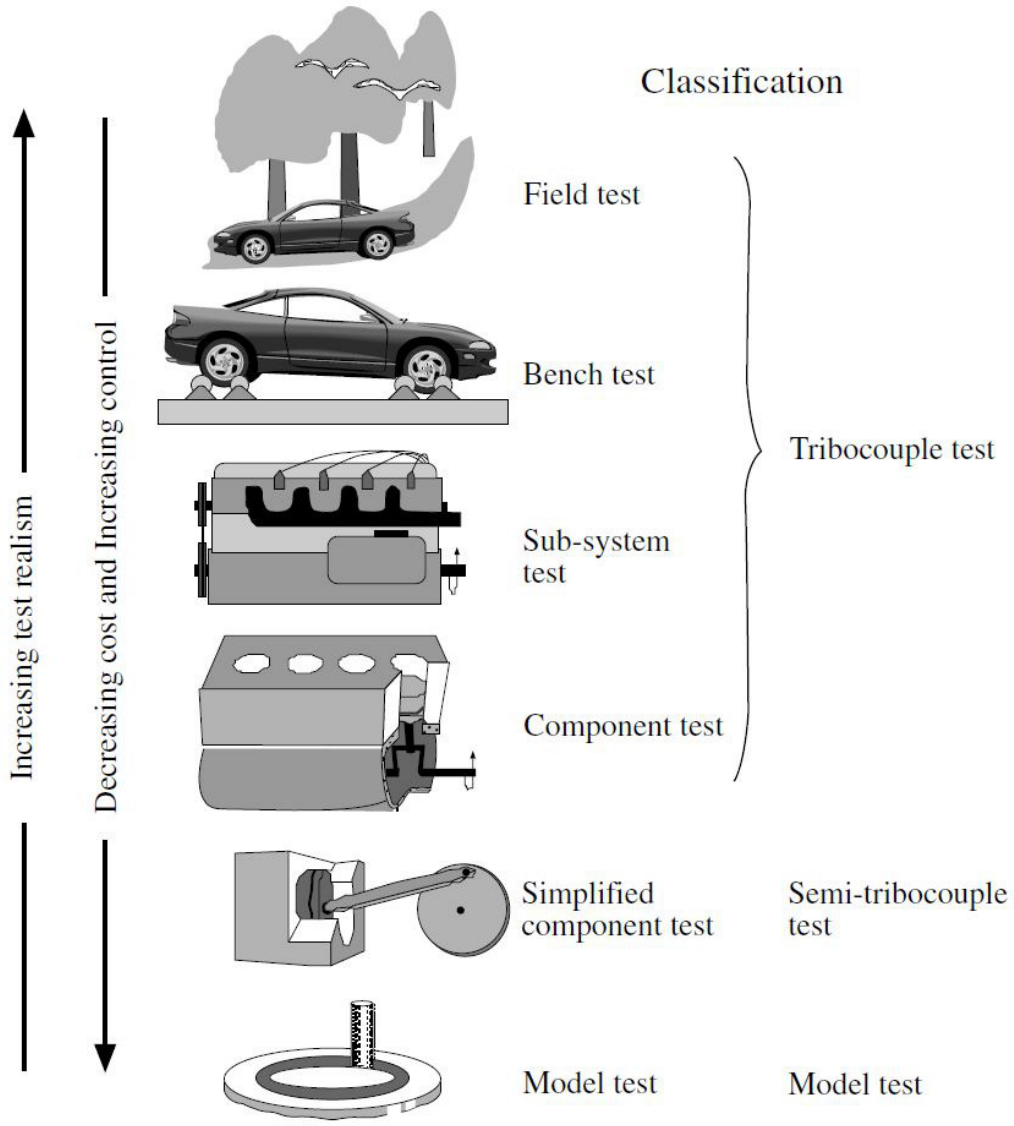

Figure 1.1: Classification of tribotests according to the degree of realism

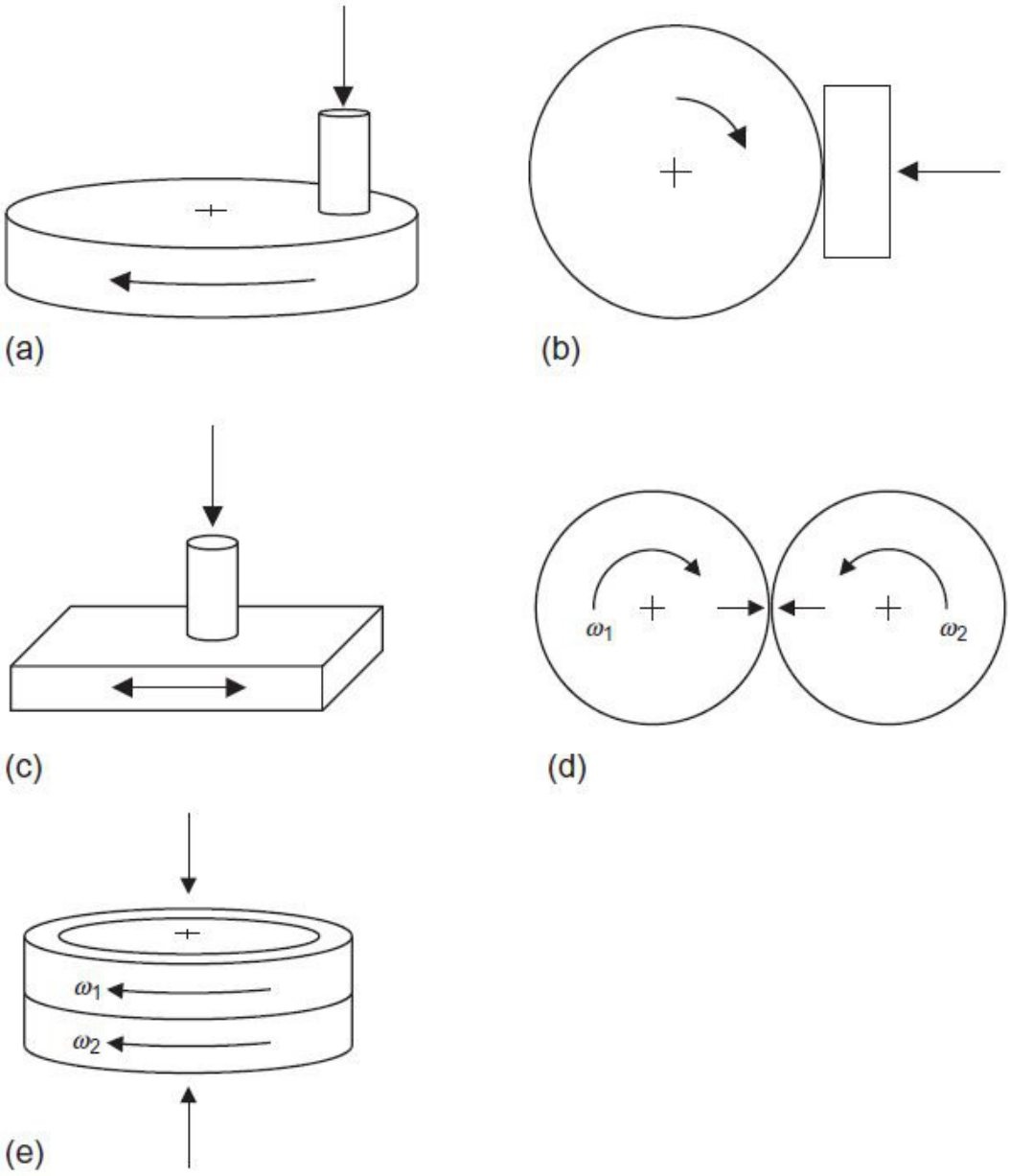

Figure 1.2: Examples on contact geometries employed in tribotest ; (a) pin-on-disc; (b) block-on-ring; (c) pin-on-reciprocating plate (pin-on-flat); (d) twin disc; (e) ring-on-ring

stroke of it should be constant regardless of the varying friction during experiment as a result of wear. Both the plate and ball components are made of steel with surfaces being polished as requested in the standard. The steel ball is pushed against the steel plate with a controlled force during the reciprocating motion. The steel plate fully immerses in the diesel fuel under test that contained by a reservoir. A heating bath outside of the fluid reservoir is used to keep the temperature of the diesel fuel at a predefined value. In summary, metallurgies of the ball and plate, test fluid temperature, load, frequency, stroke length, and the ambient air conditions of temperature and humidity during the test are specified in the standard and controlled during experiment. At the end of the experiment, wear scar generated on the steel ball under specified conditions due to friction can be found, of which the diameter is converted to a value at a standard water vapour pressure and taken as a measure of lubricity. Fig.1.4 gives an example of the wear scar produced on the steel ball [6]. The measured mean wear scar diameter (MWSD) is obtained by averaging the longitudinal and transverse diameters of the ellipse-shaped scar on the steel ball. The microscope camera is used in the measurement of MWSD, which allows the user to capture calibrated images of a wear scar and measure the wear scar on the PC screen. In this way, the lubricity of diesel fuel can be assessed [7]. In addition, commercial available HFRR is capable of measuring and logging the data of friction and thickness of lubricant film when the experiment is being conducted [8]. It has been gradually applied in other fields of tribological research due to its versatility and availability.

HFRR is usually driven by linear voice coil motor (VCM) at high frequency with a small amplitude. VCM is a direct drive DC motor with its structure similar to that of a loudspeaker. There are two types of VCMs classified by the form of motion, namely, linear VCM and rotary VCM. In this thesis, we focus on linear type VCM. Fig.1.5 shows the structure of linear VCM. It mainly consists of voice coil, permanent magnet and magnet housing. It is Lorentz force law that governs the operation of VCM. Lorentz force is generated when a current-carrying conductor is placed in a magnetic field. In the case of VCM, the magnetic field is generated by the permanent magnet in VCM and the conductor is a coil of wire called 'voice

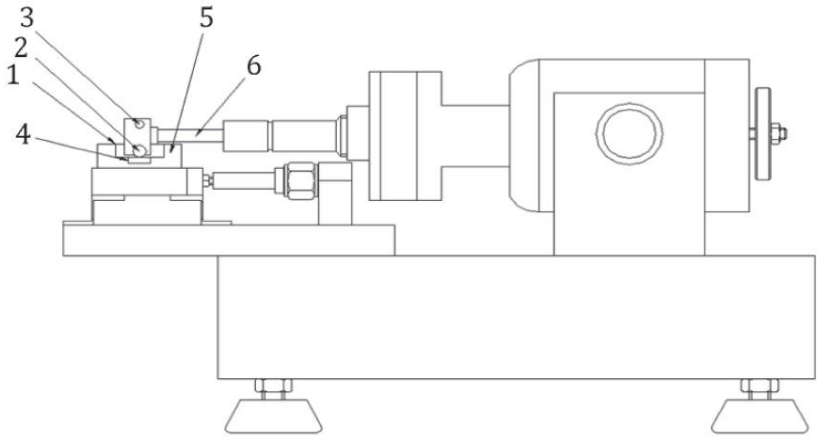

Key

1	fluid reservoir	4	test plate
2	test ball	5	heating bath
3	test mass	6	oscillating motion

Figure 1.3: A suggested schematics of HFRR by ISO 12156-1:2016

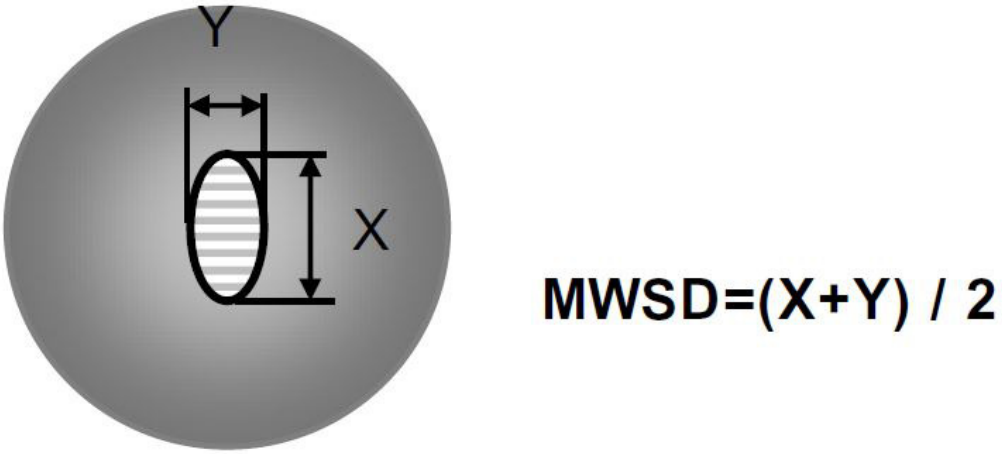

Figure 1.4: Measured mean wear scar diameter (MWSD)

coil'. When current is applied to the coil, the magnitude of the force exerts on the coil is proportional to the current flows into the coil. Given the value of the current, the generated force is relatively constant throughout the stroke of the VCM, with minor decreases at the beginning and end of it. The name 'voice coil' comes from its mechanical structure, in which a coil is deployed in the air gap of a magnetic circuit. The voice coil will vibrate, once alternating voltage applied between its two terminals, which is similar to vibrating the paper cone of a loudspeaker. Linear VCM can offer unlimited high resolution due to the absence of commutation and transmission device, which is attractive to the applications that require accurate positioning and fast response [9]. It has been widely used in precision positioning and vibration isolation applications [10] [11]. Different from other types of motor, a gearbox or corresponding transmission device is usually eliminated from the VCM driven system as it can realise direct drive. There are mainly two packages of linear VCMs available as shown in Fig.1.6 [12]. The VCM on top of Fig.1.6 is the moving coil type VCM, of which the coil assembly is moving with the permanent magnet being stationary. The VCM on the bottom is moving magnet type VCM, of which the coil assembly is fixed with the permanent magnet moving. The VCM applied to HFRR in this thesis is moving coil type linear VCM.

1.1.3 Challenges

According to HFRR standard, the average relative error of the amplitudes of oscillation at $50Hz$ given by commercial HFRR can be more than 30%, where the desired amplitude varies from $200\mu m$ to $700\mu m$ [7]. One of the reasons that account for such large error is that during the time of operation, the coefficient of friction keeps on changing, which contributes to the non-linearity and time-dependent characteristics of the system. In addition, the sinusoidal position trajectory required by standard ISO-12156-1:2016 will lead to periodic zero-crossings of velocity. Therefore, the friction exerts on motor shaft can change abruptly at those points due to the transitions between kinetic friction and static friction (slip-stick effect), which makes the position control problem challenging. As a result, friction as a typical hard nonlinear disturbance to the plant leads to the difficulty in VCM position con-

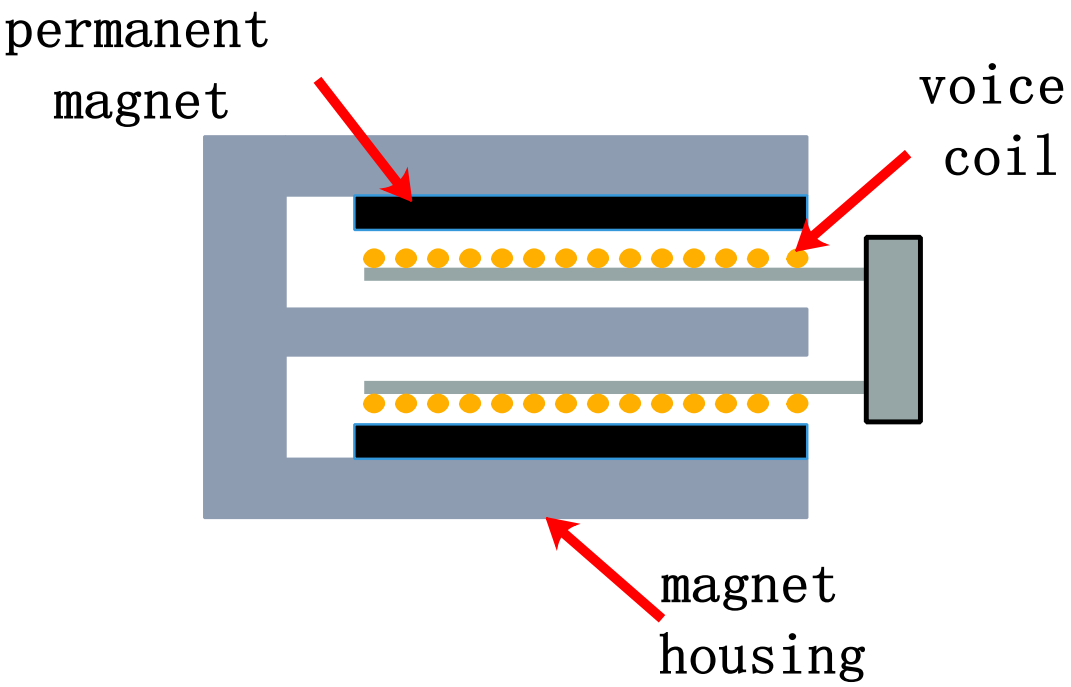

Figure 1.5: Structure of linear VCM

trol [13] [14]. Moreover, fretting wear experiments in the future require even higher accuracy of HFRR, where the relative error of amplitude should be less than 5% at the desired frequency. Consequently, there is a need to improve the performance of HFRR in the application of pin-on-flat reciprocating tribotest. The key should be the design of the controller for the VCM on HFRR.

1.2 Literature Review on VCM Related Control Methods

Fig.1.7 shows the block diagram of a generalised control scheme for VCM in case of reference position tracking task, which has been widely applied in literature. Signal r from the reference generator represents the reference signal that the shaft of the VCM is expected to follow. Signal x is the position of the shaft of VCM; signal i is the current flows into the coil of VCM. Both x and i are usually regarded as the output of VCM in the view of control design. The controller of VCM takes the

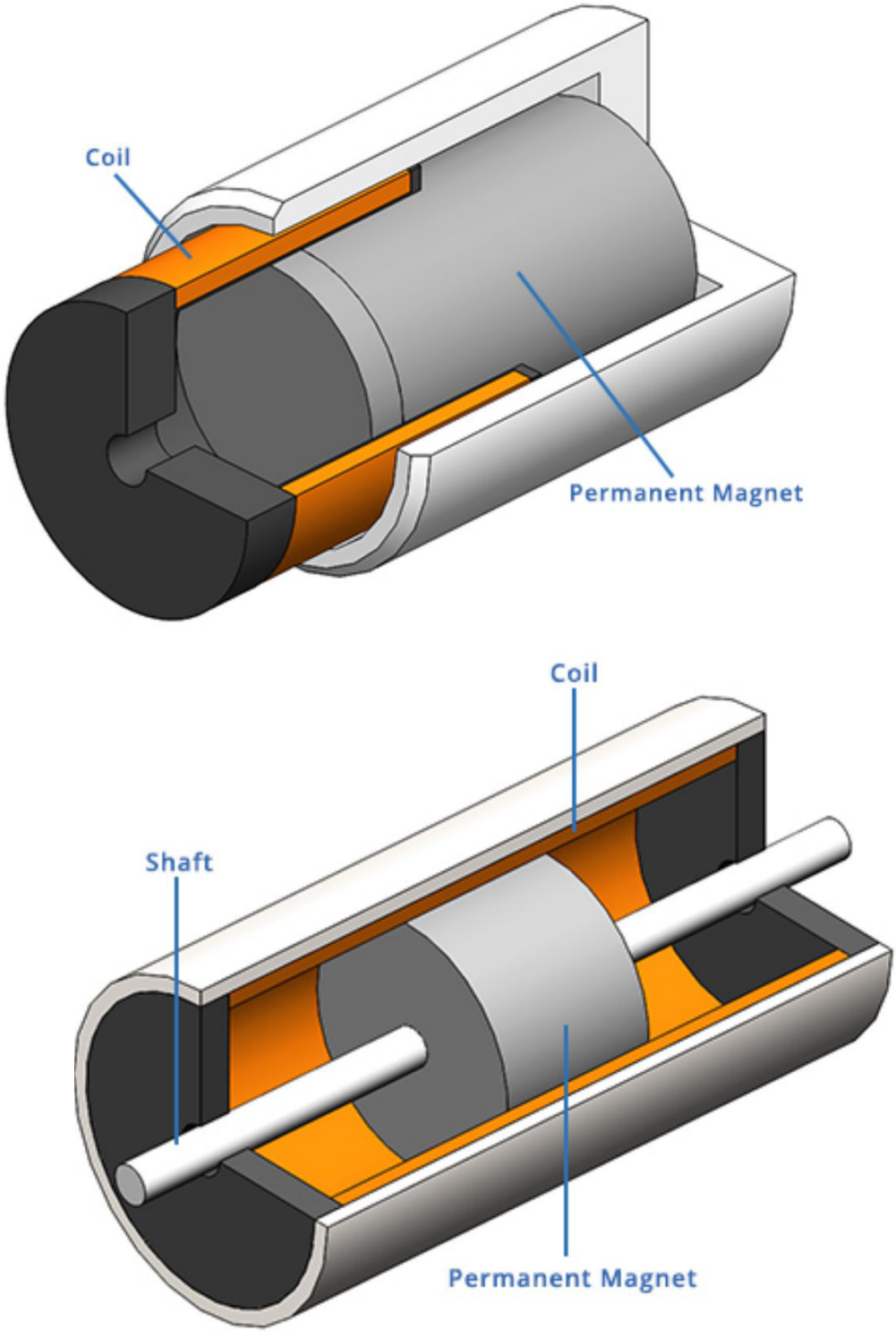

Figure 1.6: Different packages of linear VCMs: moving coil VCM (top) and moving magnet VCM (bottom)

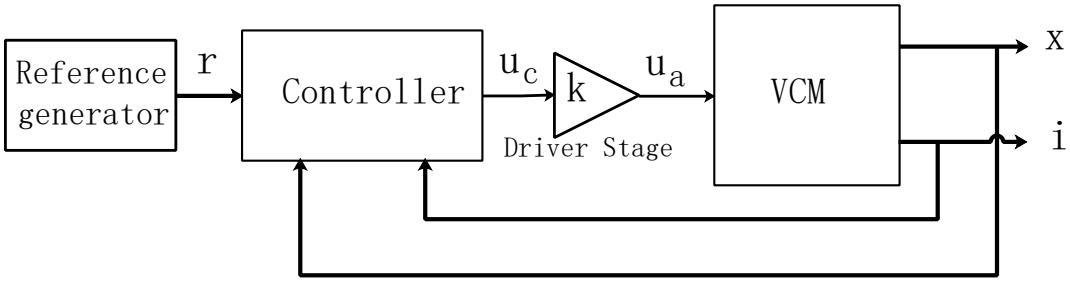

Figure 1.7: Block diagram of a generalised control scheme for VCM in reference position tracking task

reference signal r, feedback position signal x and feedback current signal i as inputs. It outputs the control signal u_c based on the built-in control algorithms, which is then fed to the input of the driver stage. The driver stage can be implemented in either the form of analog amplifier or full bridge driver circuit. The output of the driver stage is the voltage u_a applied to the terminals of VCM to excite the motion of it. Ideally, the voltage u_a should be proportional to the control signal u_c. The controller is usually implemented using embedded processor such as digital signal processor (DSP). The position of the shaft is measured by an encoder; the current is measured by either Hall sensor or shunt resistors.

The following sections present the control methods applied to VCM in literature, which can be classified according to their treatments of disturbances, namely, the control methods without disturbance compensation and the control methods with disturbance compensation. In the section of control methods with disturbance compensation, the disturbance observer based control techniques are shown in detail.

1.2.1 Control Methods Without Disturbance Compensation

PID based control: As a widely used model-free approach, PID control has been adapted to VCM position control. [15] suggests that the gains of PID controller applied to VCM position control can be tuned online by fuzzy logic technique. [16] modifies conventional PID to state feedback style position velocity controller with disturbance compensator. Both [17] and [18] investigate the application of nonlinear PID technique on VCM.

Anti-windup techniques: A common application for VCM is the actuator in a hard disk driver (HDD). To improve the tracking accuracy of the head in an HDD, a high-bandwidth secondary actuator is mounted on the VCM-actuator to construct a dual-statge actuator. Due to the limitation on the displacement of the dual-stage actuator, anti-windup techniques have been introduced. [19] proposes a modified decoupled master-slave dual-stage control scheme for HDD. It considers the enhancement of system stability when the secondary-stage piezoelectric (PZT) actuator is saturated. [20] improves the performance of actuator at the neighbour of saturation region by introducing L_2 approach within the framework of robust control design in combination with linear matrix inequality (LMI) optimisation method.

PQ Method: The VCM in combination with PZT actuator on dual-stage actuator is regarded as a dual-input/single-output (DISO) system. PQ method transforms the problem of designing controllers for DISO systems to two single-input/single-output (SISO) design problems. [21] and [22] apply PQ method together with loop-shaping techniques to the control of dual-stage actuator in HDD.

Optimal Control: Optimal control techniques have been introduced to regulate the positioning of VCM-actuator. [23] improves the disturbance rejection properties in the loop-gain crossover frequency region of some previously designed LQG controllers for HDD by appropriately shaping the sensitivity function. Apart from optimisation concerning positioning accuracy, proximate time-optimal servomechanism (PTOS) has also been introduced to the control of VCM. [24] modifies the original PTOS by introducing a predetermined damping coefficient to improve the transient performance of the VCM-driven stage. [25] improves the performance of PTOS in long-span seeking through compensator-based techniques. [26] sets a small damping ratio when applying PTOS. This is done to achieve a fast rise time. The resultant overshoot that within the PZT stroke limit is then reduced by the PZT actuator. [27] improves the system transient response through reset control. The solution of the controller is obtained by solving Riccati equations as a generalised method in optimal control design.

Robust control: [28] presents an experiment based method to characterise the uncertainty of VCM in HDD and utilise the obtained model of disturbance for H_2

robust controller design. [29] applies robust and perfect tracking control method to VCM, where perfect tracking can be achieved with low order control law. [30] proposes a new mixed H_2/H_∞ control design for VCM through introducing additional slack variable to LMI based approach.

Vibration rejection techniques: The resonance modes of the components on VCM can significantly degrade the performance of positioning accuracy. To tackle the issue, vibration rejection techniques have been introduced to VCM controller design. [31] applies active vibration rejection to VCM using the feedback signal from PZT sensor mounted at the end point. [32] applies LQG to suppress the vibration of optical disk VCM drive. [33] uses H_∞ techniques to design the controller for the purpose of vibration suppression. [34] applies notch filter to suppress the resonant modes obtained from experiment. [35] applies decentralised control scheme for the dual-VCM stage with a phase-lead interaction filter to suppress the vibration.

Additional control methods: There are additional control methods for VCM. [36] designs feedforward loops from the reference signal for both VCM and PZT actuator on a dual-stage servo system. In addition, the decoupling between VCM and PZT actuator is achieved by applying additional feedforward loop from VCM to PZT actuator. [37] proposes the tracking control method for a dual-stage actuator that utilising the model of VCM to predict the error, which improves the transient performance of the system. [38] discusses the method for reference signal generation for VCM in HDD. The idea of structural vibration minimised acceleration trajectory is utilised to adjust the errors at the end of the trajectories. [39] applies Self-tuning control and online identification to the electrostatic micro-actuator for computer disk.

1.2.2 Control Methods With Disturbance Compensation

Model-based friction compensation techniques: Friction acts as a disturbance being injected into the system, which occurs at the pivot of the head in HDD. Researches have been done to compensate for the friction to mitigate its impact on the system. [40] identifies the parameters for the model of friction through experiment results and implements model based friction compensation for the rotary VCM in

HDD. [41] obtains the hysteresis of friction versus head position through experiment. Then an operator-based modelling approach is utilised to construct the model of hysteresis in order to compensate friction exerts on VCM in HDD operation.

Neural Network (NN): As multi-layer perceptron can be used to approximate complex nonlinear systems, NN has been applied to implement nonlinear controllers for VCM. [42] applies an adaptive NN demand tracking controller to the VCM-actuator with high-frequency resonance cancellation capability, which is achieved by extending the linear control term of the NN-controller by notch-filters. [43] applies adaptive NN to approximate the unknown bounding function of hysteresis friction on VCM for the purpose of compensation. [44] applies two NNs to the control of VCM, with one detecting external vibrations and compensates for its effect through feedforward action, another compensating for friction. [45] utilises wavelet fuzzy cerebellar model articulation controller (WFCMAC) with fuzzy compensator in the application of VCM-driven stage positioning. [46] applies an adaptive dynamic sliding-mode fuzzy CMAC (ADSFC) in combination with a fuzzy compensator to the control of VCM-driven stage positioning. [47] uses a B-spline neural network to online approximate an unknown nonlinear term in the system dynamics of a VCM. Based on that, a B-spline neural position control (BNPC) system in combination with a fuzzy compensator is proposed. [48] applies a compensatory fuzzy NN observer in combination with a switching compensator. The controller, in this case, is selected as fractional order sliding mode controller (FOSMC).

Table.1.1 and 1.2 are given to summarise the advantages and limitations of the existing control methods applied to VCM in the literature mentioned above. The corresponding quantitative indicators are given to reflect the performances of control systems. For those references without explicit quantitative indicators, the abbreviation N/A that represents not applicable is used.

Disturbance observer based control techniques: The frictional load as an external disturbance leads to the difficulty in achieving high accuracy position control of VCM on HFRR using traditional control methods. In fact, the uncertainties of plants and external disturbances widely exist in industrial systems, which lead to degradation in performance and even instability of the systems under control. On

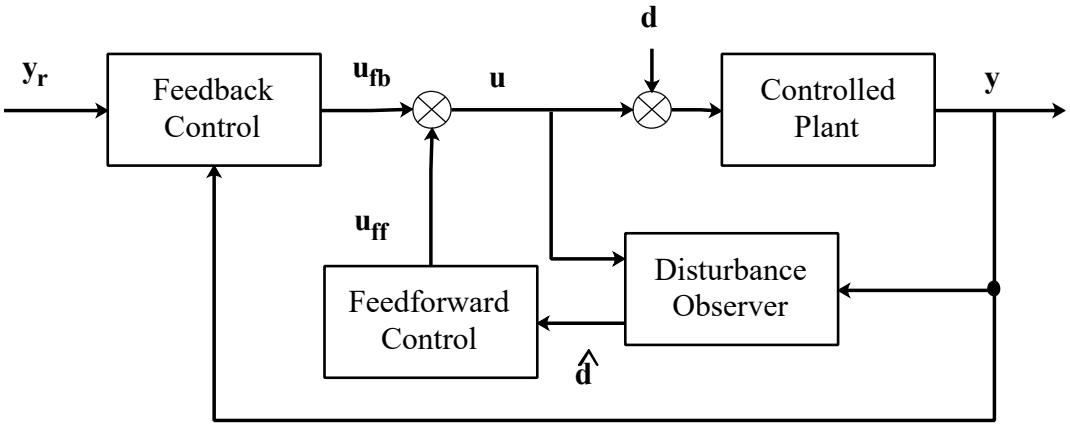

Figure 1.8: A generalised framework of disturbance observer based control for SISO system

the one hand, feedback as a basic concept in automatic control aims to attenuate uncertainties and disturbances [49] [50]. However, classical feedback control methods such as Bode and root-locus, synthesise controller with limited disturbances attenuation capability [51]. Therefore, when severe uncertainties and disturbances present, classical feedback control methods will lead to unsatisfactory performance. On the other hand, different from feedback control methods, feedforward control schemes are regarded as effective disturbance compensation methods that can attenuate uncertainties and disturbances explicitly. To implement feedforward control, not only the uncertainties and disturbances but also the models of process and disturbance channels should be known [52]. As uncertainties and disturbances cannot be directly measured by sensors in most cases, the estimation of them based on measured variables becomes necessary in the employment of feedforward control schemes. It should be noted that the influence of uncertainties of plants can be considered as being equal to the influence of a component of external disturbances from the view of measured variables [53]. Therefore, it is natural to take uncertainties and disturbances as a lumped disturbance term. Based on that, disturbance observer techniques have been introduced to deal with the estimation of the lumped disturbance. In the following discussion in this thesis, the term 'disturbance' refers to the lumped disturbance that takes both uncertainties and external disturbances into account.

The generalised framework of disturbance observer based control for single-input/single-output (SISO) system is shown in Fig.1.8 [52]. The composite controller in Fig.1.8 consists of a feedback controller and a disturbance observer based feedforward controller. The signal d added to the control input u represents the lumped input disturbance that takes the influence of both uncertainties and disturbances into account, which can be obtained by applying coordinate transforms to uncertainties and disturbances that injecting the plant at different channels. The uncertainties and disturbances, in this case, is said to fulfil the matching condition, where the disturbances should act on the system via the same channels as the control inputs or can be transferred to the same channels as the control inputs [52] [54]. The disturbance observer estimates the lumped input disturbance by taking the measurement of the plant and the control input. The estimated lumped input disturbance $\hat{d}$ as the output of the disturbance observer is then used by the feedforward controller to achieve disturbance compensation. It should be noted that the basic idea presented in Fig.1.8 for a SISO system can be applied to MIMO systems as well. As the feedforward compensation term is applied to disturbance observer based control, a faster response in counteracting the disturbance is realised compared with that of the classical feedback control schemes. In addition, the conservativeness of disturbance observer based control is less than most robust control methods based on worst-case design [52].

There are various disturbance estimation approaches developed, which can be divided into linear disturbance estimation techniques and nonlinear disturbance estimation techniques [53]. The linear disturbance estimation techniques can be further classified according to the domain of problem formulation, namely, frequency domain linear disturbance observer that based on classical control theories and time domain linear disturbance observer that based on modern control theories. [55] and [56] propose the primary block diagram of frequency domain disturbance observer, where the design of the low-pass filter in disturbance observer is the key that determines the performance of the disturbance observer in terms of bandwidth. On the other hand, most of the linear disturbance estimation techniques formulate the estimation problem in time domain. [57] applies coordinate transform to the plant

under control and adds a new state to represent the lumped disturbance. Then a state observer can be used to estimate both the states of the system and the lumped disturbance simultaneously. [58] constructs the augmented state space representation of the system, which takes the disturbance as the output of an exogenous system. The disturbance can then be estimated within the framework of modern control theories. [59] and [60] apply low-pass filters to the implementations of disturbance observers in time domain, which are closely related to the design guideline proposed in [61]. The application of linear disturbance estimation techniques can be extended to nonlinear systems as the dynamics of the nonlinear part can be regarded as disturbance and the whole systems can then be treated as linear systems with appropriate compensation based on estimated disturbance [53]. However, it is desirable to consider the known nonlinear dynamics of the system in the design of disturbance observers in order to further improve the performance in terms of estimation accuracy. [62] estimates the disturbance torques on a nonlinear robotic manipulator with the known nonlinear dynamics of the system embedded into the disturbance observer. [63] and [64] apply extended high gain observer to estimate the lumped disturbance term of a partially feedback-linearizable nonlinear system with stable zero dynamics. The method can be applied to MIMO system by decomposing the system into multiple SISO subsystems.

Comment: Aforementioned control methods deal with the position control of the VCM-driven system from different perspectives. However, as far as the author knows, the control of VCM on HFRR has not been addressed in the open literature, where the frictional load is the dominant disturbance that leads to unsatisfactory performance.

1.3 Motivation and Objectives

Tribotest is essential to the study of tribology as tribological properties of materials highly rely on a number of factors, such as temperature, humidity, contact geometry, etc. A meaningful interpretation can only be obtained after specifying and controlling these factors in a tribotest. There are various types of tribotester

Control Method	Advantages	Limitations	Quantitative Indicator
PID based control	model-free and simple structure	contradiction between stability and rapidity	[15]:steady state error 0.67%; [16]:N/A; [17]:N/A [18]:N/A
Anti-windup techniques	improved performance in the case of second stage saturation	complex design procedure	[19]:N/A; [20]:N/A
PQ method	decomposes a DISO system into two SISO systems to address the interaction	requires frequency response model of PZT	[21]: 45 degree of phase margin and 6dB of gain margin at 2470Hz; [22]: 48 degree of phase margin and 6.8dB of gain margin at 1kHz
Optimal control	fast seek time in point-to-point motion with reduced chattering problem	time consuming tuning process	[23]: N/A; [24]: settling time 5.94ms for 5000 track seek; [25]: N/A; [26]: position tracking error: 143.4nm; [27]: settling time 0.32ms for $2\mu m$ seeking target

Table 1.1: Existing control methods applied to VCM: Part I/II (N/A:not applicable)

Control Method	Advantages	Limitations	Quantitative Indicator
Robust control	ensure robust stability and perfect tracking under unmodeled dynamics	experiments are needed to characterize uncertainties; trade-offs are needed to make the controllers implementable	[28]: N/A; [29]: standard deviation of position error 0.095μm; [30]: H_2 norm of position error standard deviation 7.48nm
Vibration rejection	actively reject actuator arm resonance modes at high frequency band	requires experiments to get frequency response of actuator	[31]: N/A; [32]: N/A; [33]: N/A; [34]: N/A; [35]: standard deviation of position error 7.3nm
Model-based friction compensation	compensate the friction at pivot to improve positioning accuracy	requires experiments to get static friction model parameters	[40]: N/A; [41]: N/A
Neural network (NN)	compensate nonlinearities of systems or approximate complex nonlinear systems using neural network to achieve accurate positioning	complex training and tuning processes	[42]: standard deviation of position error 0.0114μm; [43]: N/A; [44]: N/A; [45]: maximum sinusoidal tracking error 0.0781μm; [46]: N/A; [47]: N/A; [48]: N/A

Table 1.2: Existing control methods applied to VCM: Part II/II (N/A:not applicable)

developed based on different specifications on degree of realism, contact geometry, etc. VCM based HFRR is a widely used tribotester in the application of lubricity assessment of oil and other lubricants, where reciprocating motions of the components under test are achieved by the direct drive VCM on it. VCM is applied in reciprocating tribotest for its theoretically unlimited high resolution due to the absence of commutation and transmission device. However, the tracking accuracy of commercial VCM based HFRR adapting conventional control methods is not satisfactory due to the impact of frictional force that shows hard nonlinearity and time-varying attributes. On the other hand, VCM based HFRR is gradually applied in other fields of tribological research due to its versatility and availability. For example, fretting wear experiments in the future require even higher accuracy of VCM based HFRR. Therefore, there is a need to improve the tracking accuracy of HFRR and the focus should be the control of VCM on HFRR.

The objectives of the study presented in this thesis include:

- Develop the model of VCM based HFRR considering the impact of the frictional load. The model should take both the dynamics of VCM and that of the frictional load into account.

- Investigate and propose candidate control methods for VCM based HFRR. It is desirable to explicitly consider the characteristics of frictional load in the design of controller in order to mitigate its impact on the accuracy of the output of the system.

- Investigate hardware implementation scheme for the candidate control methods. Build up a prototype of VCM based HFRR for verification of the candidate control methods.

- Assess the performances of the candidate controllers through experiments using the prototype of VCM based HFRR. Comparisons among the proposed control methods and conventional control methods should be done.

1.4 Contributions and Thesis Outline

1.4.1 Main Contributions

Main contributions of this thesis are summarised as follows:

- The model of HFRR considering the dynamics of the frictional load is developed by combining the model of VCM and LuGre dynamic friction model. The result shows a fourth order nonlinear system with indifferentiable points in system trajectory. It is the dynamic equations of friction that contributes to the complexity of the system.

- Direct amplitude control is proposed to deal with the amplitude keeping problem of HFRR subjects to frictional load, which takes the error of the amplitude of the position signal as the performance index rather than tracking error. To be specific, only the amplitude and frequency of the reciprocating motion are required to be regulated according to the standard on HFRR. The phase of the position signal is of no concern in the application. Therefore, the proposed control based on short time Fourier transform (STFT) is designed to decrease the error of amplitude rather than the error of position signal that implicitly takes the phase information into account. Both simulation and experiment results show that the proposed control method outperforms PI control in terms of amplitude keeping and harmonics suppression. The control method has been published as a regular paper 'Direct Amplitude Control for Voice Coil Motor on High Frequency Reciprocating Rig' in IEEE/ASME Transactions on Mechatronics (No.1 in the publication list below).

- Acceleration based control with time domain disturbance observer to actively suppress the undesirable effect of frictional load is applied to HFRR. The nominal controller applies finite-time convergence law in order to track sinusoidal reference with a minimised phase delay. There are two phases in the implementation of the control algorithm, namely, the design of a task controller that synthesise the desired system acceleration and the construction of a disturbance compensation module. The frictional force that distorts the output

signal is compensated through the reduced order disturbance observer at the input of the plant. The controller outperforms conventional control in terms of reference position tracking, which is verified through both simulations and experiments.

- Internal model disturbance observer based control is applied to HFRR, of which a modified frequency domain disturbance observer is implemented by embedding the generating model of the frictional load. As the frictional load that dominates the external disturbances to the VCM on HFRR are periodic in reciprocating motions, by exploiting such periodicity attribute, better performance of the system in terms of tracking accuracy can be achieved compared with either conventional feedback control or classical frequency domain disturbance observer based control. It is noted that the internal model disturbance observer based control method can better suppress the harmonics in the error signal compared with the classical frequency domain disturbance observer based control method. The controller is verified through both simulations and experiments.

1.4.2 Publication List

1. **R. Wang**, X. Yin, Q. Wang, and L. Jiang, Direct Amplitude Control for Voice Coil Motor on High Frequency Reciprocating Rig, *IEEE/ASME Transactions on Mechatronics*, vol. 25, no. 3, pp. 1299-1309, June 2020.

2. **R. Wang**, X. Yin, Q. Wang, and L. Jiang, Accleration based Robust Control for Voice Coil Motor on High Frequency Reciprocating Rig, *IEEE/ASME Transactions on Mechatronics*, [due to submit].

3. **R. Wang**, X. Yin, Q. Wang, and L. Jiang, Internal Model Disturbance Observer based Control for Voice Coil Motor to Reject Periodic Disturbances, *IEEE Transactions on Industrial Electronics*, [due to submit].

1.4.3 Thesis Outline

The thesis is organised as follows:

Chapter 2 Modelling and Prototype of High Frequency Reciprocating Rig: This chapter develops the model of HFRR that takes dynamics of both VCM and frictional load into account. To achieve this, the operation principle of HFRR will be discussed first. Then the model of HFRR will be developed by combining VCM model and frictional load model. In addition, The configuration of a DSP based hardware prototype of HFRR, which is used to verify the proposed control methods in the following chapters of this thesis is shown.

Chapter 3 Direct Amplitude Control with Amplitude as Performance Index: This chapter proposes direct amplitude control of the position of VCM based HFRR. It takes the amplitude rather than the position as the performance index to achieve amplitude regulation of VCM. The controller based on STFT realises spectra analysis of the output signal in consecutive time step with the length determined by the windowing function. In addition, the comparisons among the proposed control method, PR control and conventional PI control are presented in both simulation and experiment results sections.

Chapter 4 Acceleration Based Control with Time Domain Disturbance Observer: In this chapter, we apply acceleration based control method to VCM based HFRR. By assuming the relatively slow variation of frictional force and matching condition, the frictional force that distorts the output signal of VCM can be compensated through a reduced order disturbance observer at the input of the plant. The chapter starts by formulating the tracking problem of VCM within the framework of motion control for a single degree of freedom system. Both the design of convergence law for the nominal feedback controller and the coordinate transform for the reduced order time domain disturbance observer are shown. In addition, simulations and experiments to verify the control method are presented.

Chapter 5 Internal Model Disturbance Observer Based Control: This chapter applies internal model principle to modify the classical frequency domain disturbance observer based control method. The frictional load that dominates the external disturbances to the VCM on HFRR are periodic in reciprocating motions.

By exploiting such periodicity attribute, internal model disturbance observer can be constructed by embedding the generating model of disturbance in the frequency domain. The discussion on the selection of low-pass filter for classical disturbance observer and the construction of generating model for disturbance are shown. Both simulations and experiments are presented to compare the internal model disturbance observer based control with classical frequency domain disturbance observer based control for HFRR.

Chapter 6 Conclusions and Future Work: This chapter concludes the findings of this thesis and suggests future research work that can be extended based on results.

Chapter 2

Modelling and Prototype of High Frequency Reciprocating Rig

2.1 Introduction

HFRR has been widely applied to conduct pin-on-flat reciprocating tribotest, where a flat component is driven by the testing rig to achieve high frequency reciprocating motion with respect to a pin or ball component. The motion is driven by VCM on HFRR, of which the working principle is similar to that of a loudspeaker. This chapter will develop the model of HFRR that takes dynamics of both VCM and frictional load into account. To achieve this, the operation principle of HFRR will be discussed first. Then the model of HFRR will be developed by combining VCM model and frictional load model, as the friction exerts on the coil of VCM through motor shaft. In addition, we will show the detailed configuration of a DSP based hardware prototype of HFRR, which is used to verify the proposed control methods in the following chapters of this thesis. As the controllers in this thesis are developed in the form of continuous time controllers and implemented using DSP in the form of discrete time controllers, the difference between them is discussed at the end of this chapter.

2.2 Operation of HFRR

Fig. 2.1 shows the schematic and operation principle of HFRR. When conducting the experiment, the test plate oscillates at a fixed frequency with a fixed stroke. In the meantime, the normal force is exerted to push the test ball against the test plate. Usually, the test ball is loaded against the test plate with a fixed force during the experiment. The contact interface is immersed in a fluid. The friction between the test ball and test plate directly exerts on the coil of VCM through motor shaft. After the operation of the test, the test ball together with the ball holder should be removed from the rig. The diameter of the wear scar on the contacting surface of the test ball can be measured through microscope.

A typical application is the assessment of the lubricity of diesel fuel. Diesel fuel acts as a lubricant in all diesel fuel injection equipment. [7] presents a standard method to assess the lubricity of diesel fuel. The idea is to realise the relative motion between a steel ball and a steel plate that contact with each other. The steel plate immerses in the diesel fuel. By examining the diameter of wear scar on the steel ball after the experiment, the lubricities of different diesel fuels can be assessed.

Fig. 2.2 shows the structure of the voice coil motor on HFRR, which mainly consists of permanent magnet and voice coil. The load is connected to the voice coil through motor shaft. As the friction exerts on the coil of VCM through motor shaft, the model of HFRR is obtained by combining VCM model and frictional load model.

2.3 Model of HFRR

2.3.1 Model of VCM

As VCM is a DC motor, the attributes of a VCM are similar to that of a generalised DC motor with permanent magnet. Fig. 2.3 depicts the equivalent circuit for VCM. The impedance of voice coil is represented in the form of a resistor and inductor in series. In addition, the back electromotive force due to electromagnetic induction on moving coil is demonstrated as a voltage source. According to the

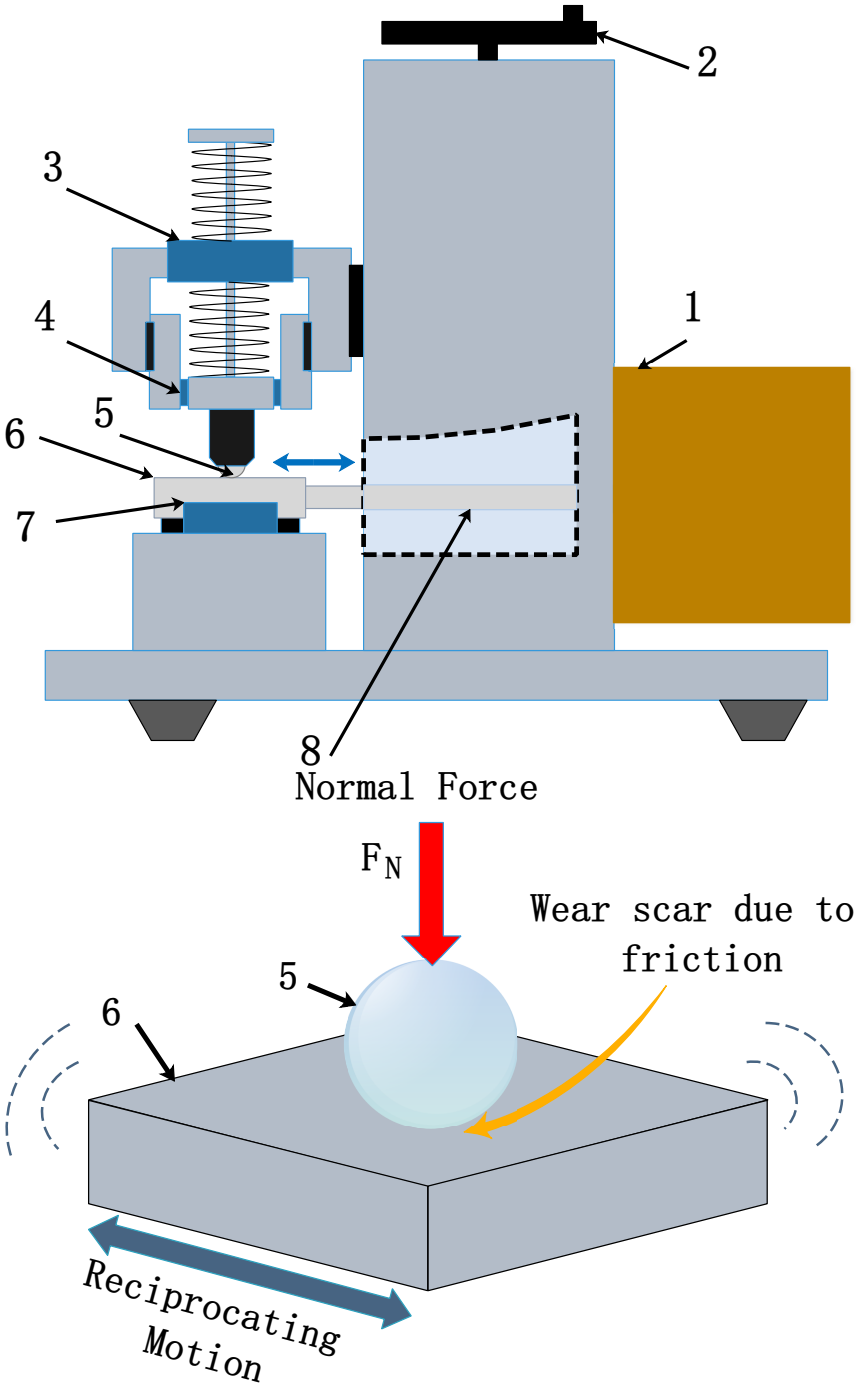

Figure 2.1: Schematic and operation principle of HFRR: 1) VCM, 2) Normal Force Adjustment, 3) Normal Force Sensor, 4) Friction Sensor, 5) Test Ball, 6) Test Plate, 7) Incremental Encoder, 8) Motor Shaft

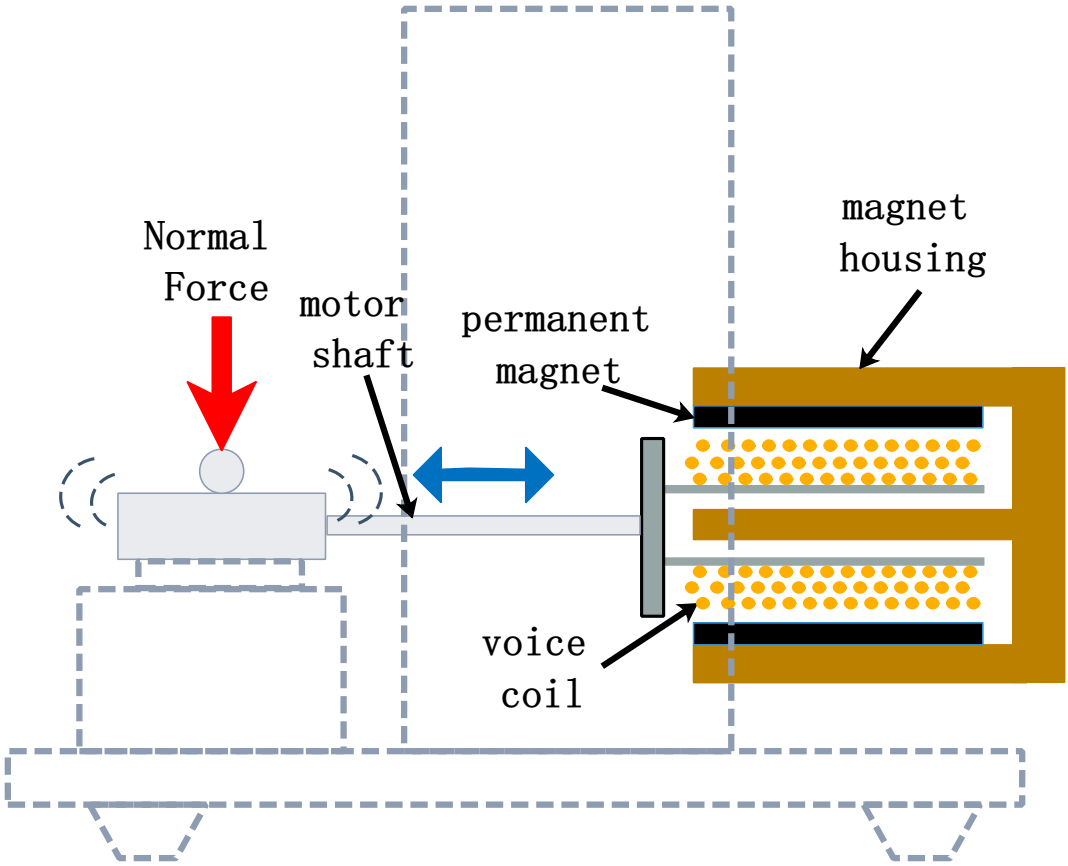

Figure 2.2: Schematic of VCM on HFRR: the test plate is directly connected to the voice coil of VCM through shaft.

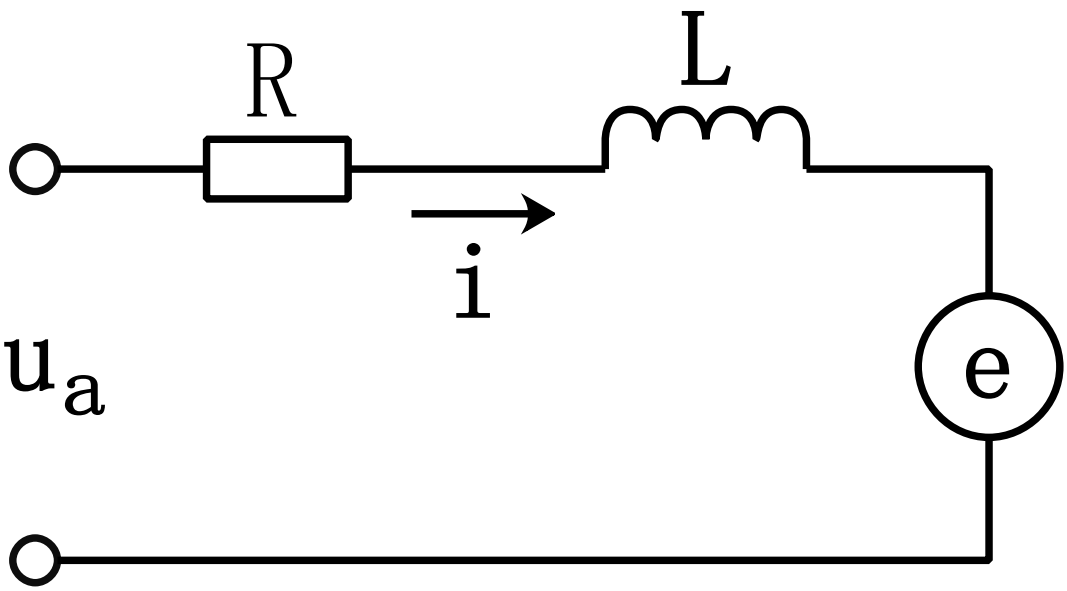

Figure 2.3: Electric circuit model of VCM

Kirchhoff's Circuit Law, (2.3.1) holds. u_a is the voltage between the terminals of VCM. i is the current flows into the coil. R and L are resistance and inductance of the equivalent circuit. e is counter-Electro-Motive Force (counter EMF).

$$u_a = e + iR + L\dot{i} \tag{2.3.1}$$

When operating VCM, the desired amplitude of oscillation of the voice coil is usually less than $1mm$, which is small compared with the length of the air gap. The length of that applied in our research is $110mm$. Therefore, the magnetic field flux density is treated as a constant lumped parameter, as the distributed attribute of it can be ignored in the case of such small amplitude of oscillation. In addition, the effective length of the coil that generating Lorentz force is the same as the total length of the voice coil, since the full length of voice coil subjects to the magnetic field in air gap during its oscillation. The counter EMF can be derived as:

$$e = Blv \tag{2.3.2}$$

B is the magnetic field flux density in the air gap. l is the total length of the coil. v is the velocity of the moving coil. It can be found that considering all the variables in the equation of counter EMF, only the velocity of the coil can be changed in

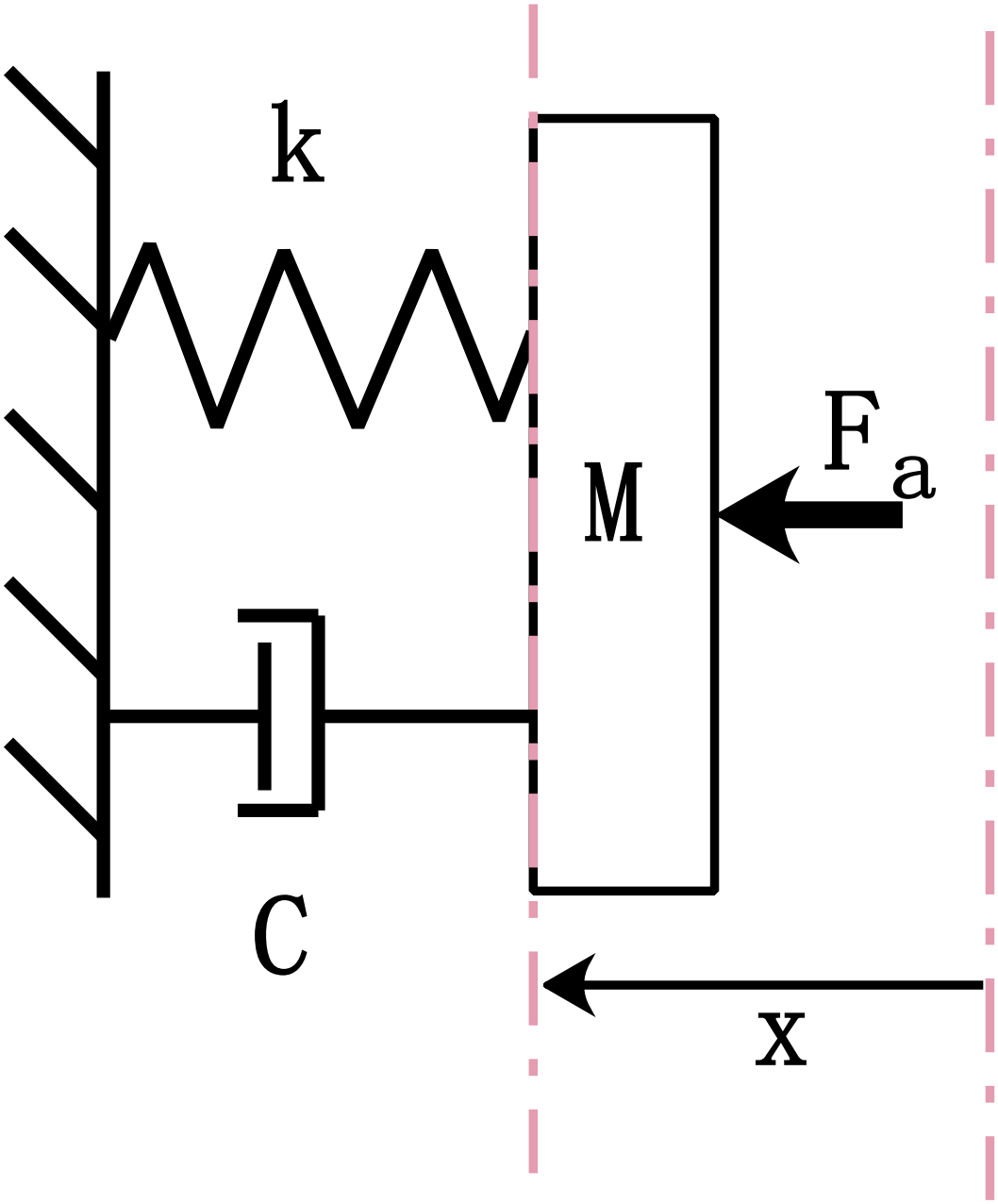

Figure 2.4: Analytic mechanical model of VCM

the operation of the motor. Therefore, we define the product of B and l as motor constant.

$$K_s = Bl \tag{2.3.3}$$

Fig. 2.4 presents the mechanical characteristics of VCM [65]. Previous study [66] indicates that there are two types of VCM, namely MFK type and MF type. MFK type VCM deploys a spring to support the moving coil. In this thesis, we only consider MFK type linear VCM. In Fig. 2.4, k represents spring factor. C is damping factor. M is the total mass of the moving part of VCM. In addition, x is the displacement of VCM shaft. According to Newtons Laws of Motion, we can obtain the following equation:

$$M\ddot{x} + C\dot{x} + kx = F_a \tag{2.3.4}$$

where F_a is the Ampere's force given by:

$$F_a = K_s i \tag{2.3.5}$$

Rearrange (2.3.1) to (2.3.5) above, we can derive the mathematical model of VCM:

$$\begin{cases} \dot{x} = v \\ \dot{v} = -\frac{k}{M} \cdot x - \frac{C}{M} \cdot v + \frac{K_s}{M} \cdot i \\ \dot{i} = -\frac{K_s}{L} \cdot v - \frac{R}{L} \cdot i + \frac{1}{L} \cdot u_a \end{cases} \tag{2.3.6}$$

2.3.2 Model of Frictional Load

Friction is a common phenomenon which can be defined as the resistance to motion when two surfaces slide against each other [67]. Fig. 2.5 shows the lumped forces that exist in a tribological system [68]. v is the velocity of relative motion of the upper body with respect to the lower body. F_f is the friction force in the reverse direction of motion. The enlarged contacting surfaces in Fig. 2.5 show their geometries at the microscopic level. There is a large number of asperity junctions that exist on two contacting surfaces, which contribute to the origin of friction [68].

Previous research reveals that two friction regimes can be defined in the sliding process of a tribological system, namely, the pre-sliding regime and the gross sliding regime [69] [70]. By taking both pre-sliding regime and gross sliding regime into

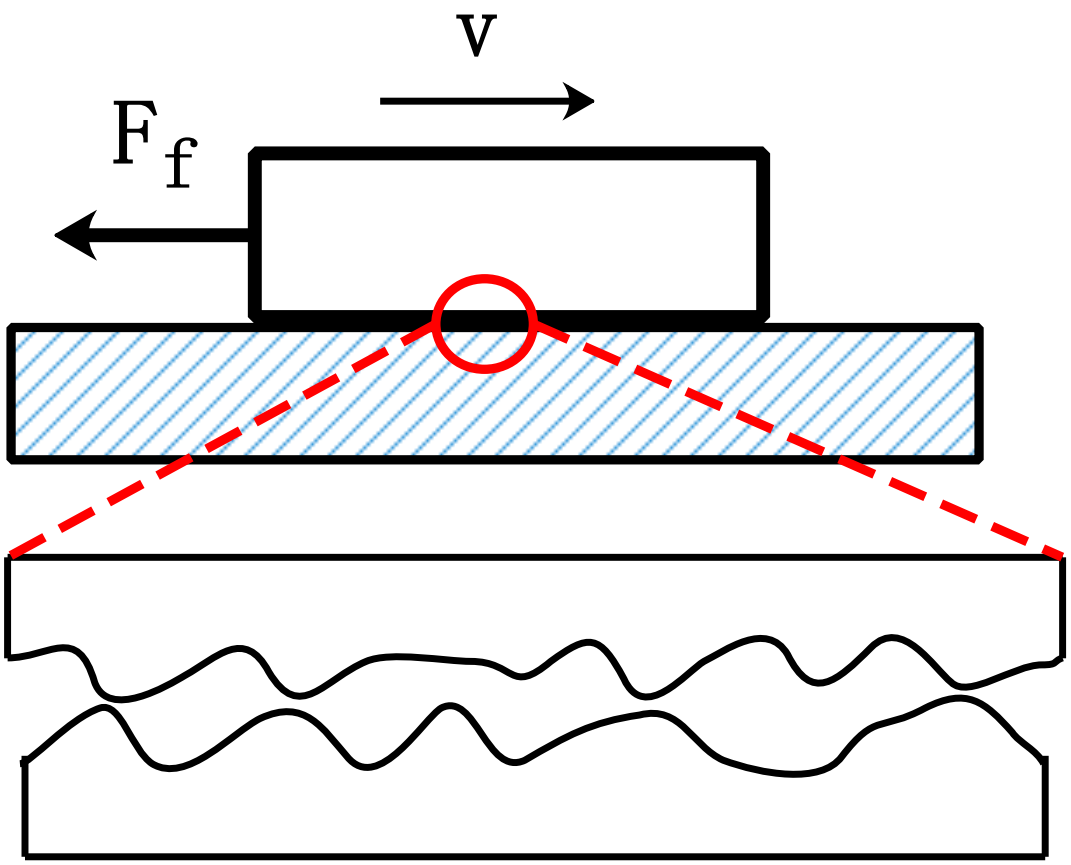

Figure 2.5: Basic friction configuration with enlarged contacting surfaces

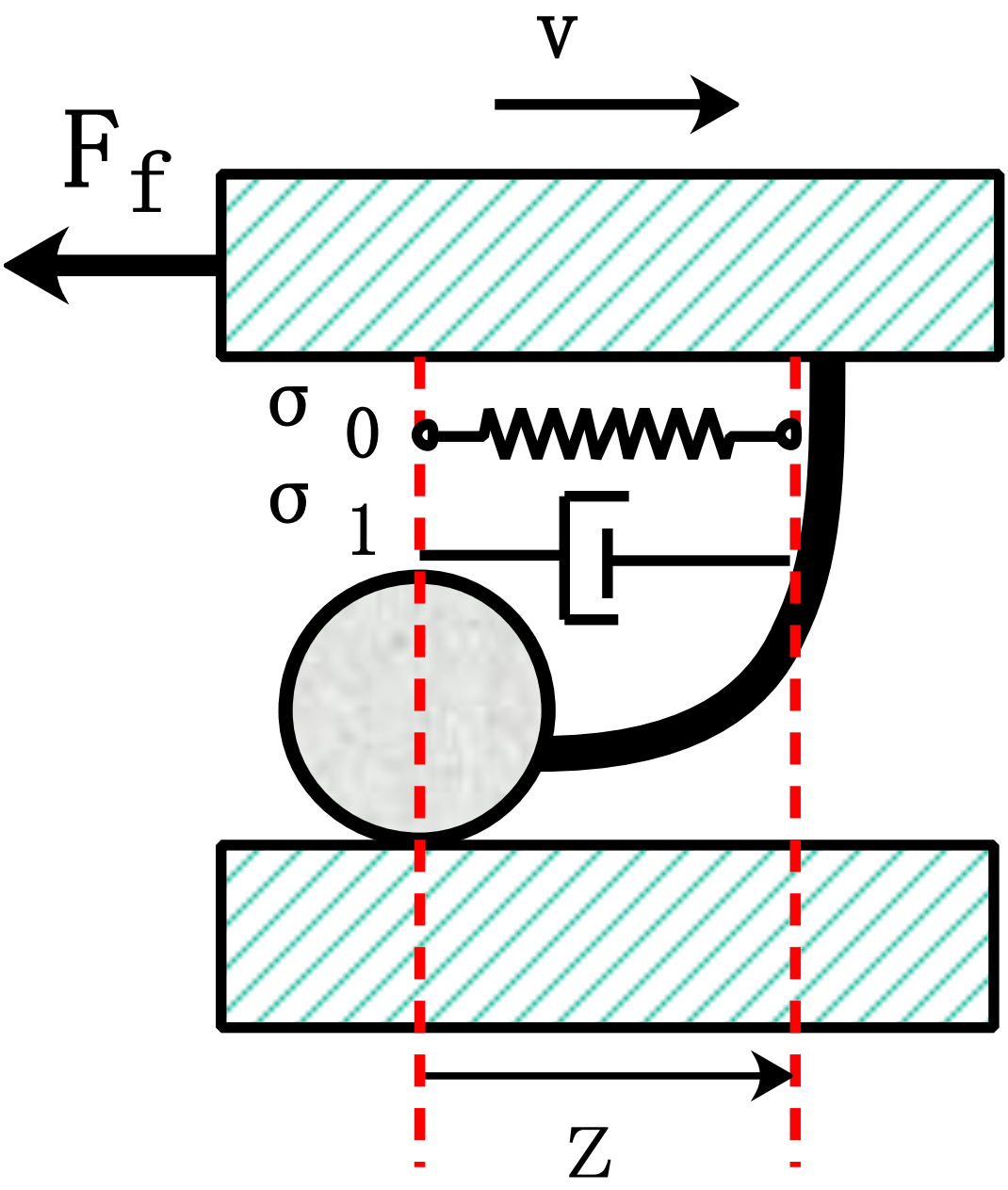

Figure 2.6: LuGre model

account, LuGre model is raised, which is depicted in Fig. 2.6 [67]. LuGre model takes the average behaviour of the bristles that represent the deformations of asperity junctions as a state variable [71]. It is capable of capturing several effects such as stick-slip oscillations and zero-slip displacement [72]. In Fig. 2.6, z denotes the average deflection of bristles, which is modelled as:

$$\dot{z} = v - \sigma_0 \frac{|v|}{S\left(v\right)} z \tag{2.3.7}$$

where v is velocity, σ_0 is asperity stiffness, $S(v)$ is a function of sliding velocity that accounts for the Stribeck effect [73]:

$$S\left(v\right) = F_c + (F_s - F_c) e^{-(|\frac{v}{v_s}|)^{\sigma_{vs}}} \tag{2.3.8}$$

where F_c and F_s stand for the Coulomb friction force and Static friction force respectively, v_s is Stribeck velocity, and σ_{vs} is the shape factor that determines the shape of Stribeck curve. According to the configuration of LuGre Model, the component of friction force due to bristle effect is given by:

$$F_{bristle} = \sigma_0 z + \sigma_1 \dot{z} \tag{2.3.9}$$

where σ_0 and σ_1 represent the asperity stiffness and damping coefficient of frictional interface respectively. To consider the effect of viscous friction, a term proportional to the sliding velocity is added [74] and the lumped friction force is obtained as:

$$F_f = F_{bristle} + \sigma_2 v \tag{2.3.10}$$

Finally, the detailed LuGre model is summarised as:

$$\begin{cases} F_f = \sigma_0 z + \sigma_1 \dot{z} + \sigma_2 v \\ \dot{z} = v - \sigma_0 \frac{|v|}{S(v)} z \\ S\left(v\right) = F_c + (F_s - F_c) e^{-(|\frac{v}{v_s}|)^{\sigma_{vs}}} \end{cases} \tag{2.3.11}$$

The friction acts as a typical external disturbance to the HFRR system from the point of view of control systems, which is a nonlinear function of velocity according to the expression given above. To illustrate the nonlinear characteristics of the friction

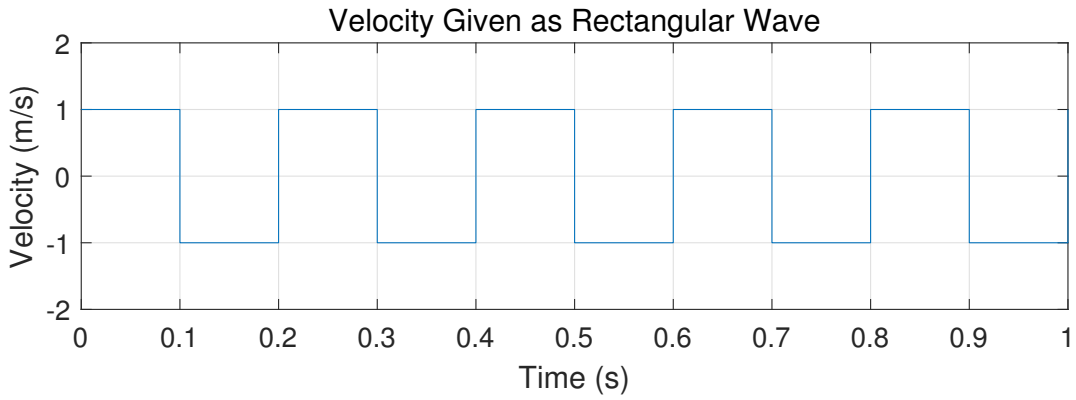

Figure 2.7: Velocity used in friction simulation: rectangular wave

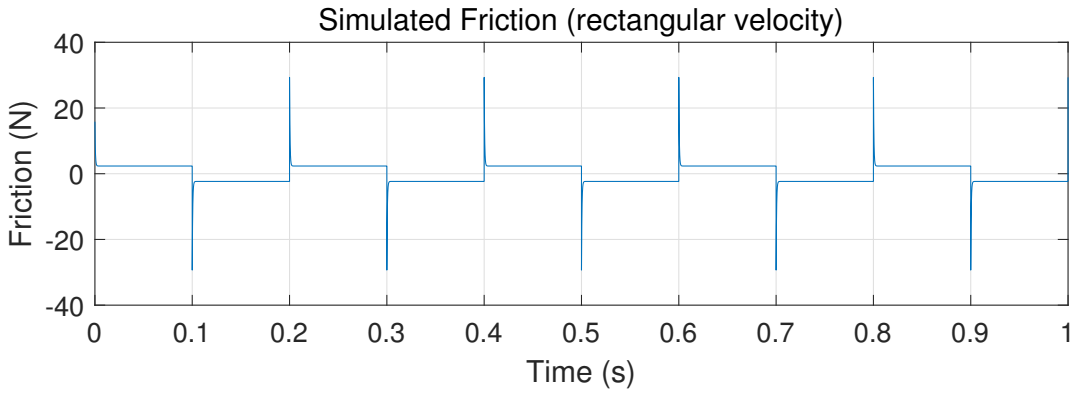

Figure 2.8: Simulated friction corresponding to the velocity given in Fig.2.7

model, simulation results based on the detailed LuGre model are given below. The values of the parameters applied in friction model can be found in Table.2.1.

Fig.2.7 shows the given velocity in the form of rectangular wave. The corresponding simulated friction is presented in Fig.2.8. Pulses on the curve of friction can be found at the timings of rising edges and falling edges of the velocity curve. In addition, Fig.2.9 and Fig.2.10 are the given velocity in the form of sinusoidal wave and corresponding simulated friction respectively. The friction in this case is a clipped sine wave. In both cases, one can identify the nonlinearity of friction with respect to velocity.

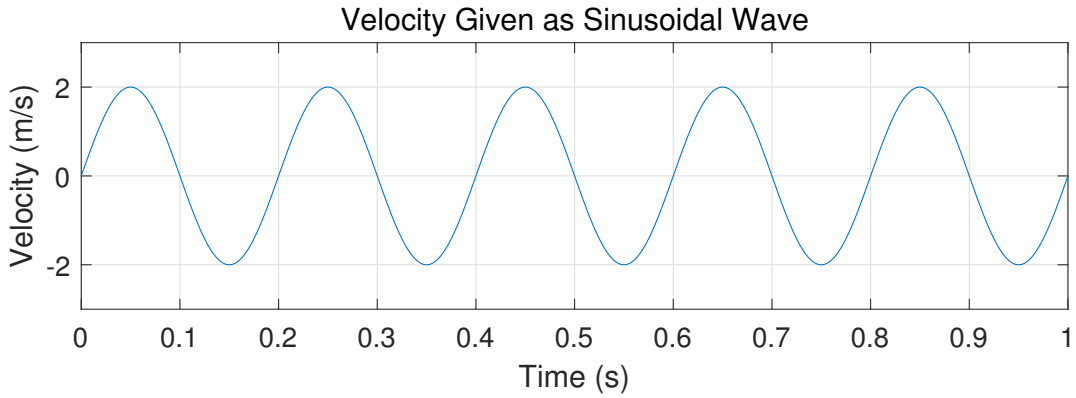

Figure 2.9: Velocity used in friction simulation: sinusoidal wave

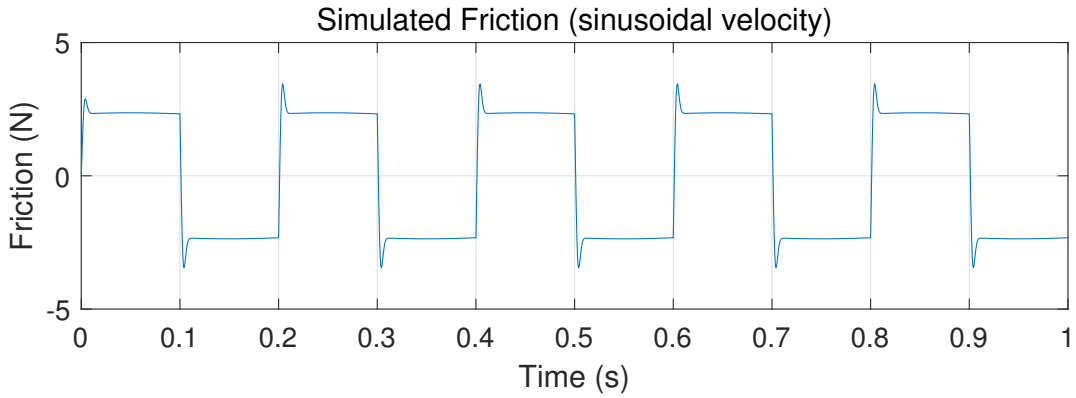

Figure 2.10: Simulated friction corresponding to the velocity given in Fig.2.9

2.3.3 Model of HFRR

As it can be seen from figure 2.1, there is no gearbox installed between the load and the motor shaft. The VCM in operation subjects to the frictions that arise from two tribosystems, which are the contacting surfaces between the test ball and the test plate and the linear guide that supports the test plate. It is noted that the friction arises from the linear guide is in the same direction as that between the test ball and the test plate. Therefore, they are treated as a lumped friction exerts on VCM in modelling. The model of HFRR can be obtained by combining model of VCM and that of frictional load together. Finally, the model of HFRR is:

$$\begin{cases} \dot{x} = v \\ \dot{v} = -\frac{k}{M} \cdot x - \frac{C}{M} \cdot v + \frac{K_s}{M} \cdot i - \frac{1}{M} \cdot F_f \\ \dot{i} = -\frac{K_s}{L} \cdot v - \frac{R}{L} \cdot i + \frac{1}{L} \cdot u_a \end{cases} \tag{2.3.12}$$

where the expression of frictional load F_f can be found in (2.3.11). In general, the developed model of HFRR suggests a 4^{th} order nonlinear system with indifferentiable points in system trajectory. x is the output of the system, which is the position signal of motor shaft. u_a is the input of the system, which is the voltage applied to VCM. It is noted that the model of HFRR here can be regarded as a 3^{rd} order linear system by considering the friction as an unknown load. In fact, for the control design discussed in the following chapters, we use the linear model of (2.3.12), as neither the values of the parameters of friction model nor the accurate sensing of friction is available.

2.4 Prototype of HFRR

2.4.1 Hardware Setup

The setup of the experimental platform applied in research is shown in Fig. 2.11. A DSP is used to implement the controller, which reads in the position, normal force and friction signals from the sensors on HFRR. A full bridge inverter is used to alternate the voltage applied to the terminals of VCM. The inverter is controlled by DSP

through pulse width modulation (PWM) technique. A PC is used to achieve signals monitoring in real time. In Fig. 2.11, an incremental encoder in position sensing module is used to measure the position of the shaft of VCM, of which the resolution is $0.5\mu m$. In addition, A load cell connected with an isolated voltage transducer form the normal force sensing module, which is used to measure the normal force exerted on the specimen during experiments. The conditioned normal force signal passing through isolated voltage transducer is fed into DSP. Similarly, a piezoelectric sensor together with a charge amplifier composes the friction sensing module, of which the output is fed into DSP through AD. The details of the components applied to the experimental platform are given as:

- The DSP with part number TMS320F28379D is equipped with two 32-bit floating-point CPUs, with each core provides 200 MHz of signal processing performance. Its processing capability is further enhanced by trigonometric math unit (TMU) accelerator and complex math and CRC unit (VCU) accelerator. There are several analog and control peripherals that integrated to DSP for the purpose of real-time control applications. In our study, the peripherals and subsystems of interest include Enhanced Pulse Width Modulation (ePWM) module, Enhanced Quadrature Encoder Pulse (eQEP) module, Serial Communications Interface (SCI), Serial Peripheral Interface (SPI), General-Purpose Input/Output (GPIO) and Analog-to-Digital Converter (ADC). ePWM module is used to generate PWM signals to drive power electronics components. eQEP is used to decode the position signal acquired from quadrature encoder. SCI is used to realise duplex communication between PC and DSP. SPI and GPIO are used to achieve communication between DSP and other IC chips [75] [76].

- The 3-phase driver stage applied in the experimental platform is built based on the DRV8305 motor gate driver and CSD18540Q5B NexFET power MOSFET. It supports 4.4 to 45V voltage supply and up to 15A RMS (20A peak) drive current. For each phase, it has been designed with voltage sense and current shunt sense circuits. In our study, as VCM is a two-terminal motor, only

two phases are used to form a full H-bridge driver circuit. The outputs of voltage sense and current sense are fed to DSP through ADC. The On-Off states of the power MOSFETs on the driver stage are controlled by ePWM peripheral on DSP. The gains of the internal current shunt amplifiers are set by DSP through SPI. The driver stage is enabled by DSP through the corresponding GPIO [77] [78].

- The quadrature encoder with part number MII1600 is a reflective optical incremental encoder. The linear tape scale is equipped with a stick-on bidirectional optical index marker for indexing function in repetitive motion application. The grating pitch of the linear tape scale is $20\mu m$. The resolution is improved to $0.5\mu m$ through interpolation method. The differential output signals of the incremental encoder are converted to single-ended form by AM26C32 quadruple differential line receiver and fed to DSP through eQEP module [79] [80] [81].

- The VCM applied to the study is an MKF type linear VCM with the shaft being connected to the test plate that supports by a linear guide. The parameters of the VCM can be found in Table. 2.1 [82] [83].

- In the experiment, the DC power supply connected to the driver stage is a 1kW 42V switch power supply. In addition, the normal force, friction and position sensing modules are powered by a 3-channel regulated DC power supply, which is shown in Fig. 2.11. The parameters of digital controller, full bridge inverter and incremental encoder on the experimental platform are presented in Table. 2.2.

Fig.2.12 shows the completed DSP based experimental platform of HFRR. A PC is used for the purpose of programming of DSP. In addition, the feedback signals such as current, position and friction can be transmitted from DSP to PC through a USB cable in real time during the experiment. The received signals can then be logged for the later signal processing.

Remark II.1: The position counter register of the digital signal processor on the

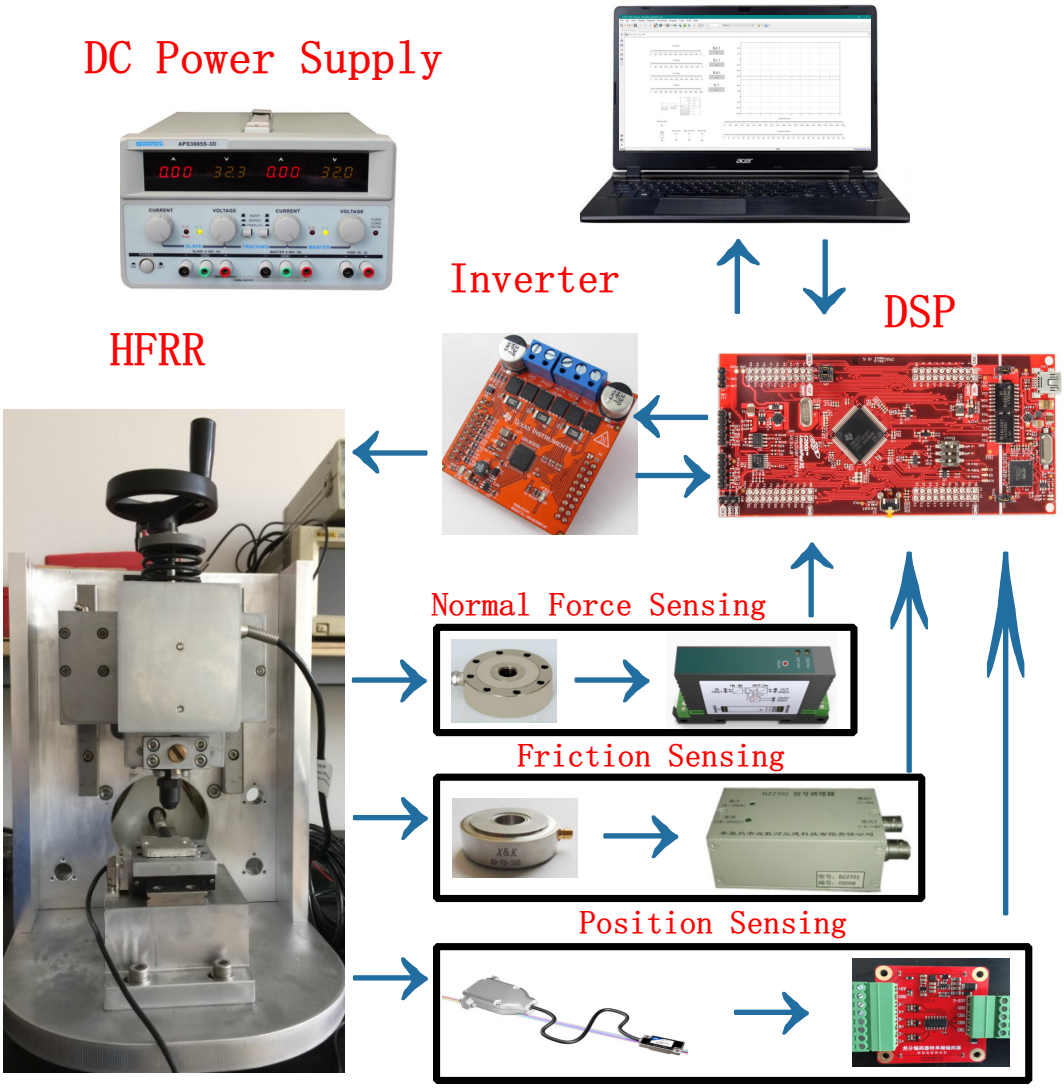

Figure 2.11: Configurations of experimental platform

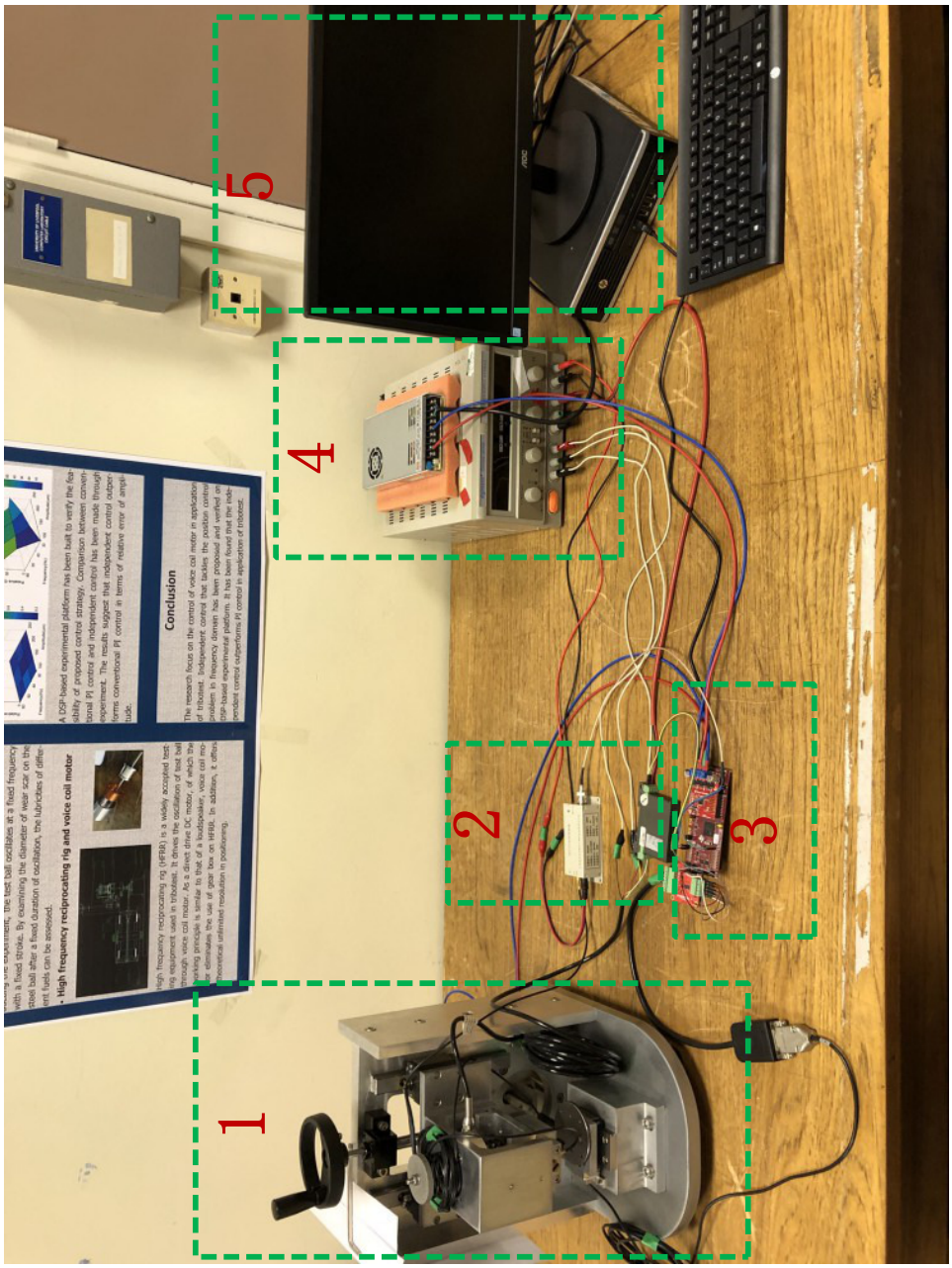

Figure 2.12: DSP based experimental platform of HFRR on the workbench: 1) HFRR with friction force sensor and normal force sensor (the detailed structure of HFRR can be referred to Fig.2.1), 2) friction signal conditioning module (top) and normal force signal conditioning modules (bottom), 3) DSP with driver stage PCB docking on top of it, 4) DC Power Supplies (42V, 24V, 10V, 5V), 5) Host PC with serial communication cable connected to DSP.

Parameter	Symbol(unit)	Value
Coil resistance	R(Ω)	5.4
Coil inductance	L(H)	3.86×10^{-3}
Mass of moving components	M(Kg)	0.512
Motor constant	K_s(N/A)	24
Spring stiffness	k(N/m)	1960
Damping coefficient	C($n.s.m^{-1}$)	2
Asperity stiffness	σ_0 (N/m)	10^5
Damping coefficient	σ_1 (Ns/m)	$10^{\frac{1}{2}}$
Viscous coefficient	σ_2 (Ns/m)	0.4
Coulomb friction	F_c (N)	46.49
Stiction force	F_s (N)	55.3
Stribeck velocity	v_s (m/s)	0.001
Shape factor	σ_{vs} (-)	2

Table 2.1: HFRR model parameters: the parameter values of VCM are taken from [82][83]; the parameter values of friction model are taken from [67].

Parameter	Value
DC Bus Voltage	$42V$
DSP Clock Frequency	$2 \times 10^8 Hz$
PWM frequency	$4 \times 10^4 Hz$
Encoder Resolution	$5 \times 10^{-7} m$

Table 2.2: Parameters of prototype

experimental platform will always be set to a predefined initial value on index events during each cyclic period of oscillation to mitigate potential drift problem

2.4.2 Program Configuration

The program development environment for controller implementation purpose applied in the study is constructed by integrating Code Composer Studio (CCS), ControlSUITE, C2000WARE, MATLAB/SIMULINK and TI C2000 Embedded Coder Support Package. CCS is an integrated development environment (IDE) that supports embedded processors of Texas Instruments [84]. It is based on the Eclipse open source software framework that is free of license. ControlSUITE and C2000WARE are both a set of softwares and driver packages that developed to ease the burden on the coding of embedded processor [85] [86]. TI C2000 Embedded Coder Support Package is an add-on package for MATLAB/SIMULINK that is designed to generate C code for C2000 embedded processor. The algorithms implemented using MATLAB code and SIMULINK models can then be translated into source code and executables. By setting the systems target file corresponding to the DSP applied in the study, the generated code can be directly deployed to TMS320F28379D DSP using the customised MATLAB/SIMULINK that configured specifically for embedded processor coding purpose [87] [88]. In addition, the communication between PC and DSP for the purpose of signals monitoring and parameters tuning in real time can be achieved by calling the built-in instrument driver in instrument control toolbox in MATLAB/SIMULINK [89]. In order to log the signals of interest in experiments, both the program running in DSP and that running on PC need to be developed. To be specific, the main tasks for the two programs are given as follows:

For the program running in DSP, it mainly deals with the following tasks:

- Data acquisition from AD and eQEP
- Digital filtering and signal conditioning
- Realisation of control algorithms
- PWM signals generation

- Data exchange between DSP and PC

For the program running on PC, it mainly deals with the following tasks:

- Data exchange between PC and DSP
- Signals logging and display in real time
- Support for graphical user interface (GUI)

When conducting experiments, the program running in DSP should be loaded and executed at first. Then on PC, the GUI program should be triggered to realise signal monitoring and logging in real time.

In DSP, the signal conditioning function is configured to convert the unsigned raw signals from AD to the meaningful signals with physical units. To eliminate the noise generated by the charge amplifier, digital filtering is introduced in the program. It is noted that the data exchange between DSP and PC is unbalanced. To ease the computation burden of DSP, different working modes for data uploading and downloading in DSP are proposed. The data uploading is executed periodically at the frequency of $5KHz$. However, the data downloading from PC to DSP is executed by triggering an interrupt service routine, by which the tunable parameters such as the amplitude of the reference signal in DSP program can be changed during the time of program execution.

For the program runs in PC, the configurations of data exchange routine are similar to that of DSP, as client and server share the same communication protocol. The data uploaded to PC is logged and displayed in real time through built-in data logging and display functions of the Scope block in SIMULINK. The data is stored in structure type format, which can be accessed for post-processing purpose in MATLAB Workspace at the end of program execution. The interactive user interface is implemented through blocks in Dashboard library.

2.4.3 Discussion on Discretisation

To implement the controller using DSP, it is required that the continuous time controller should be discretised. The output from a discrete time controller is piece-

wise constant over the sampling interval in this case:

$$u = u(nT), \quad nT \leq t < (n+1)T \tag{2.4.1}$$

Where T is sampling period.

For a continuous system with frequency function $G(i\omega)$, when the input of the continuous system is constant over the sampling interval, the corresponding frequency function for the sampled system is given by $G_T(e^{i\omega T})$. The relationship between them can be described by:

$$\left|G(i\omega) - G_T\left(e^{i\omega T}\right)\right| \leq \omega T \cdot \int_0^\infty |g(\tau)| d\tau \tag{2.4.2}$$

where $g(\tau)$ is the impulse response of $G(s)$. As a rule of thumb, the difference between two frequency functions can be regarded as small when the frequency is less than one tenth of the sampling frequency: [90]

$$\omega < \frac{2\pi}{10T} \tag{2.4.3}$$

In experiments, the frequency of PWM by digital signal processor has been set as $40kHz$. In addition, the control algorithm has been set to be executed 1×10^4 times per second. Therefore, the dominated sampling time is $T = 1 \times 10^{-4}s$ for the discrete time controller. The desired frequency of the output position of HFRR in our research is less than $70Hz$. Hence:

$$\omega < 2\pi \times 70 < \frac{2\pi}{10 \times T} \tag{2.4.4}$$

The frequency of interest for HFRR is less than one tenth of the sampling frequency of the discrete time controller. As a result, the difference between the continuous system in analysis and sampled system in experiments can be considered as small.

2.5 Conclusion

HFRR is widely used in pin-on-flat reciprocating tribotest application, where a flat is driven by VCM to achieve reciprocating motion with respect to a pin or ball component. In this chapter, the model of HFRR is constructed by combining the

model of VCM and that of friction. The result shows a fourth order nonlinear system with indifferentiable points in system trajectory. It is the dynamic equations of friction that contributes to the complexity of the system. In order to verify the proposed control methods for HFRR in the following chapters, a DSP-based experimental platform has been built and shown in detail. The key components of the experimental platform include VCM, DSP, full-bridge inverter and incremental encoder. The programs for both PC and DSP are developed through automatic C code generation for embedded processors function in MATLAB/SIMULINK environment, which is achieved by integrating customised MATLAB/SIMULINK, CCS and relevant softwares and driver packages provided by TI. In addition, the main tasks for both programs are shown and discussed. As the controllers in this thesis are designed in the form of continuous time controller and implemented using DSP, the differences between the discretised controllers and the original controllers are discussed in the last section of this chapter. It concludes that the differences between the continuous systems in analysis and sampled systems in experiments can be considered as small.

Chapter 3

Direct Amplitude Control with Amplitude as Performance Index

3.1 Introduction

The controllers for VCM in open literature target to control the real-time position to track a given sinusoidal reference. However, the control objective of a VCM based HFRR is to maintain a constant magnitude of the position signal at high frequency oscillation, rather than to drive the position signal to track the reference in real time. This is required in the assessment standard ISO-12156-1:2016 [7]. Based on author's best knowledge, there is no controller design published to directly regulate the magnitude of the position signal of VCM. This chapter proposes direct amplitude control of the position of VCM based HFRR. It takes the amplitude rather than the position as the performance index to achieve amplitude regulation of VCM. The proposed controller includes a short time Fourier transform (STFT) based amplitude regulation module and an offset compensator. Simulations and experiments to verify the proposed control method are shown. The comparisons among the proposed control method, PR control and conventional PI control are presented as well.

3.2 Direct Amplitude Control Design

3.2.1 Direct Amplitude Control

The position control of motor is usually regarded as a reference tracking problem, of which the aim is to minimise the error between the measured position signal and reference signal. The most popular controller is PI controller, which is shown in (3.2.1):

$$G_{pi}(s) = k_p + \frac{k_i}{s} \tag{3.2.1}$$

where k_p and k_i are proportional gain and integral gain. A conventional PI controller in stationary reference frame can lead to steady state amplitude and phase error when tracking a sinusoidal reference [91]. According to internal model principle, a compensator with a sinusoidal transfer function can be applied to the system in this situation [92]. It has been proved that the steady state error can be zero once the closed system is asymptotically stable. The transfer function of the controller is shown in (3.2.2). It consists of a proportional term and a resonant term.

$$G_{pr}(s) = k_p + \frac{k_i \cdot s}{s^2 + \omega_0^2} \tag{3.2.2}$$

ω_0 is the angular frequency of the sinusoidal reference. k_p and k_i are proportional gain and resonant gain.

Recall the operation of HFRR, which requests maintain a constant amplitude of vibration at the desired frequency and small midpoint offset during experiments. The phase of the position signal is of no concern in application. Therefore, the proposed control method is designed to achieve the following aims:

1. Maintain constant amplitude of vibration
2. Maintain constant frequency of vibration
3. Suppress DC component (offset of midpoint)

The basic idea is to adjust the amplitude of the position signal by varying the amplitude of sinusoidal voltage signal applied between the terminals of VCM. In addition, a varying DC voltage is applied to fight against the drift of midpoint of the position

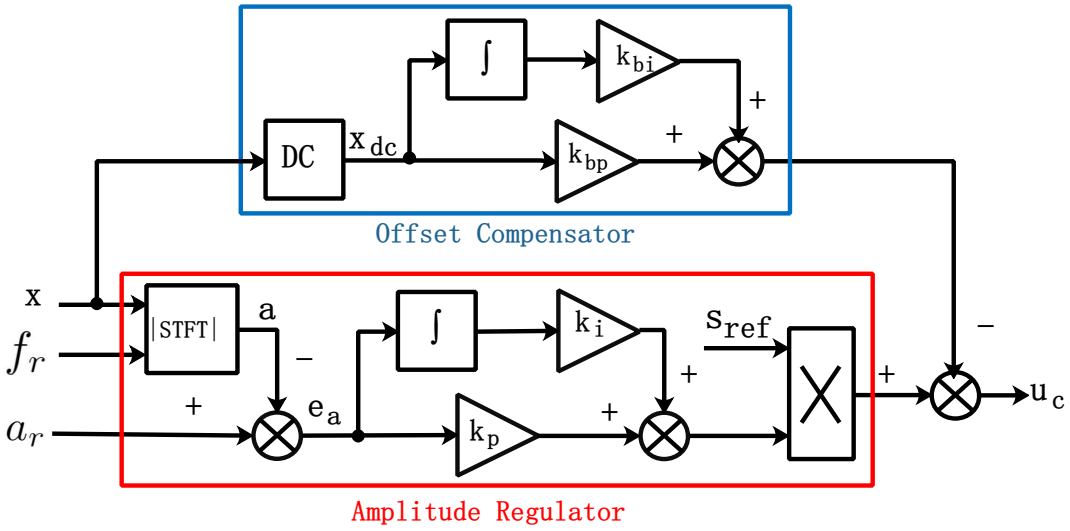

Figure 3.1: Direct amplitude controller

signal. According to the results of the open loop response test of HFRR, the fundamental frequency of output signal is the same as that of the input signal. As a result, the controller can adjust the frequency, amplitude and offset of the output signal separately.

Fig. 3.1 shows the structure of such controller. The controller takes the desired amplitude, desired frequency and feedback position signal as inputs, it outputs the voltage signal applied to the motor. There are two modules in the controller, namely, amplitude regulator module, and offset compensator module. Different from traditional PI control that directly takes the error of position in real time as input, the amplitude regulator module of the proposed controller applies short time Fourier transform (STFT) to the feedback position signal to obtain the amplitude of it at first. Then, it is the error of amplitude rather than error of position being sent to a built-in PI controller. In addition, different from traditional PI control that directly applies its output to the plant under control, the built-in PI controller in amplitude regulator module uses its output to modulate the amplitude of a sinusoidal signal applies to the plant under control. The controller output u_c in time domain can be expressed as:

$$u_c = \left(k_p \cdot e_a + k_i \cdot \int_0^t e_a \cdot dt\right) \cdot s_{ref} - k_{pb} \cdot x_{dc} - k_{ib} \cdot \int_0^t x_{dc} \cdot dt \quad (3.2.3)$$

where

$$\begin{cases} s_{ref} = sin(2\pi \cdot f_r \cdot t) \\ e_a = a_r - a \\ a = \mid \left(\int_{-\infty}^{+\infty} w\left(t-\tau\right) x\left(\tau\right) e^{-j\cdot 2\pi f_r \tau} d\tau \right) \mid \\ x_{dc} = \left(\int_{-\infty}^{+\infty} w\left(t-\tau\right) x\left(\tau\right) d\tau \right) \end{cases} \tag{3.2.4}$$

f_r is the desired frequency of output position signal. e_a is the error of amplitude. a_r is the desired amplitude of position signal x based on STFT. x_{dc} is the windowed DC component in output position signal. k_p and k_i are proportional gain and integral gain of amplitude regulator module. k_{pb} and k_{pi} are proportional gain and integral gain of offset regulator module. In implementation, a is obtained by taking the modulus of the short time Fourier transform of the output signal.

$$a\left(t\right) = \mid \int_{t-\frac{1}{f_r}}^{t} w^{TS}\left(t-\tau\right) x\left(\tau\right) e^{-j\cdot 2\pi f_r \tau} d\tau \mid \tag{3.2.5}$$

where, the time-shifted Hamming window $w^{TS}\left(t\right)$ is:

$$w^{TS}\left(t\right) = 0.54 - 0.46cos\left(2\pi f_r t\right), 0 \leq t \leq \frac{1}{f_r} \tag{3.2.6}$$

3.2.2 Convergence Analysis

The transfer function of HFRR without friction can be obtained from equation (2.3.6) as:

$$\frac{X(s)}{U_a(s)} = \frac{K_s}{LM \cdot s^3 + (LC + RM) \cdot s^2 + (K_s^2 + RC + Lk) \cdot s + Rk} \tag{3.2.7}$$

where $X(s)$ is the position of VCM in s domain and $U_a(s)$ is the voltage applied to VCM in s domain.

The denominator of the transfer function of HFRR without friction is:

$$\begin{aligned} P\left(s\right) = LM \cdot s^3 + (LC + RM) \cdot s^2 + \\ \left(K_s^2 + RC + Lk\right) \cdot s + Rk \end{aligned} \tag{3.2.8}$$

Therefore, the characteristic equation of HFRR transfer function without friction is:

$$P\left(s\right) = 0 \tag{3.2.9}$$

Substitute the values listed in the Table. 2.1 into (3.2.9), we can obtain:

$$0.0021s^3 + 2.8893s^2 + 594.3656s + 10584 = 0 \tag{3.2.10}$$

The poles of the HFRR transfer function are:

$$\begin{aligned} p_1 &\approx -19.65964 < 0 \\ p_2 &\approx -225.87700 < 0 \\ p_3 &\approx -1157.17522 < 0 \end{aligned}$$

Remark III.1: HFRR as a system without friction is open loop stable.

The proposed controller in s domain can be expressed as:

$$C(s) = \left[(k_p + \frac{k_i}{s}) * \frac{\omega_r}{s^2 + \omega_r^2}\right] \cdot E_a(s) - (k_{pb} + \frac{k_{ib}}{s}) \cdot X_{dc}(s) \tag{3.2.11}$$

$$= \left[k_p * \frac{\omega_r}{s^2 + \omega_r^2} + \frac{k_i}{s} * \frac{\omega_r}{s^2 + \omega_r^2}\right] \cdot E_a(s) - (k_{pb} + \frac{k_{ib}}{s}) \cdot X_{dc}(s) \tag{3.2.12}$$

where $*$ indicate convolution and $\omega_r = 2\pi f_r$. According to the definition of convolution, expression (3.2.12) in frequency domain can be written as:

$$\begin{aligned} C(j\omega) = &\left[\int_{-\infty}^{\infty} k_p \cdot \frac{\omega_r}{(j\omega - ju)^2 + \omega_r^2} du + \int_{-\infty}^{\infty} \frac{k_i}{ju} * \frac{\omega_r}{(j\omega - ju)^2 + \omega_r^2} du\right] \cdot E_a(s) \\ &- (k_{pb} + \frac{k_{ib}}{j\omega}) \cdot X_{dc}(j\omega) \end{aligned} \tag{3.2.13}$$

rearrange the above equation and express it in s domain as:

$$C(s) = \frac{k_i \omega_r}{s^2 + \omega_r^2} \cdot E_a(s) - (k_{pb} + \frac{k_{ib}}{s}) \cdot X_{dc}(s) \tag{3.2.14}$$

Assumption III.1: the friction as a disturbance is differentiable and bounded. Then it satisfies matching condition, where the disturbance can be transferred to act on the system via the same channel as control input [52].

Fig. 3.2 shows the block diagram of HFRR considering friction. Once the matching condition is fulfilled, the friction as disturbance can be transferred to an equivalent input disturbance $D(s)$ as shown in Fig. 3.3. Therefore, the output of the closed

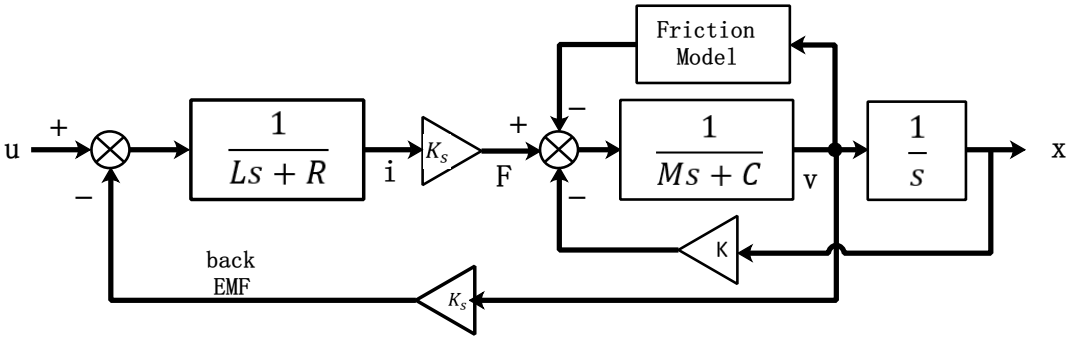

Figure 3.2: Block diagram of HFRR including friction

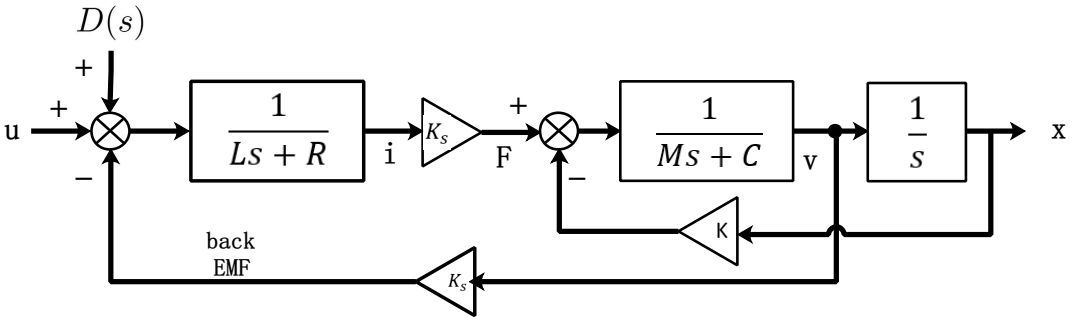

Figure 3.3: Modification on the model of HFRR including friction: the friction can be transferred to act on HFRR via the same channel as control input (shown as $D(s)$ in (b)).

loop system in frequency domain can be expressed as:

$$X\left(s\right)=G\left(s\right)\cdot\left[\frac{k_i\omega_r}{s^2+\omega_r^2}\cdot E_a(s)-(k_{pb}+\frac{k_{ib}}{s})\cdot X_{dc}(s)\right]+G\left(s\right)\cdot D\left(s\right) \tag{3.2.15}$$

where the plant model $G\left(s\right)$ and equivalent input disturbance $D\left(s\right)$ are given as:

$$\begin{cases} G\left(s\right) & =\frac{K_s}{P(s)} \\ D\left(s\right) & =-\frac{(L\cdot s+R)}{K_s}\cdot F_f\left(s\right) \end{cases} \tag{3.2.16}$$

The output of the closed loop system can be decomposed into sinusoidal component $X_{ac}(s)$ and generalised output disturbance $X_{dis}(s)$ as:

$$X(s)=X_{ac}(s)+X_{dis}(s) \tag{3.2.17}$$

where

$$\begin{cases} X_{ac}\left(s\right) & =G(s)\cdot\frac{k_i\omega_r}{s^2+\omega_r^2}\cdot E_a(s) \\ X_{dis}\left(s\right) & =G(s)\cdot\left[D(s)-(k_{pb}+\frac{k_{ib}}{s})\cdot X_{dc}(s)\right] \end{cases} \tag{3.2.18}$$

Assumption III.2: perfect knowledge of $a(t)$ and $x_{dc}(t)$ can be obtained. Then, $e_a(t)$ can be approximated as error of amplitude in real time. In addition, $x_{dc}(t)$ is nonzero for only DC component in output signal.

As the disturbance is assumed to be bounded and $x_{dc}(t)=0$ for sinusoidal component of the output signal, output of the system in s domain ignoring DC offset can be expressed as:

$$\begin{aligned} X(s) &= G(s)\cdot\frac{k_i\omega_r}{s^2+\omega_r^2}\cdot E_a(s)+G(s)\cdot[D(s)-(k_{pb}+\frac{k_{ib}}{s})\cdot 0] \\ &= G(s)\cdot\left(\frac{k_i\omega_r}{s^2+\omega_r^2}\cdot E_a(s)+D(s)\right) \end{aligned} \tag{3.2.19}$$

The magnitude of the component at the desired frequency considering disturbance can be expressed as:

$$\begin{aligned} |X(j\omega_r)| &= |G(j\omega_r)\cdot\left[\frac{k_i\omega_r}{s^2+\omega_r^2}\cdot E_a(j\omega_r)+D(j\omega_r)\right]| \\ &\leq |G(j\omega_r)|\cdot|\left[\frac{k_i\omega_r}{s^2+\omega_r^2}\cdot E_a(j\omega_r)+D(j\omega_r)\right]| \end{aligned} \tag{3.2.20}$$

Therefore, we have:

$$|X(j\omega_r)| \leq |G(j\omega_r)| \cdot [k_i \cdot (a_r - |X(j\omega_r)|) + D(j\omega_r)] \tag{3.2.21}$$

Here we define the equivalent uncertainty of the control input of HFRR as Δ, such that:

$$|X(j\omega_r)| = |G(j\omega_r)| \cdot [k_i \cdot (a_r - |X(j\omega_r)|) + \Delta] \tag{3.2.22}$$

Rearrange the last line of (3.2.22), we have:

$$|X(j\omega_r)| = \frac{|G(j\omega_r)| \cdot k_i}{1 + |G(j\omega_r)| \cdot k_i} \cdot (a_r + \frac{\Delta}{k_i}) \tag{3.2.23}$$

Remark III.2: At steady state, arbitrarily small error of amplitude at the desired frequency can be achieved by choosing $k_i \gg 1$ (The order of magnitude in practice is set to be 10^3). And we have:

$$\lim_{k_i \to \infty} |X(j\omega_r)| = a_r \tag{3.2.24}$$

Considering the DC component of the output signal at steady state, we have:

$$\begin{aligned} X(j0) &= X_{ac}(j0) + X_{dis}(j0) \\ &= 0 + X_{dis}(j0) \\ &= G(j0) \cdot \left[D(j0) - (k_{pb} + \frac{k_{ib}}{j0}) \cdot X(j0) \right] \end{aligned} \tag{3.2.25}$$

Hence,

$$\frac{X(j0)}{D(j0)} = \frac{G(j0)}{k_{pb} + \frac{k_{ib}}{j0}} \tag{3.2.26}$$

Remark III.3: At steady state, the DC component of the output signal $X(j0) \to 0$.

As a result, the system is open loop stable. By assuming the fulfilment of matching condition and perfect knowledge of amplitude and DC offset, it can be proved that arbitrarily small error of amplitude of the closed loop system at the desired frequency can be achieved at steady state. In addition, the DC offset of the position signal of the closed loop system approaches zero at steady state.

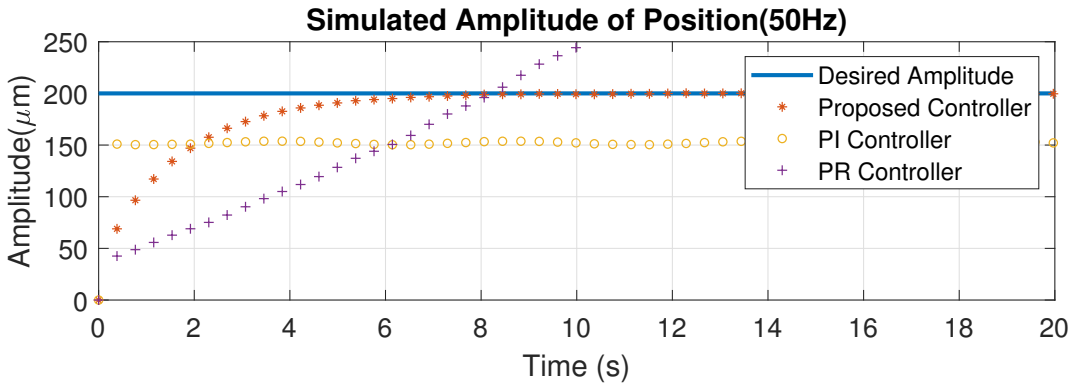

Figure 3.4: Simulated amplitudes of position signals using different controllers

3.3 Simulations

In simulation, the desired amplitude of vibration at 50Hz is set as 200um. Table. 2.1 gives the values of the parameters applied in simulation.

The parameter values of VCM in Table.2.1 are taken from references [82] [83], which are the manuals of products equipped with the same VCM applied in the research. The parameter values of friction model are taken from reference [67], which is a highly cited journal paper on friction model.

On the one hand, the order of magnitude of the simulated friction based on [67] is comparable with what we observed from our experiments. On the other hand, the actual parameter values of the model corresponding to the specimen with lubricant applied in our research are not available from open literature as far as we known. In addition, the measurements of parameter values in experiments can be difficult as there is no reasonable confidence in the accuracy of friction sensor. Therefore, we refer to [67] for the parameter values of friction model for the purpose of simulations.

Fig. 3.4 shows the simulated amplitudes of position signals using different controllers. It is assumed that the shaft of VCM is at standstill initially. It can be found that the amplitude of position signal using the proposed controller converges to the desired value. There is steady state error of amplitude exists for PI controller, which is in agreement with [91]. In addition, when applying PR controller to HFRR, the closed loop system become unstable.

By ignoring the effect of frictional load, the transfer function of the closed loop system under no load condition using PR control can be obtained. Fig. 3.5 shows the root locus plot of the closed loop system using proportional control. The gain varies from 0 to 5×10^4. The corresponding loop transfer function is given by:

$$L_p(s) = \frac{K_p K_i}{P(s) + K_p K_s} \tag{3.3.1}$$

By applying Routh's stability criterion, the closed loop system is stable when $K_p < 33639.48796$. Let $K_p = 10$, the loop transfer function of the closed loop system using proportional resonant control can be expressed as:

$$L_{pr}(s) = \frac{K_s}{P(s)} \cdot \frac{K_p \cdot s^2 + K_i \cdot s + K_p \cdot \omega_0^2}{s^2 + \omega_0^2} \tag{3.3.2}$$

Fig. 3.6 shows the root locus plot of the closed loop system using proportional resonant control with $K_p = 10, \quad \omega_0 = 100\pi$. The gain varies from 0 to 5×10^4. By applying Routh's stability criterion, it is found that there is no positive resonant gain that lead to stable system. Fig. 3.7 shows the magnified view of Fig. 3.6, which clearly shows the conjugate pole pairs on the right hand side of imaginary axis [93].

3.4 Experiment Results

To simplify the experiments, we keep the types of specimen and values of normal force constant in each test. The settings of remaining experimental conditions applied in experiments are shown in Table. 3.1.

In Table 3.1, there are 16 sets of experimental conditions. The frequency varies from 30Hz to 60Hz. The amplitude varies from $100\mu m$ to $250\mu m$. The specimens in all experiments are chosen as aluminium plate with petroleum ether (Al&PE) covered on top of them. To make sure the initial conditions such as surface roughness are same in each experiment, both aluminium plate and petroleum ether between contacting surfaces should be replaced at the end of each test. To assess the performance of the proposed control method, comparisons among conventional PI control, PR control and the proposed control method have been done. The parameters for

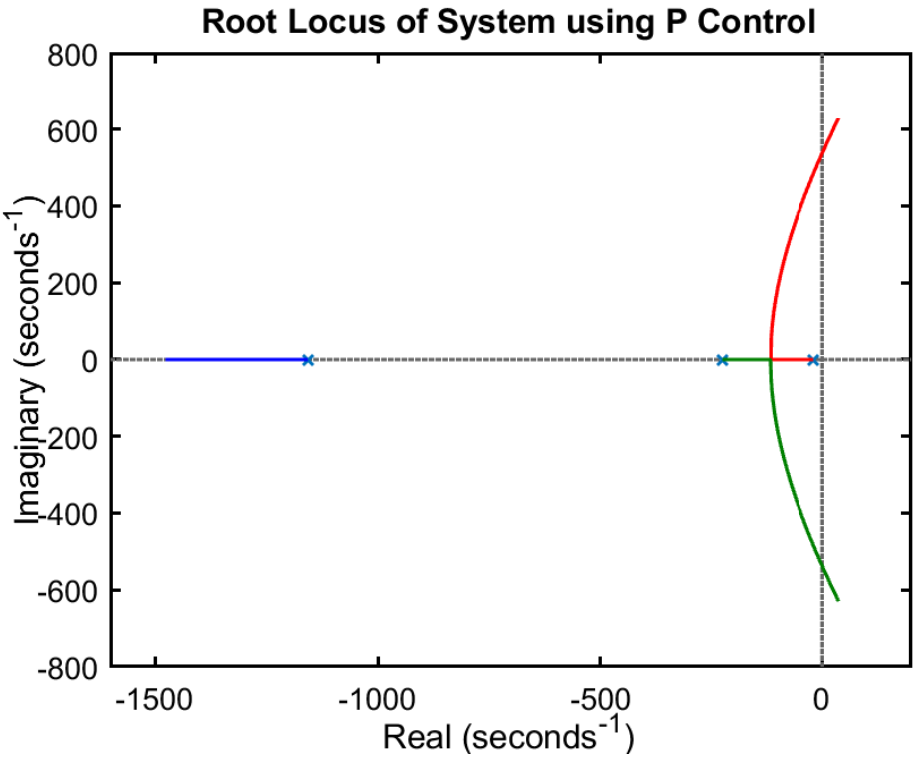

Figure 3.5: Root locus plot of the closed loop system using proportional control

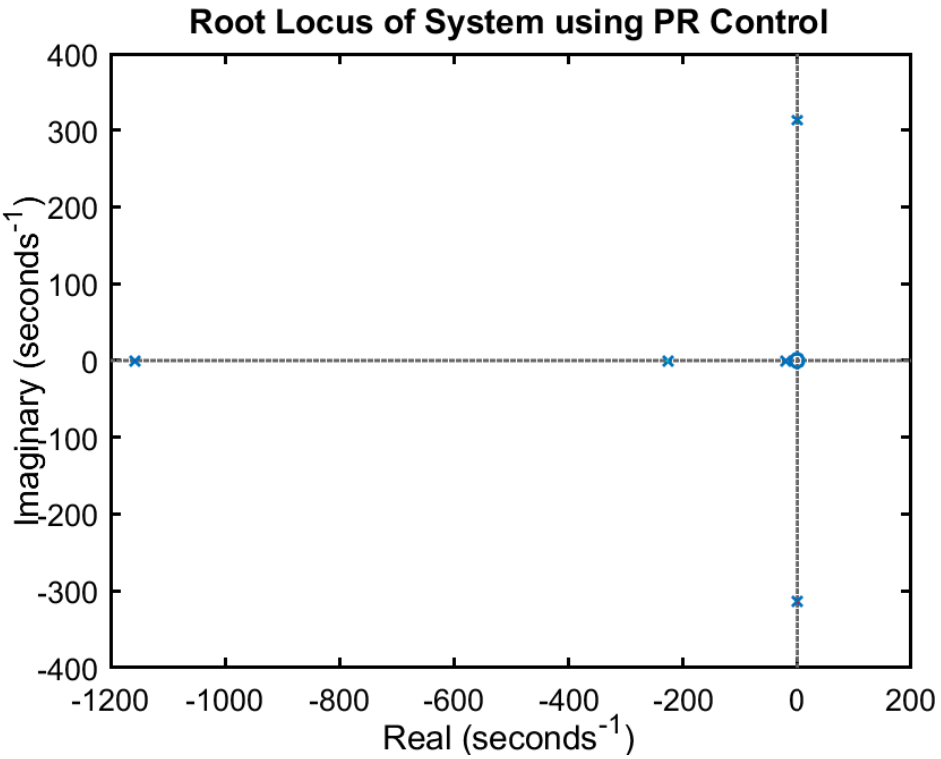

Figure 3.6: Root locus plot of the closed loop system using proportional resonant control with $K_p = 10$ (K_i is varying)

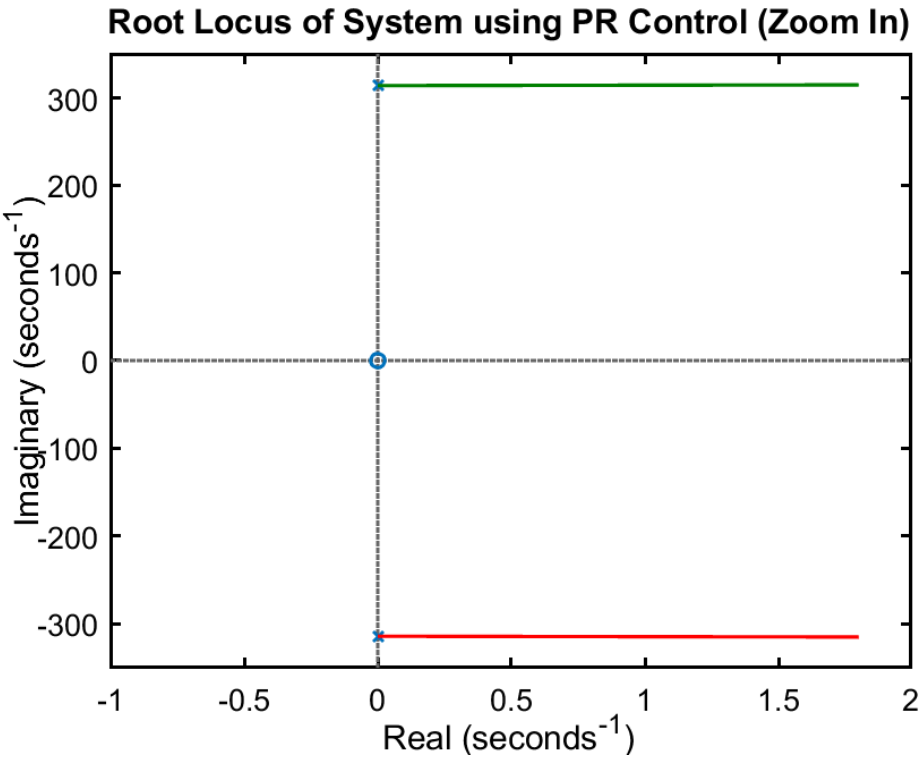

Figure 3.7: Root locus plot of the closed loop system using proportional resonant control with $K_p = 10$ (K_i is varying) (Zoom In)

Frequency(Hz)	Amplitude(μm)
30Hz	100μm
30Hz	150μm
30Hz	200μm
30Hz	250μm
40Hz	100μm
40Hz	150μm
40Hz	200μm
40Hz	250μm
50Hz	100μm
50Hz	150μm
50Hz	200μm
50Hz	250μm
60Hz	100μm
60Hz	150μm
60Hz	200μm
60Hz	250μm

Table 3.1: Experimental conditions

each controller are tuned under the condition shown in Table. 3.2, and then keep constant in remaining tests.

Fig. 3.8 shows the amplitudes of position signals using PR controller at different frequencies. The desired amplitude is set as 200μm. It can be found that the amplitudes of position signals corresponding to each frequency always keep increasing, which indicates an unstable system.

Fig. 3.9 and Fig. 3.10 are the amplitudes of position signals acquired in experiments using PI and the proposed controllers. The desired values of amplitude are all set as $200um$. It can be found that the performance of the conventional PI control in terms of amplitude degrades significantly as frequency increases. However,

Frequency(Hz)	Amplitude(μm)	Specimen	Normal Force(N)
30Hz	100μm	Al&PE	6N

Table 3.2: Experimental conditions for controllers tuning

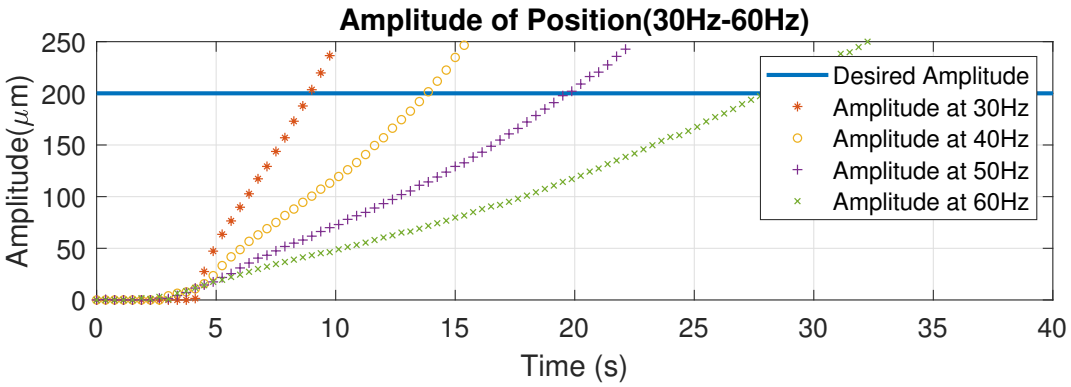

Figure 3.8: Amplitudes of experimental position signals at different frequencies using PR control

the proposed control method shows the ability of amplitude keeping at different frequencies. Fig. 3.11 and Fig. 3.12 are the position signals acquired in experiments using PI and the proposed controllers. The desired values of amplitude are all set as $200\mu m$. In addition, the normal force is changed to 10N when obtaining Fig.3.13. It can be found that the convergence of amplitude error can still be guaranteed.

It can be found that the magnitude of relative error increases at higher frequency using conventional PI control. The relative errors of amplitudes given by the proposed control method all converge to zero at different frequencies. The rate of convergence depends on the frequency of vibration. Fig. 3.14 are the outputs of PI controller and the proposed controller at 30Hz with the desired amplitude of $200\mu m$. The control efforts are similar.

Fig. 3.15 and Fig. 3.16 show the relative errors of amplitude for both conventional PI controller and the proposed controller at steady states. The proposed control outperforms the conventional PI control significantly in terms of amplitude keeping. The relative errors of amplitude using the proposed controller are less than 0.5% in all 16 experiments. The conventional PI controller presents higher relative

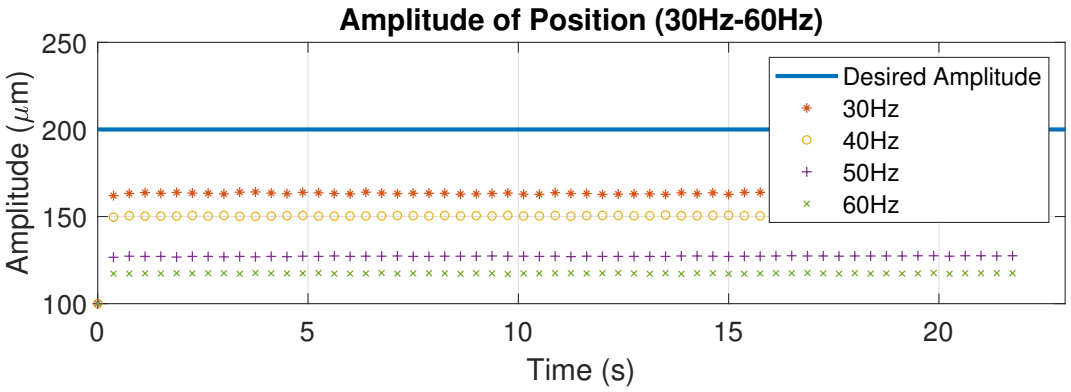

Figure 3.9: Amplitude of experimental position signals at different frequencies using PI control

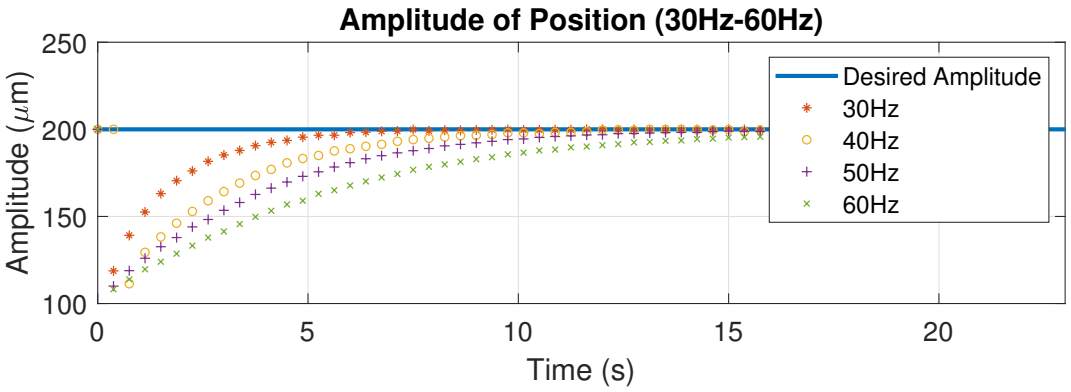

Figure 3.10: Amplitude of experimental position signals at different frequencies using the proposed control method

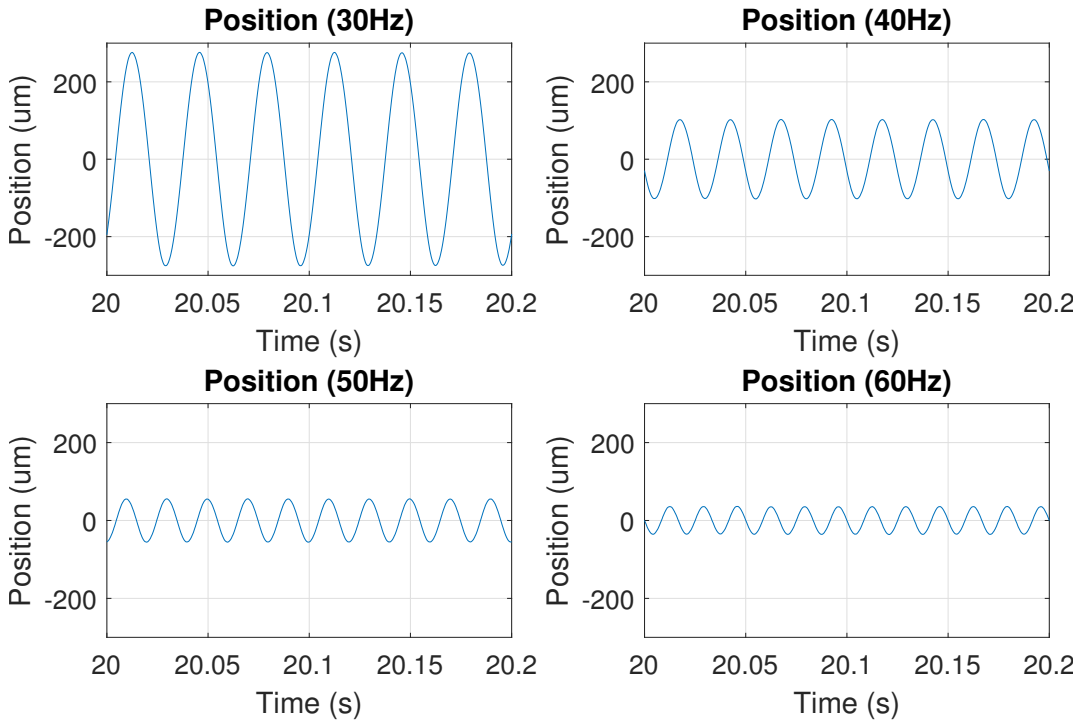

Figure 3.11: Experimental position signals at different frequencies using PI control

error as either amplitude or frequency increasing. At 60Hz, the relative error of amplitude can be as large as 80%. On the contrary, the relative error of amplitude using the proposed controller decreases as either amplitude or frequency increasing. This implies that the proposed control algorithm is attractive for application of vibration control in high frequency band. In both situations, the relative offsets are always less than 1%, which is of little difference.

Fig. 3.17 and Fig. 3.18 show the total harmonic distortions (THD) of position signals at steady states under different conditions. THD applied in the analysis is determined from the fundamental frequency of vibration and the first three harmonics of position signal acquired from corresponding test. This is used to assess the frequency keeping ability of control algorithm. At 30Hz, THD of position signal using conventional PI control is less than that using the proposed controller. However, at higher frequencies, the performance of proposed control in terms of harmonics suppression is better than that of conventional control. This observation agrees with the conclusion that the proposed control algorithm is attractive for application of

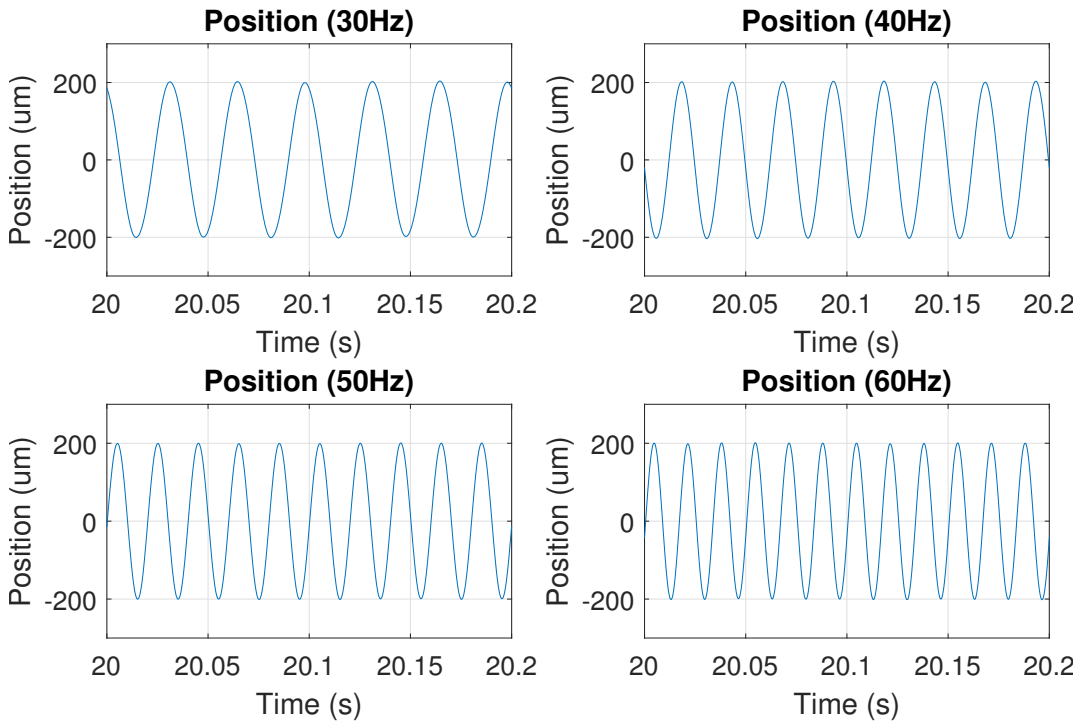

Figure 3.12: Experimental position signals at different frequencies using the proposed control method

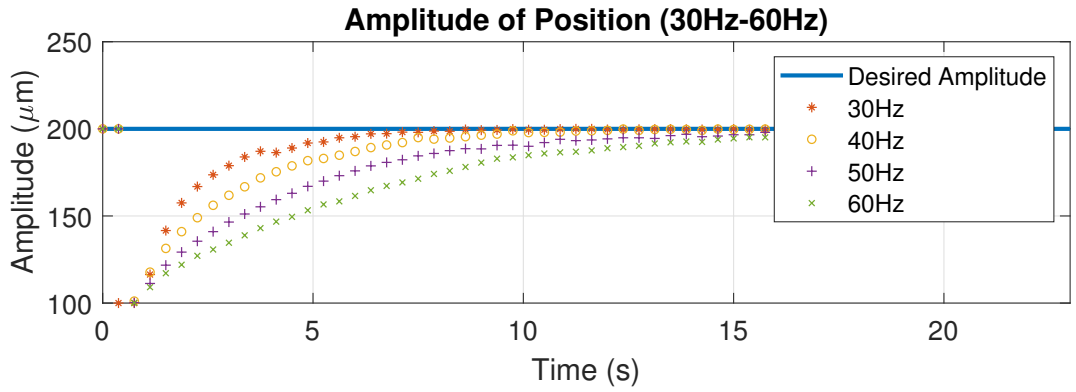

Figure 3.13: Amplitude of experimental position signals at different frequencies using the proposed control method with 10N normal force

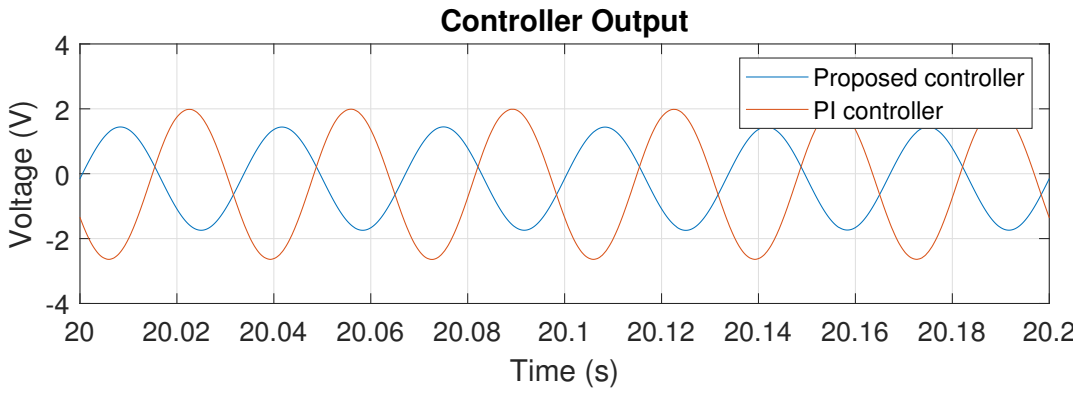

Figure 3.14: PI controller output at 30Hz

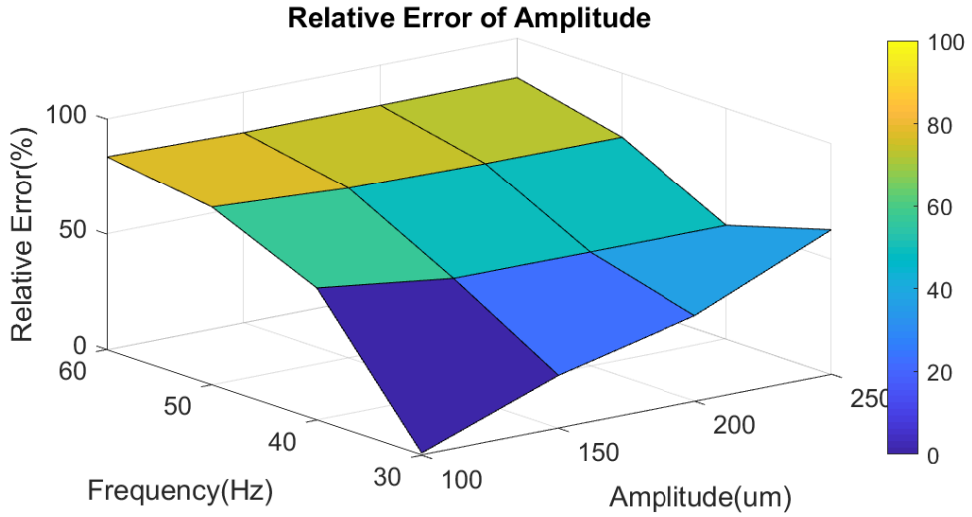

Figure 3.15: Relative errors of amplitude using PI control under different conditions

vibration control in high frequency band in tribotests.

Remark III.4: In addition, as VCM is also applied to the design of electrodynamic shaker in vibration test systems, the proposed control method can be applied to the regulation of the amplitude of acceleration of the shaker in vibration tests, where the encoder is replaced by accelerometer [94] [95].

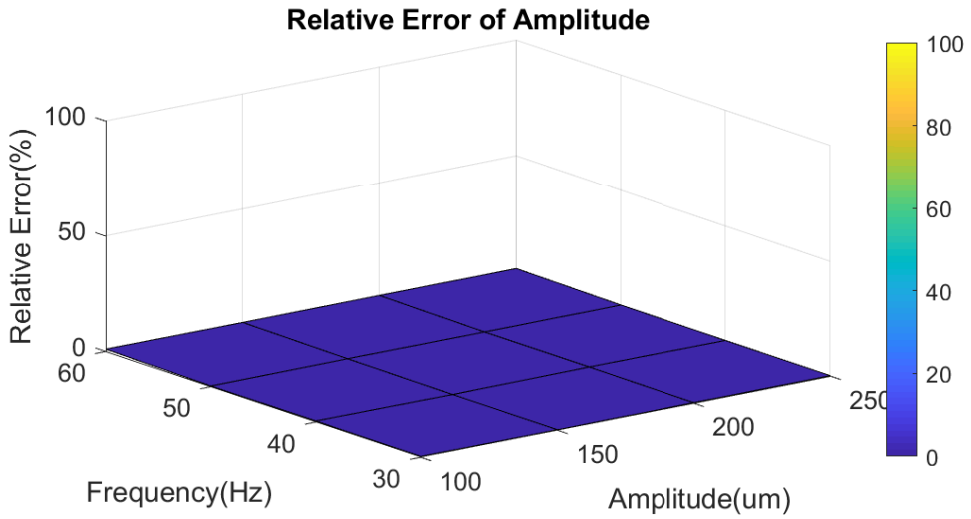

Figure 3.16: Relative errors of amplitude using the proposed control under different conditions

3.5 Conclusion

Direct amplitude control is proposed to deal with the amplitude keeping problem of HFRR subjects to frictional load. The proposed control scheme consists of an amplitude regulator and an offset compensator. It takes the error of the amplitude of the position signal as the performance index. The analysis shows that the error of amplitude of position signal of the closed loop system converges to zero by applying the proposed control. A DSP based experimental platform is applied to verify the proposed control method. Both PI control and PR control are introduced to experiments for the purpose of comparison. Although PR control has been widely applied in the application of tracking sinusoidal reference signal, it leads to an unstable system due to the large phase delay of VCM based HFRR at high frequency band. It is found that the proposed direct amplitude control outperforms PI control in terms of amplitude keeping and harmonics suppression in high frequency reciprocating motion.

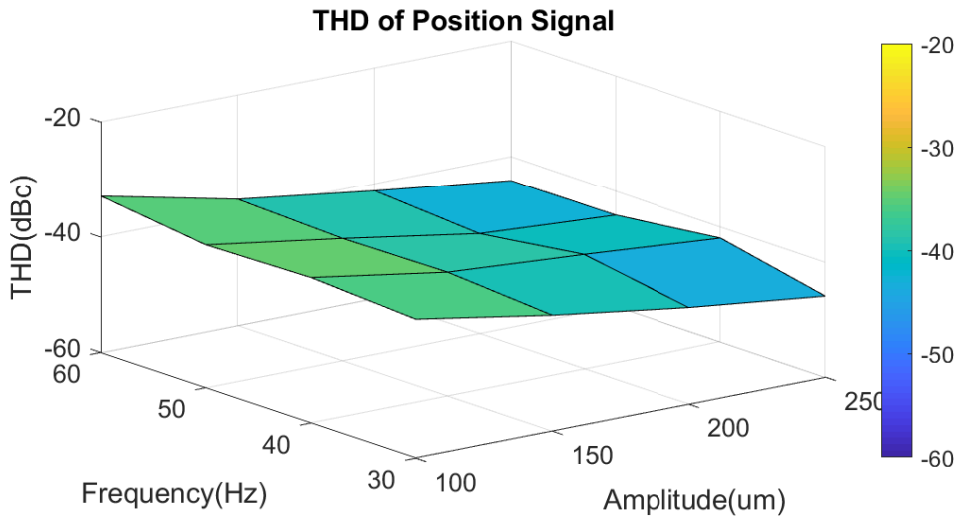

Figure 3.17: Total harmonic distortions of position signals using PI control under different conditions

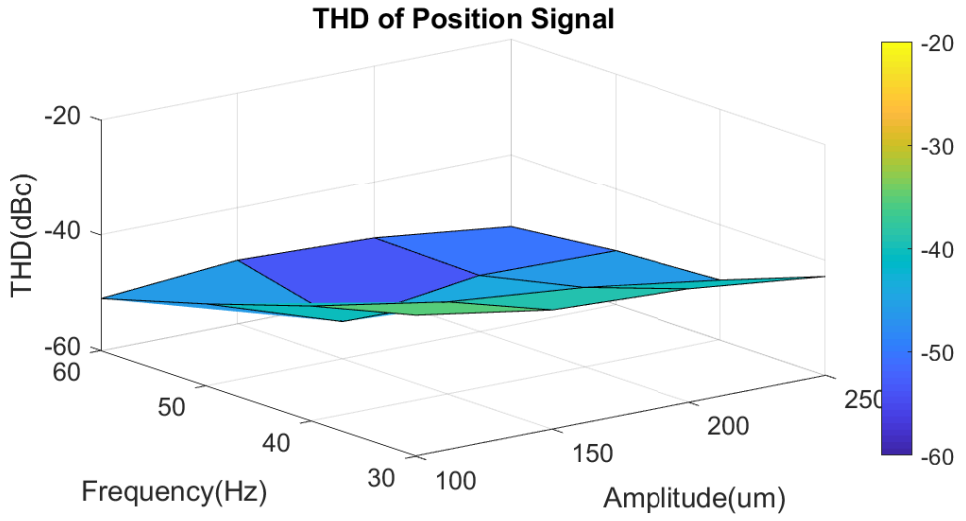

Figure 3.18: Total harmonic distortions of position signals using the proposed control under different conditions

Chapter 4

Acceleration Based Control with Time Domain Disturbance Observer

4.1 Introduction

Motion control has been a hot topic in the study of mechatronics, which can be classified according to the output of the mechanical system, such as position control and force control [96]. Compliance is used as a simplified index to quantitatively represent the requirements of motion control corresponding to different selections on the output of the mechanical system, which is defined as a relative change in position due to a change in interaction force. Therefore, in the case of position control, compliance should be as small as possible to mitigate the impact of input disturbances. On the contrary, in the case of force control, compliance should be as large as possible to maintain the desired force regardless of position. In order to set a common goal for motion control in different situations, acceleration based control is applied to mechatronics study, of which the goal is described as maintaining control error zero despite changes in system dynamics [97].

From the motion control point of view, the control of VCM on HFRR can be formulated as a reference position tracking problem for a single degree of freedom mechanical system subject to frictional load. In this chapter, we apply acceleration based control method to VCM, where the design of a task controller that synthesise

the desired system acceleration and the construction of a disturbance compensation module that estimate and compensate for the input disturbance are involved. By assuming the relatively slow variation of frictional force and matching condition, the frictional force that distorts the output signal can be compensated through the reduced order disturbance observer at the input of the plant. In addition, simulations and experiments to verify the control method are presented.

4.2 Acceleration Based Control

The structure of the closed loop system within the framework of acceleration control applied to a single degree of freedom mechanical system is shown in Fig. 4.1 [97]. It consists of a task controller that synthesise the desired system acceleration and a disturbance compensation module that estimate and compensate for the input disturbance F_d. The plant dynamics is represented as a double integrator with acceleration $\ddot{x}$. In the framework of acceleration, the control of a mechanical system is implemented by firstly determining acceleration as a virtual input and then exerting the force necessary to enforce the desired acceleration. In Fig. 4.1, M is the mass of the moving component on a mechanical system under control; x, $\dot{x}$ and $\ddot{x}$ are position, velocity and acceleration of the moving component; $y(x, \dot{x})$ is a function of system coordinates; $y^{ref}(x, \dot{x})$ is a function of the desired system trajectory. The disturbance compensation module is used to estimate the lumped input disturbance rather than the original disturbances. The lumped input disturbance is defined as the projections of the original disturbances into the range space of the control distribution matrix. Such kind of treatment allows the compensation of original disturbances to be achieved through subtracting the estimated lumped input disturbance from system input [97].

4.2.1 Formulation of Tracking Problem

Express the dynamic equation of HFRR as:

$$M\ddot{x} = K_s \cdot i - C \cdot \dot{x} - k \cdot x - F_f \tag{4.2.1}$$

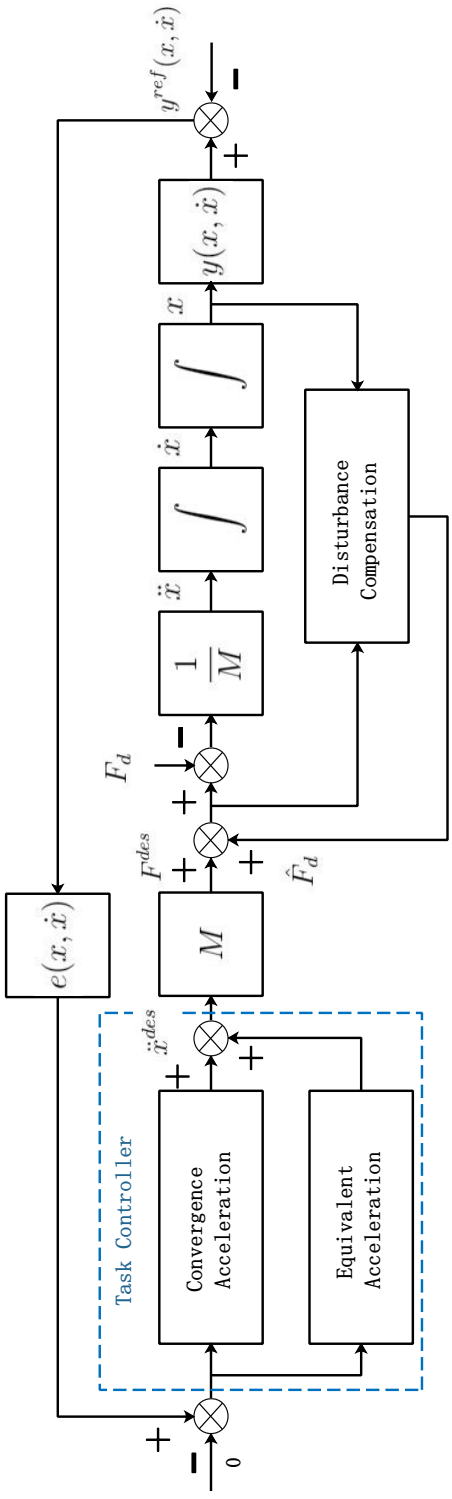

Figure 4.1: Block diagram of acceleration based control applied to mechanical system

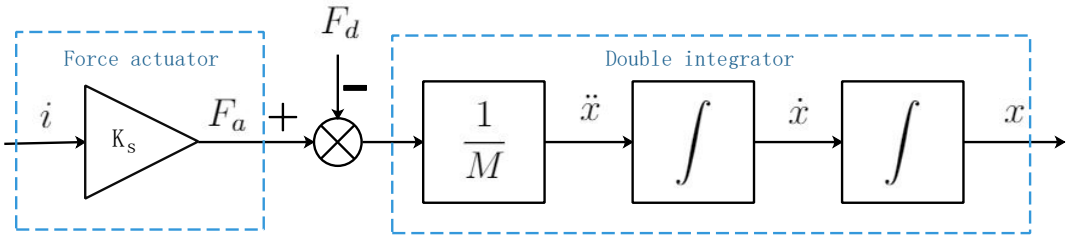

Figure 4.2: HFRR as a double integrator with virtual force actuator

where M is the mass of the moving component; K_s is motor constant; C is damping coefficient; k is spring factor; F_f is the friction exerts on motor shaft; x is the position of motor shaft; $\dot{x}$ is the velocity of motor shaft; $\ddot{x}$ is the acceleration of motor shaft and i is the current flow through motor coil. Let $F_a = K_s \cdot i$ represent the force exerted by VCM. Hence, the dynamic equation of HFRR is expressed as:

$$M\ddot{x} = F_a - F_d \tag{4.2.2}$$

where F_d is the lumped input disturbance defined by:

$$F_d = C \cdot \dot{x} + k \cdot x + F_f \tag{4.2.3}$$

Here $C \cdot \dot{x} + k \cdot x$ is introduced as an extended disturbance that has the dimension of force [96]. The value of it can be estimated through a reduced order disturbance observer, which will be discussed later. At this stage, we assume that perfect knowledge of the lumped input disturbance is available.

Now the dynamics of HFRR can be modelled as a double integrator, which is driven by a virtual force actuator F_a as shown in Fig.4.2. The lumped input disturbance F_d changes the system motion in the same way as that of the virtual force actuator. The force actuator which is VCM, in this case, applies the current feedback loop to regulate the output force as shown in Fig.4.3 [96]. In general, the tracking problem within the framework of acceleration control can be viewed as minimising the error between output and reference by imposing the desired acceleration through the force actuator.

Let the output of the plant y be a linear function of position and velocity. Then, the reference output can be expressed as $y^{ref}(x, \dot{x})$. Hence, the tracking error is

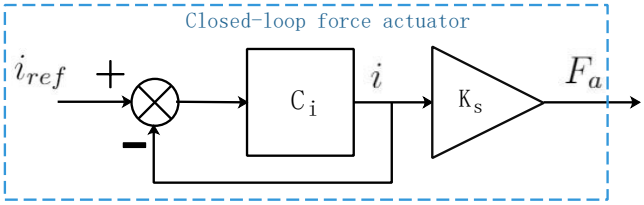

Figure 4.3: VCM as a closed-loop force actuator

$e(x, \dot{x}) = y(x, \dot{x}) - y^{ref}(x, \dot{x})$. In equilibrium, the system state is constrained to the manifold:

$$S(x, \dot{x}) = \left\{x, \dot{x} : e(x, \dot{x}) = y(x, \dot{x}) - y^{ref}(x, \dot{x}) = 0\right\} \tag{4.2.4}$$

The dynamics of the error is

$$\dot{e}(x, \dot{x}) = c_1\dot{x} + c_2\ddot{x} - \dot{y}^{ref}(x, \dot{x}) \tag{4.2.5}$$

where

$$c_1 = \frac{\partial y(x, \dot{x})}{\partial x} \neq 0 \tag{4.2.6}$$

$$c_2 = \frac{\partial y(x, \dot{x})}{\partial \dot{x}} \neq 0 \tag{4.2.7}$$

The selection of acceleration should enforce convergence to and stability of the equilibrium. As the nominal plant system is a linear time-invariant system, superposition principle can be applied in the design of the acceleration controller. Therefore, the resultant acceleration can be decomposed into two components:

- The first component can be selected to enforce equilibrium solution for initial conditions consistent with equilibrium $e|_{t=0} = 0$.
- The second component can be selected to enforce convergence to equilibrium if initial condition is not consistent with equilibrium $e|_{t=0} \neq 0$.

As mentioned above, the resultant acceleration of HFRR should be enforced by VCM as the virtual force actuator.

4.2.2 Force Control Design

The equivalent acceleration $\ddot{x}^{eq}$ or corresponding equivalent force F^{eq} as first component can be derived by solving:

$$\dot{e}(x, \dot{x}) = c_1\dot{x} + c_2\ddot{x}^{eq} - \dot{y}^{ref}(x, \dot{x}) = 0 \tag{4.2.8}$$

Hence,

$$\ddot{x}^{eq} = -\frac{c_1\dot{x} - \dot{y}^{ref}(x, \dot{x})}{c_2} \tag{4.2.9}$$

The equivalent acceleration obtained from the equation above will enforce a motion that is equidistant from the equilibrium solution as $\dot{e}(x, \dot{x}) = 0 \Rightarrow e(x, \dot{x}) = \text{ const }$ [97]. In theory, we can enforce the motion to equilibrium solution by letting $e(x, \dot{x}, \ddot{x}) = 0$. However, we decide to only take position and velocity error in consideration as the acceleration information is unavailable on HFRR. The equivalent force to enforce such equivalent acceleration is:

$$F^{eq} = F_d + M\ddot{x}^{eq} \tag{4.2.10}$$

$$= C \cdot \dot{x} + k \cdot x + F_f - M \cdot \frac{c_1\dot{x} - \dot{y}^{ref}(x, \dot{x})}{c_2} \tag{4.2.11}$$

By substituting equation (4.2.9) into equation (4.2.5), one can obtain:

$$\dot{e}(x, \dot{x}) = c_2(\ddot{x} - \ddot{x}^{eq}) \tag{4.2.12}$$

As it pointed out above, the selection of output function with respect to position and velocity will lead to an equivalent force that only enforce equilibrium solution for initial conditions consistent with equilibrium $e|_{t=0} = 0$. To achieve the requirement of tracking where the error between output and reference should be zero, additional terms need to be added to system input to enforce convergence if initial condition is not consistent with equilibrium $e|_{t=0} \neq 0$. Let the desired rate of change of the distance from manifold $S(x, \dot{x}) = 0$ as:

$$\dot{e}(x, \dot{x}) = \dot{e}^{des}(x, \dot{x}) \tag{4.2.13}$$

Therefore, the desired acceleration corresponding to the desired rate of change of the distance is:

$$\ddot{x}^{des} = \ddot{x}^{eq} + \ddot{x}^{con} \tag{4.2.14}$$

where $\ddot{x}^{con}$ is the convergence acceleration defined by:

$$\ddot{x}^{con} = \frac{\dot{e}^{des}(x, \dot{x})}{c_2} \tag{4.2.15}$$

The desired control force to enforce the desired acceleration should be:

$$F^{des} = F^{eq} + F^{con} \tag{4.2.16}$$

$$= F_d + M\ddot{x}^{eq} + M\ddot{x}^{con} \tag{4.2.17}$$

$$= C \cdot \dot{x} + k \cdot x + F_f - M \cdot \frac{c_1\dot{x} - \dot{y}^{ref}(x, \dot{x})}{c_2} + M \cdot \frac{\dot{e}^{des}(x, \dot{x})}{c_2} \tag{4.2.18}$$

Comment on (4.2.18): the lumped input disturbance F_d including friction in equation (4.2.18) is unavailable and should be estimated in the synthesis of the desired control force. The estimation of the lumped input disturbance will be discussed in section 4.3. At this point, we assume perfect knowledge of F_d.

4.2.3 Convergence Law Design

To enforce convergence and stability of the system, the rate of change of the output error $e(x, \dot{x})$ should be carefully designed. Given a Lyapunov function candidate with respect to output error as:

$$V = \frac{e^2(x, \dot{x})}{2} > 0, \quad V(0) = 0 \tag{4.2.19}$$

Taking the derivative of the Lyapunov function, we have:

$$\dot{V} = e(x, \dot{x})\dot{e}(x, \dot{x}) \tag{4.2.20}$$

$$= e(x, \dot{x})c_2 \left(\ddot{x} - \ddot{x}^{eq}\right) \tag{4.2.21}$$

$$= e(x, \dot{x})\frac{c_2}{M}\left(F - F^{eq}\right) \tag{4.2.22}$$

To satisfy Lyapunov stability conditions, the derivative of the Lyapunov function should be negative definite. Therefore, we let:

$$\dot{V} \leq -\lambda(V) \tag{4.2.23}$$

where $\lambda(V) > 0$ is a positive scalar function of Lyapunov function. We can enforce different types of convergence of the Lypapunov function by selecting appropriate

scalar function $\lambda(V)$. Hence,

$$e(x,\dot{x})\dot{e}(x,\dot{x}) + \lambda(V) \leq 0 \tag{4.2.24}$$

$$e(x,\dot{x})c_2(\ddot{x} - \ddot{x}^{eq}) + \lambda(V) \leq 0 \tag{4.2.25}$$

Therefore, the conditions for acceleration and force to satisfy asymptotic convergence of the system should be:

$$\ddot{x} \leq \ddot{x}^{eq} - \frac{1}{c_2} \cdot \frac{\lambda(V)}{e(x,\dot{x})} \tag{4.2.26}$$

and

$$F \leq F^{eq} - \frac{M}{c_2} \cdot \frac{\lambda(V)}{e(x,\dot{x})} \tag{4.2.27}$$

To simplify analysis, considering the case where $\dot{V} = -\lambda(V)$. The acceleration and input force can be expressed as:

$$\ddot{x} = \ddot{x}^{eq} - \frac{1}{c_2}\frac{\lambda(V)}{|e(x,\dot{x})|}\,\mathrm{sign}[e(x,\dot{x})] = \ddot{x}^{eq} + \ddot{x}^{con}, \quad e(x,\dot{x}) \neq 0 \tag{4.2.28}$$

$$F = F^{eq} - \frac{M}{c_2}\frac{\lambda(V)}{|e(x,\dot{x})|}\,\mathrm{sign}[e(x,\dot{x})] = F^{eq} + F^{con}, \quad e(x,\dot{x}) \neq 0 \tag{4.2.29}$$

where

$$\mathrm{sign}[e(x,\dot{x})] = \begin{cases} +1 & \text{if} \quad [e(x,\dot{x})] > 0 \\ -1 & \text{if} \quad [e(x,\dot{x})] < 0 \end{cases} \tag{4.2.30}$$

Comment on equation (4.2.28) and equation (4.2.29): It should be noted that once the trajectory of the system arrives at the equilibrium, the convergence control action should be eliminated, that is:

$$\ddot{x} = \ddot{x}^{eq}, \quad e(x,\dot{x}) = 0 \tag{4.2.31}$$

$$F = F^{eq}, \quad e(x,\dot{x}) = 0 \tag{4.2.32}$$

The selection of $\lambda(V)$ should satisfy that:

- The control input defined by $\lambda(V)$ should be bounded.
- When the equilibrium has been reached, both equivalent force and convergence force should become zero

Select the structure of $\lambda(V)$ as:

$$\lambda(V) = -K_\lambda 2^\alpha V^\alpha \tag{4.2.33}$$

where

$$K_\lambda > 0, \quad \frac{1}{2} \leq \alpha \leq 1 \tag{4.2.34}$$

For $\alpha = 1$, the exponential convergence is achieved. The finite-time convergence is achieved for $\frac{1}{2} \leq \alpha < 1$. The fastest finite-time convergence is achieved for $\alpha = \frac{1}{2}$. To be specific, the desired acceleration corresponding to exponential convergence is:

$$\ddot{x}_e^{des} = \ddot{x}^{eq} + \ddot{x}_e^{con} = \ddot{x}^{eq} - \frac{K_\lambda}{c_2} e(x, \dot{x}) \tag{4.2.35}$$

where $\ddot{x}_e^{con}$ represents the convergence acceleration in this case. The force that enforce the desired acceleration corresponding to exponential convergence is:

$$F = C \cdot \dot{x} + k \cdot x + F_f - M \cdot \frac{c_1 \dot{x} - \dot{y}^{ref}(x, \dot{x})}{c_2} - M \frac{K_\lambda}{c_2} e(x, \dot{x}) \tag{4.2.36}$$

The dynamics of $e(x, \dot{x})$ in this case is governed by:

$$e(t) = e(t_0)^{-K_\lambda t} \tag{4.2.37}$$

where $e(t_0)$ denotes the initial output error at t_0. In theory, the convergence time is infinite for exponentially decaying output error. However, as a rule of thumb, it can be approximated as:

$$t_{re} = \frac{5}{K_\lambda} \tag{4.2.38}$$

In addition, the desired acceleration corresponding to finite-time convergence is:

$$\ddot{x}_f^{des} = \ddot{x}^{eq} + \ddot{x}_f^{con} = \ddot{x}^{eq} - \frac{K_\lambda}{c_2} |e(x, \dot{x})|^{2\alpha - 1} \operatorname{sign}[e(x, \dot{x})] \tag{4.2.39}$$

The force that enforce the desired acceleration corresponding to finite-time convergence is:

$$F = C \cdot \dot{x} + k \cdot x + F_f - M \cdot \frac{c_1 \dot{x} - \dot{y}^{ref}(x, \dot{x})}{c_2} - M \frac{K_\lambda}{c_2} |e(x, \dot{x})|^{2\alpha - 1} \operatorname{sign}[e(x, \dot{x})] \tag{4.2.40}$$

The convergence time for finite-time convergence is determined by:

$$t_{rf} = \left[e^2(t_0)\right]^{1-\alpha} \frac{1}{2K_\lambda(1-\alpha)} \tag{4.2.41}$$

For $\alpha = \frac{1}{2}$, the desired acceleration and force take specific forms as follows:

$$\ddot{x}_f^{des} = \ddot{x}^{eq} - \frac{K_\lambda}{c_2}\,\mathrm{sign}[e(x,\dot{x})] \tag{4.2.42}$$

$$F = C\cdot\dot{x} + k\cdot x + F_f - M\frac{K_\lambda}{c_2}\,\mathrm{sign}[e(x,\dot{x})] \tag{4.2.43}$$

When implementing control corresponding to $\alpha = \frac{1}{2}$, discontinuous force input to the system in may excite unmodeled dynamics of the system. To mitigate the undesirable effect, the amplitude of the discontinuous term can be modified to make it variable around equilibrium as follows:

$$\ddot{x}_f^{con} = -\frac{K_\lambda}{c_2}|e(x,\dot{x})|^\beta\,\mathrm{sign}[e(x,\dot{x})] \tag{4.2.44}$$

where

$$0 < \beta < 1 \tag{4.2.45}$$

In this study, the convergence law is selected as finite-time convergence as we want the output of the system to track a sinusoidal reference with relatively high frequency. This is done to avoid significant phase lag between the output of the system and the reference.

4.3 Time Domain Disturbance Observer

As it has been pointed out, the lumped input disturbance should be estimated to construct equivalent control. That is where the disturbance observer comes in. Similar to traditional state observer, a disturbance observer should be designed based on some known properties of the model of disturbance [53] [98]. Usually, the disturbance is modelled by a polynomial of time. For a disturbance corresponding to $(m-1)$ order polynomial, it can be expressed as:

$$\begin{bmatrix} \dot{\vartheta} \\ \cdots \\ \dot{\vartheta}_{m-1} \end{bmatrix} = \begin{bmatrix} 0 & 1 & 0 \\ \cdots & \cdots & \cdots \\ 0 & 0 & 0 \end{bmatrix} \begin{bmatrix} \vartheta \\ \cdots \\ \vartheta_{m-1} \end{bmatrix} \tag{4.3.1}$$

$$F_{dm} = \begin{bmatrix} 1 & \cdots & 0 \end{bmatrix} \begin{bmatrix} \vartheta \\ \cdots \\ \vartheta_{m-1} \end{bmatrix} \tag{4.3.2}$$

where ϑ_x represents the x-th state of the disturbance state space model; F_{dm} represents the output of the disturbance state space model of $(m-1)$ order. Assume the lumped input disturbance changes slowly relative to the state variables of the plant. The disturbance can then be modelled as a constant:

$$F_{d0} = -M\vartheta \tag{4.3.3}$$

where F_{d0} represents the disturbance; M is the total mass of the moving components on HFRR; ϑ is the internal state of the disturbance state space model with its first derivative equals to zero:

$$\dot{\vartheta} = 0 \tag{4.3.4}$$

By introducing the state ϑ to the system, the augmented plant-disturbance system can be written as [96]:

$$\begin{bmatrix} \dot{x} \\ \dot{v} \\ \dot{\vartheta} \end{bmatrix} = \begin{bmatrix} 0 & 1 & 0 \\ 0 & 0 & -M^{-1} \\ 0 & 0 & 0 \end{bmatrix} \begin{bmatrix} x \\ v \\ \vartheta \end{bmatrix} + \begin{bmatrix} 0 \\ M^{-1} \\ 0 \end{bmatrix} F_a \tag{4.3.5}$$

where F_a is the control force applied to the system input. Both states of the plant and the state of disturbance model can be estimated simultaneously using a full-order Luenberger observer. However, as the position signal x can be perfectly acquired from incremental encoder, a reduced order observer is constructed in this case [99] [100]. The augmented plant-disturbance system can be rewritten as:

$$\begin{bmatrix} \dot{x}_a \\ \dot{\mathbf{x}}_b \end{bmatrix} = \begin{bmatrix} \mathbf{A}_{aa} & \mathbf{A}_{ab} \\ \mathbf{A}_{ba} & \mathbf{A}_{bb} \end{bmatrix} \begin{bmatrix} x_a \\ \mathbf{x}_b \end{bmatrix} + \begin{bmatrix} \mathbf{B}_a \\ \mathbf{B}_b \end{bmatrix} \mathbf{u} \tag{4.3.6}$$

where

$$x_a = x \tag{4.3.7}$$

$$\mathbf{x}_b = \begin{bmatrix} v \\ \vartheta \end{bmatrix} \tag{4.3.8}$$

and

$$\mathbf{A}_{aa} = 0 \tag{4.3.9}$$

$$\mathbf{A}_{ab} = \begin{bmatrix} 1 & 0 \end{bmatrix} \tag{4.3.10}$$

$$\mathbf{A}_{ba} = \begin{bmatrix} 0 \\ 0 \end{bmatrix} \tag{4.3.11}$$

$$\mathbf{A}_{bb} = \begin{bmatrix} 0 & -M^{-1} \\ 0 & 0 \end{bmatrix} \tag{4.3.12}$$

In this way, the measurable state variable x, unmeasurable state variables v and ϑ can be treated separately for the purpose of order reduction of the observer. Represent the system as:

$$\begin{aligned} \dot{\mathbf{x}}_b &= \mathbf{A}_{bb}\mathbf{x}_b + (\mathbf{A}_{ba}x_a + \mathbf{B}_b\mathbf{u}) \\ \dot{x}_a - A_{aa}x_a - \mathbf{B}_a\mathbf{u} &= \mathbf{A}_{ab}\mathbf{x}_b \end{aligned} \tag{4.3.13}$$

where $\mathbf{x}_b$ is the states vector for the modified system; $\mathbf{A}_{bb}$ is the dynamics matrix for the modified system; $\mathbf{A}_{ba}x_a + \mathbf{B}_b\mathbf{u}$ is the modified system input; $\mathbf{A}_{ab}$ is the measurement matrix for the modified system; $\dot{x}_a - A_{aa}x_a - \mathbf{B}_a\mathbf{u}$ is the modified system output. Therefore, the unmeasured states vector $\mathbf{x}_b$ can be obtained by applying Luenberger-style observer to the modified system:

$$\dot{\hat{\mathbf{x}}}_b = (\mathbf{A}_{bb} - \mathbf{L}\mathbf{A}_{ab})\,\hat{\mathbf{x}}_b + \mathbf{A}_{ba}x_a + \mathbf{B}_b\mathbf{u} + \mathbf{L}\,(\dot{x}_a - A_{aa}x_a - \mathbf{B}_a\mathbf{u}) \tag{4.3.14}$$

where

$$\mathbf{L} = \begin{bmatrix} l_1 \\ l_2 \end{bmatrix} \tag{4.3.15}$$

$\hat{\mathbf{x}}_b$ is the estimated $\mathbf{x}_b$ given by the observer; $\mathbf{L}$ is the gain vector for the driving feedback component of the observer. To avoid introduction of noise due to signal differentiation in the above equation, we firstly put differential terms on the left of the equation and rewrite the equation as:

$$\dot{\hat{\mathrm{x}}}_b - \mathbf{L}\dot{y} = (\mathbf{A}_{bb} - \mathbf{L}\mathbf{A}_{ab})\,(\hat{\mathbf{x}}_b - \mathbf{L}y) + [(\mathbf{A}_{bb} - \mathbf{L}\mathbf{A}_{ab})\,\mathbf{L} + \mathrm{A}_{ba} - \mathbf{L}\mathbf{A}_{\mathbf{aa}}]\,y + (\mathbf{B}_b - \mathbf{L}\mathbf{B}_a)\,\mathbf{u} \tag{4.3.16}$$

where

$$y = x_a \tag{4.3.17}$$

Then, we can define an intermediate vector $\mathbf{z}$ to eliminate the need for $\dot{y}$:

$$\mathbf{z} = \begin{bmatrix} z_1 \\ z_2 \end{bmatrix} = \begin{bmatrix} v \\ \vartheta \end{bmatrix} = \hat{\mathbf{x}}_b - \mathbf{L}y \tag{4.3.18}$$

The reduced order observer can be obtained as:

$$\begin{aligned} \dot{\hat{z}}_1 &= -l_1 \left(\hat{z}_2 + l_2 x\right) \\ \dot{\hat{z}}_2 &= \hat{z}_1 - l_2 \hat{z}_2 + \left(l_1 - l_2^2\right) x + F^* \end{aligned} \tag{4.3.19}$$

where

$$F^* = M^{-1} F_a \tag{4.3.20}$$

The dynamics of the observer in s domain are:

$$\hat{F}_d(s) = \frac{l_1}{s^2 + l_2 s + l_1} F_d(s) \tag{4.3.21}$$

$$\hat{v}(s) = \frac{l_1}{s^2 + l_2 s + l_1} v(s) \tag{4.3.22}$$

Two poles of the observer p_{o1} and p_{o2} can be arbitrarily allocated in the complex plane. They satisfy the following equations:

$$l_1 = p_{o1} \cdot p_{o2} \tag{4.3.23}$$

$$l_2 = -(p_{o1} + p_{o2}) \tag{4.3.24}$$

The equations of the dynamics of the observer show that the estimated disturbance can be regarded as the actual disturbance that passing through a low-pass filter. We represent the dynamics of the low-pass filter as $Q(s)$. Then, the dynamics of the estimation error of disturbance should be a function with respect to $Q(s)$ and the actual disturbance $F_d(s)$, which can be expressed as:

$$E_{F_d}(s) = F_d(s) - \hat{F}_d(s) = \left[1 - Q(s)\right] F_d(s) \tag{4.3.25}$$

where $E_{F_d}(s)$ is the error of the estimation of disturbance in s domain. By allocating the poles properly, the estimated disturbance within the frequency band of interest

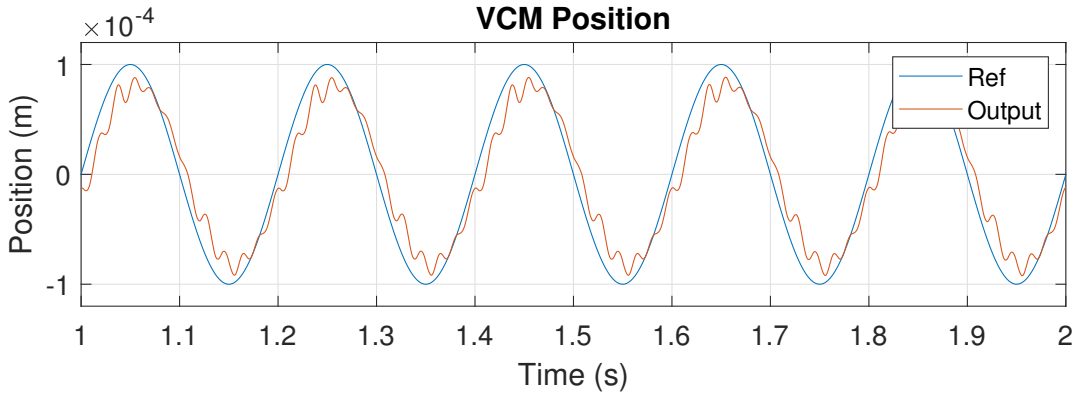

Figure 4.4: Simulated VCM position tracking using PI control

can approach to its actual value. The output of the plant considering disturbance observer in s domain can be expressed as:

$$X(s) = G_{nd}(s) \cdot F^{des}(s) + G_{nd}(s) \cdot E_{F_d}(s) \tag{4.3.26}$$

where $G_{nd}(s)$ denotes the nominal plant in s domain:

$$G_{nd}(s) = \frac{1}{M} \cdot \frac{1}{s^2} \tag{4.3.27}$$

The detailed analysis can be referred to [101] [102].

4.4 Simulations

In simulation, the reference position signal is a sinusoidal wave of the frequency of $5Hz$. The amplitude is set as $100\mu m$. Fig. 4.4 shows the output of VCM in terms of shaft position using PI control. Fig.4.5 shows the error of position tracking in this case. It can be found that due to the effect of frictional load, the output position signal lags the reference and the shape of it is distorted as well. The error of position contains significant harmonics. Fig.4.6 shows the position tracking of VCM using acceleration based control. It can be found that perfect tracking can be achieved without significant lagging. Fig.4.7 shows the error of position tracking in this case. The tracking accuracy of acceleration control outperforms that of PI control shown in Fig.4.5.

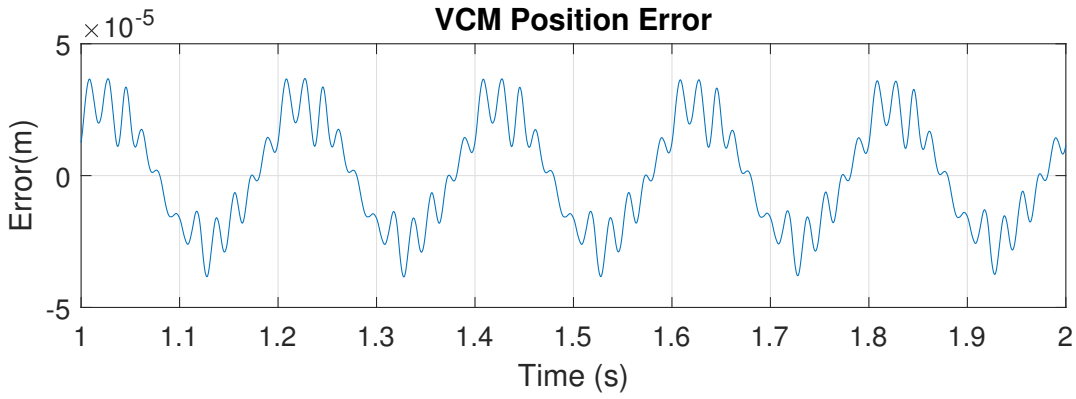

Figure 4.5: Simulated VCM position tracking error using PI control

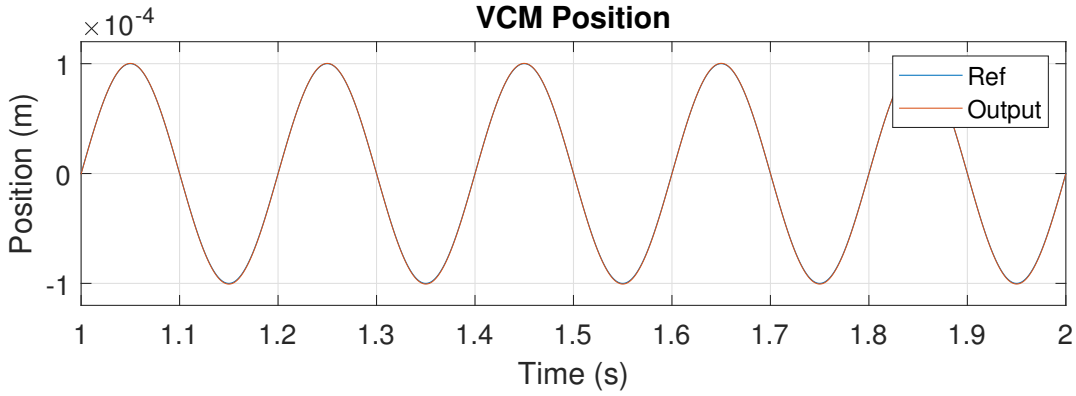

Figure 4.6: Simulated VCM position tracking using acceleration based control

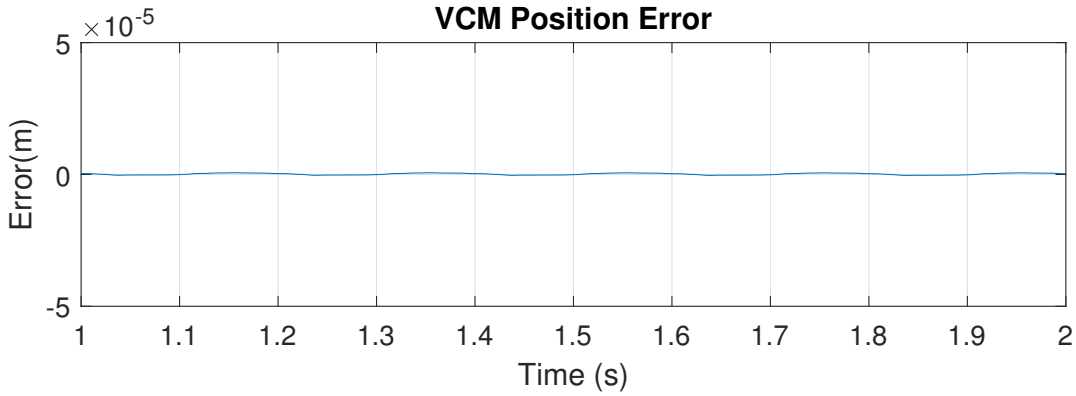

Figure 4.7: Simulated VCM position tracking error using acceleration based control

Frequency(Hz)	Amplitude(μm)	Normal Force (N)	Control Method
3Hz	120μm	6N	PI Control
3Hz	120μm	6N	AB Control
5Hz	120μm	6N	PI Control
5Hz	120μm	6N	AB Control
7Hz	120μm	6N	PI Control
7Hz	120μm	6N	AB Control
3Hz	120μm	10N	PI Control
3Hz	120μm	10N	AB Control
5Hz	120μm	10N	PI Control
5Hz	120μm	10N	AB Control
7Hz	120μm	10N	PI Control
7Hz	120μm	10N	AB Control

Table 4.1: Experimental conditions for comparisons between PI control and acceleration based control (AB Control is short for acceleration based control)

4.5 Experiment Results

To simplify the experiments, the types of specimen are same in each test. The settings of remaining experimental conditions applied in experiments are shown in Table. 4.1.

In Table 4.1, there are 12 sets of experimental conditions. The frequency varies from $3Hz$ to $7Hz$. The normal varies from $6N$ to $10N$. The specimens in all experiments are chosen as aluminium plate with petroleum ether (Al&PE) covered on top of them. To make sure the initial conditions such as surface roughness are same in each experiment, both aluminium plate and petroleum ether between contacting surfaces should be replaced at the end of each test. To assess the performance of the proposed control method, comparisons between conventional PI control and acceleration based control have been done.

Fig.4.8 and Fig.4.9 are the experimental results obtained using PI control to track

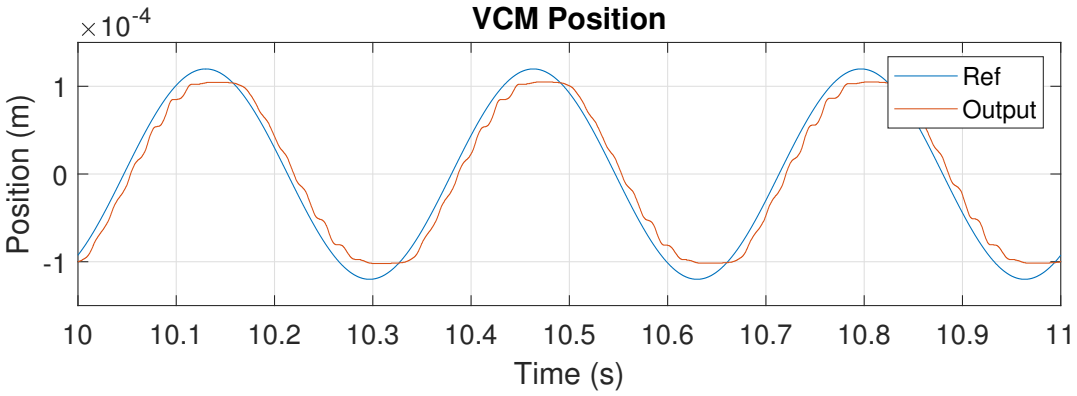

Figure 4.8: Experimental result of position reference tracking of VCM using PI control with reference at $3Hz$ and normal force of $6N$

a sinusoidal wave of the frequency of $3Hz$. The normal force in this case is set as $6N$. The desired amplitude in this case is set as $120\mu m$. It can be found that the output position of VCM is distorted due to disturbance. Fig.4.10 and Fig.4.11 are the experimental results obtained using acceleration based control with the same reference as for PI control. Compared with the results obtained by PI control, the error of position tracking using acceleration based is suppressed significantly.The average relative error corresponding to the data shown in Fig.4.11 is calculated as 4.59%. In addition, Fig.4.12 shows the estimated lumped input disturbance given by the reduced order disturbance observer in experiment. The fundamental period of disturbance is the same as that of the reference position signal, which is in agreement with the results of simulation.

Fig.4.13 and Fig.4.14 are the experimental results obtained using PI control to track a sinusoidal wave of the frequency of $5Hz$. The normal force in this case is set as $6N$. The desired amplitude in this case is set as $120\mu m$. Fig.4.15 and Fig.4.16 are the experimental results obtained using acceleration based control with the same reference as for PI control. Compared with the results obtained by PI control, the error of position tracking using acceleration based is suppressed as well. In addition, Fig.4.17 shows the estimated lumped input disturbance given by the reduced order disturbance observer in experiment.

Fig.4.18 and Fig.4.19 are the experimental results obtained using PI control to

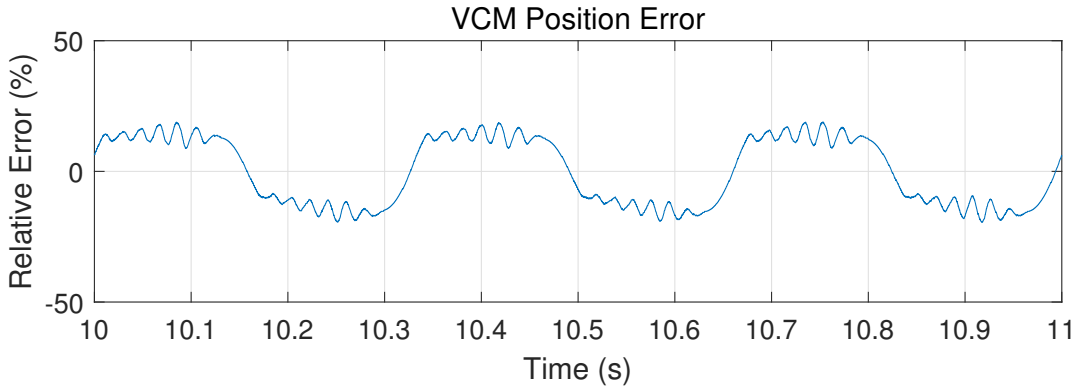

Figure 4.9: Experimental error of position reference tracking of VCM using PI control with reference at $3Hz$ and normal force of $6N$

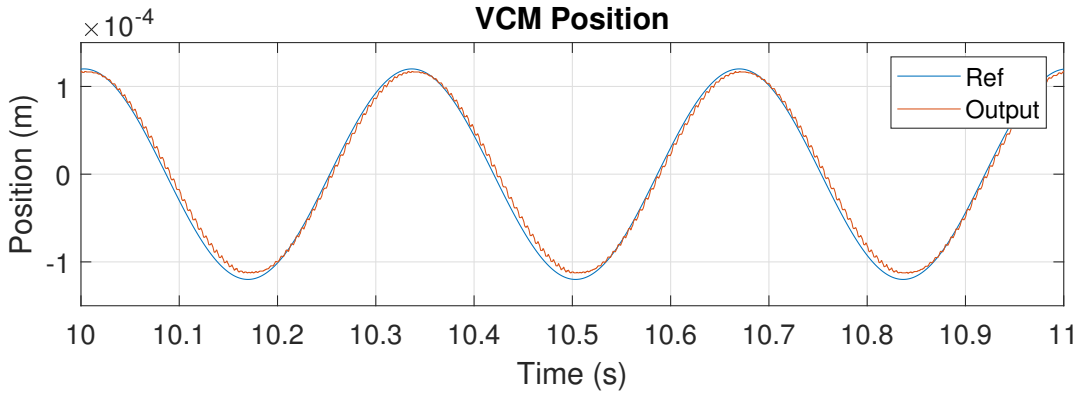

Figure 4.10: Experimental result of position reference tracking of VCM using acceleration based control with reference at $3Hz$ and normal force of $6N$

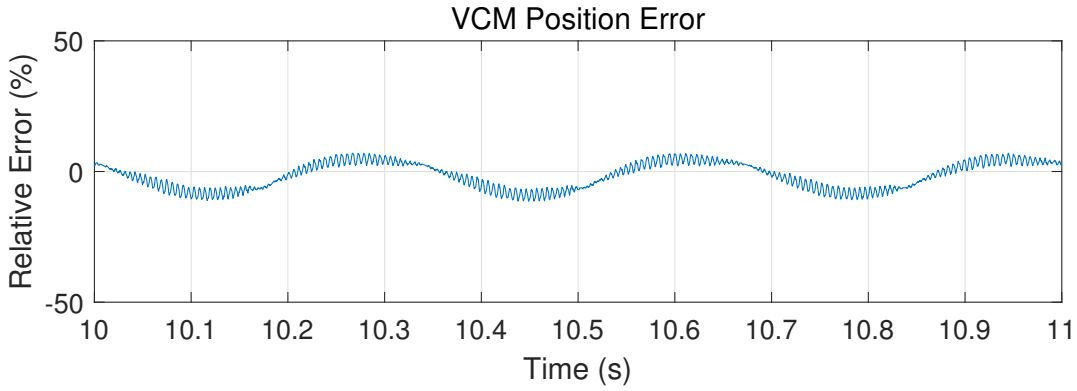

Figure 4.11: Experimental error of position reference tracking of VCM using acceleration based control with reference at $3Hz$ and normal force of $6N$

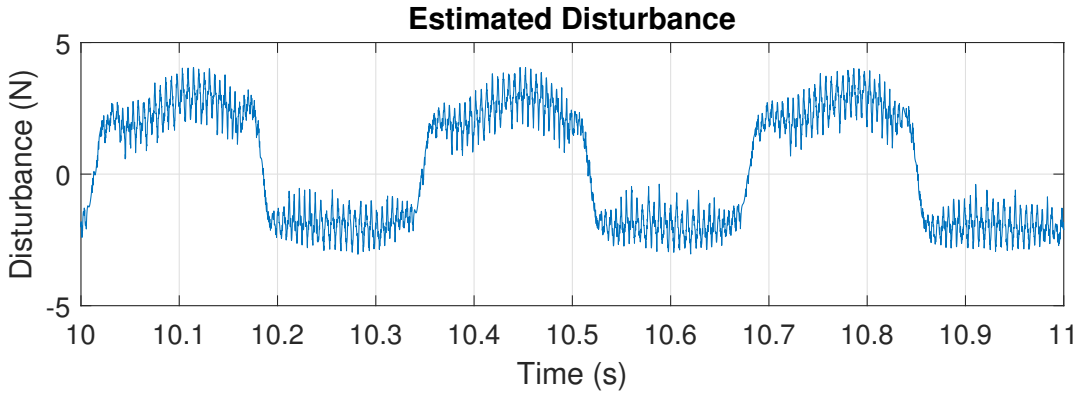

Figure 4.12: Estimated lumped input disturbance obtained using reduced order disturbance observer in position reference tracking experiment with reference at $3Hz$ and normal force of $6N$

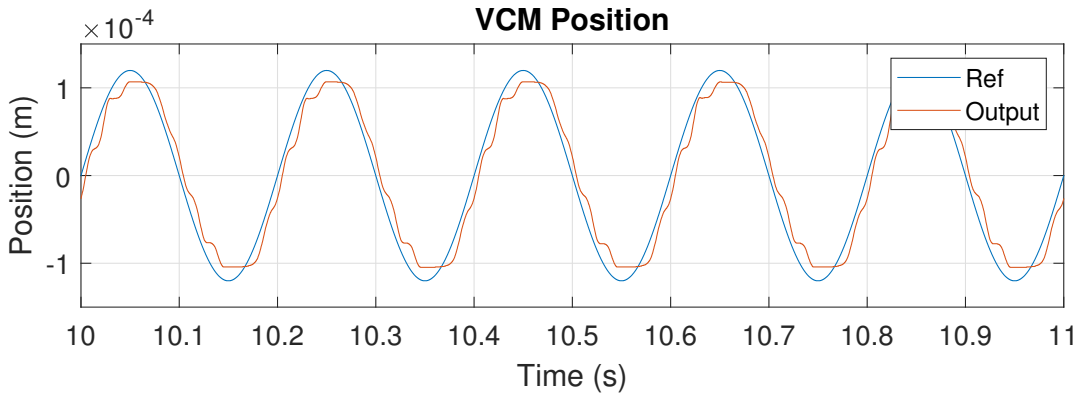

Figure 4.13: Experimental result of position reference tracking of VCM using PI control with reference at $5Hz$ and normal force of $6N$

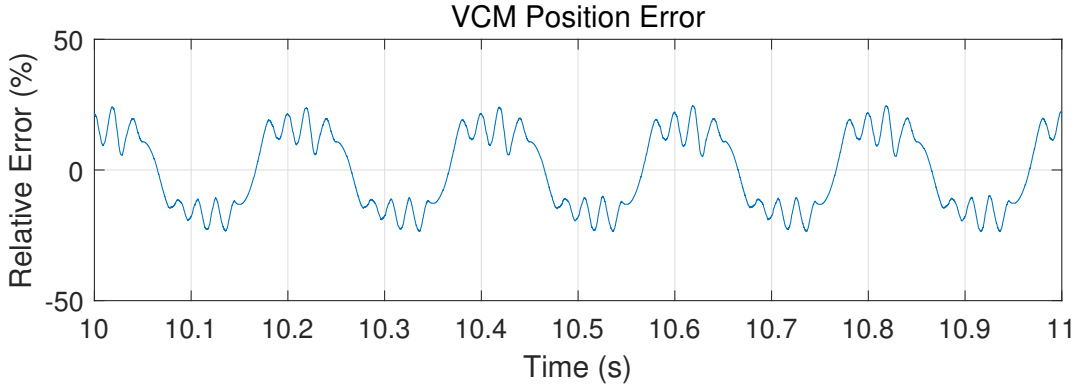

Figure 4.14: Experimental error of position reference tracking of VCM using PI control with reference at $5Hz$ and normal force of $6N$

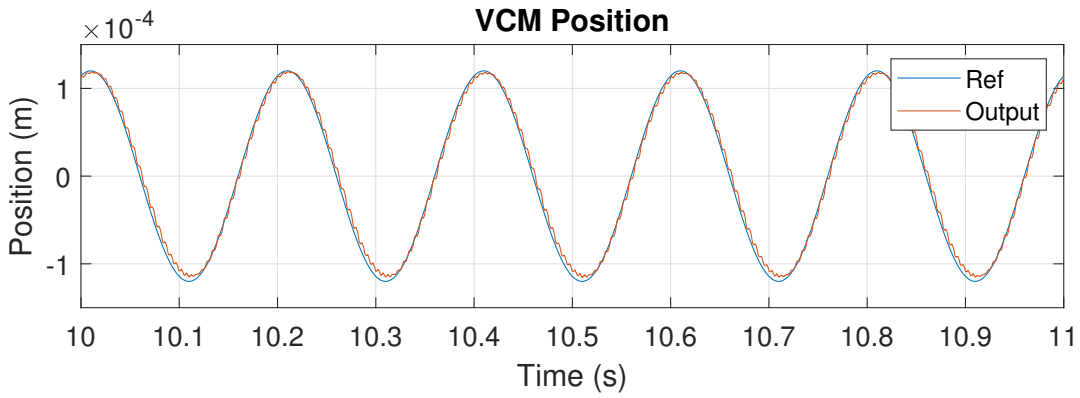

Figure 4.15: Experimental result of position reference tracking of VCM using acceleration based control with reference at $5Hz$ and normal force of $6N$

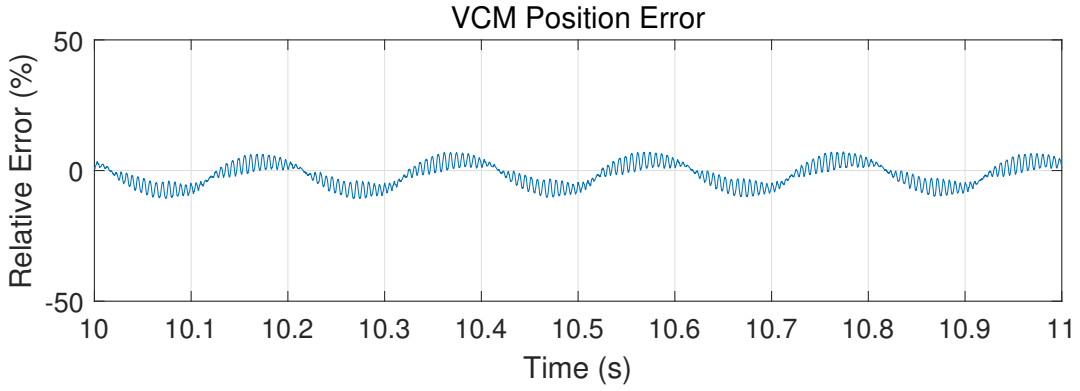

Figure 4.16: Experimental error of position reference tracking of VCM using acceleration based control with reference at $5Hz$ and normal force of $6N$

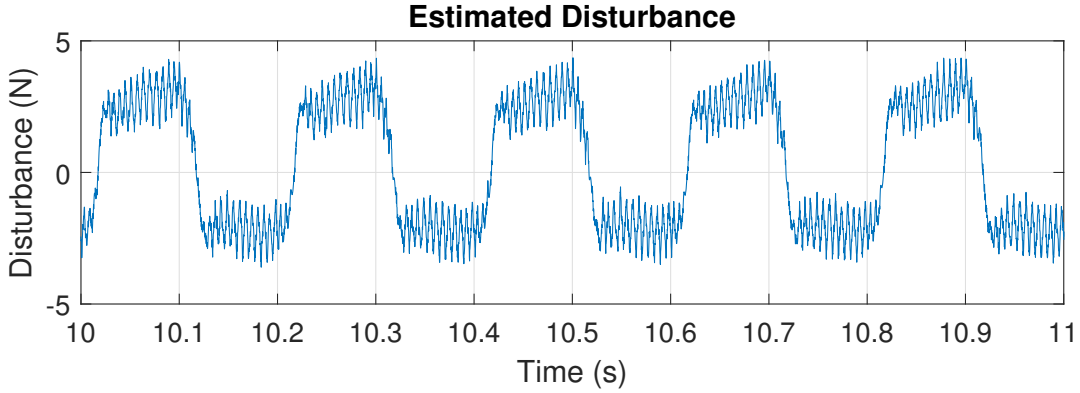

Figure 4.17: Estimated lumped input disturbance obtained using reduced order disturbance observer in position reference tracking experiment with reference at $5Hz$ and normal force of $6N$

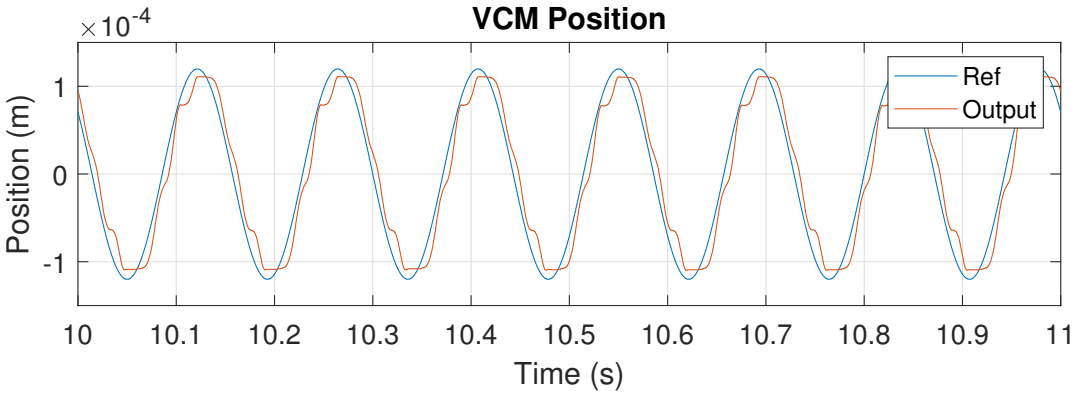

Figure 4.18: Experimental result of position reference tracking of VCM using PI control with reference at $7Hz$ and normal force of $6N$

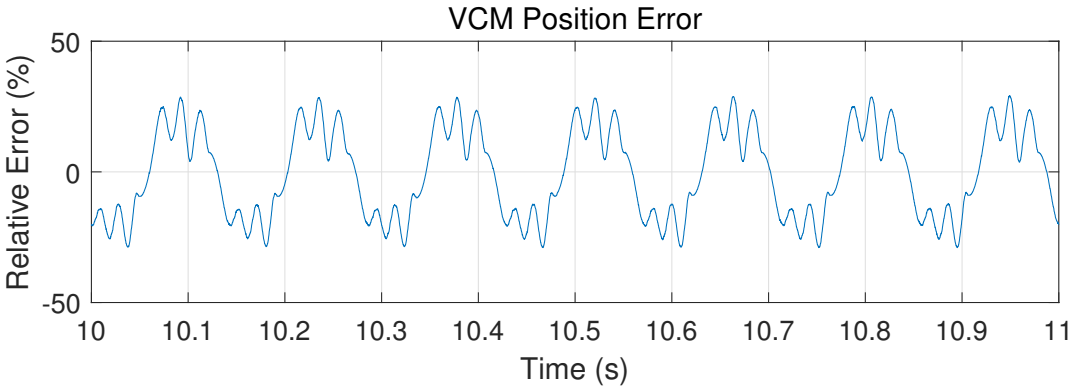

Figure 4.19: Experimental error of position reference tracking of VCM using PI control with reference at $7Hz$ and normal force of $6N$

track a sinusoidal wave of the frequency of $7Hz$. The normal force in this case is set as $6N$. The desired amplitude in this case is set as $120\mu m$. Fig.4.20 and Fig.4.21 are the experimental results obtained using acceleration based control with the same reference as for PI control. Compared with the results obtained by PI control, the error of position tracking using acceleration based is suppressed as well. In addition, Fig.4.22 shows the estimated lumped input disturbance given by the reduced order disturbance observer in experiment.

Fig.4.23 and Fig.4.24 are the experimental results obtained using PI control to track a sinusoidal wave of the frequency of $3Hz$. The normal force in this case is set as $10N$. the desired amplitude in this case is set as $120\mu m$. It can be found that

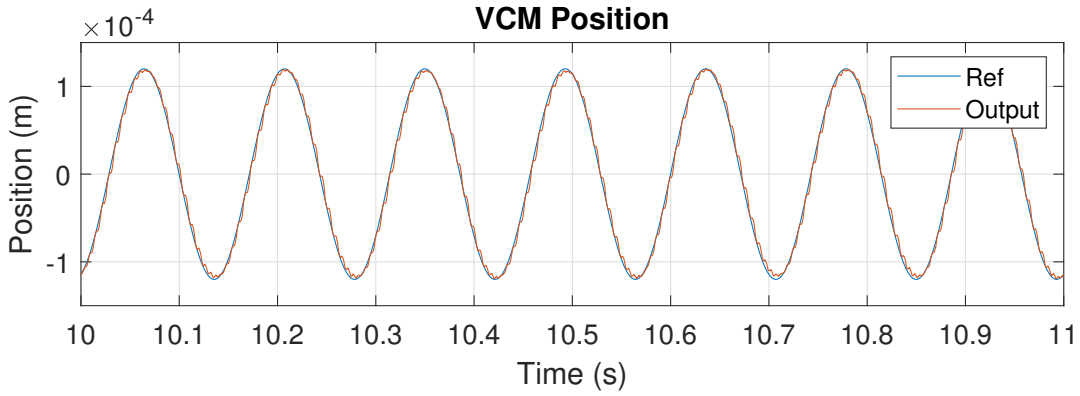

Figure 4.20: Experimental result of position reference tracking of VCM using acceleration based control with reference at $7Hz$ and normal force of $6N$

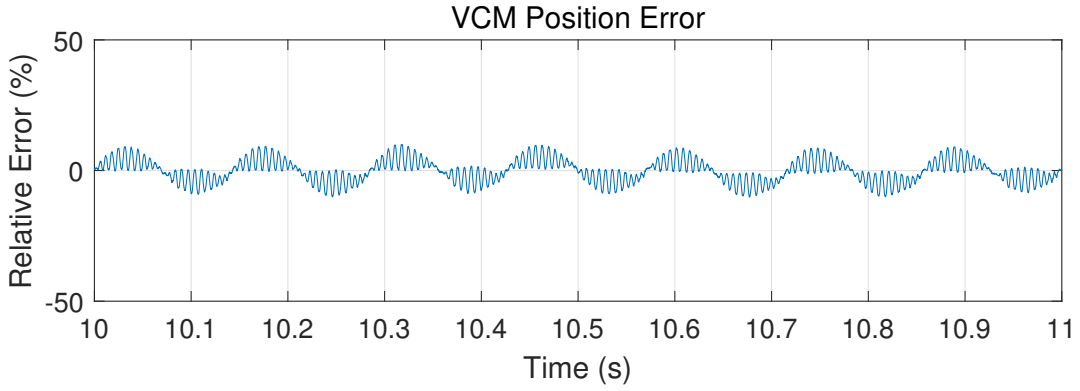

Figure 4.21: Experimental error of position reference tracking of VCM using acceleration based control with reference at $7Hz$ and normal force of $6N$

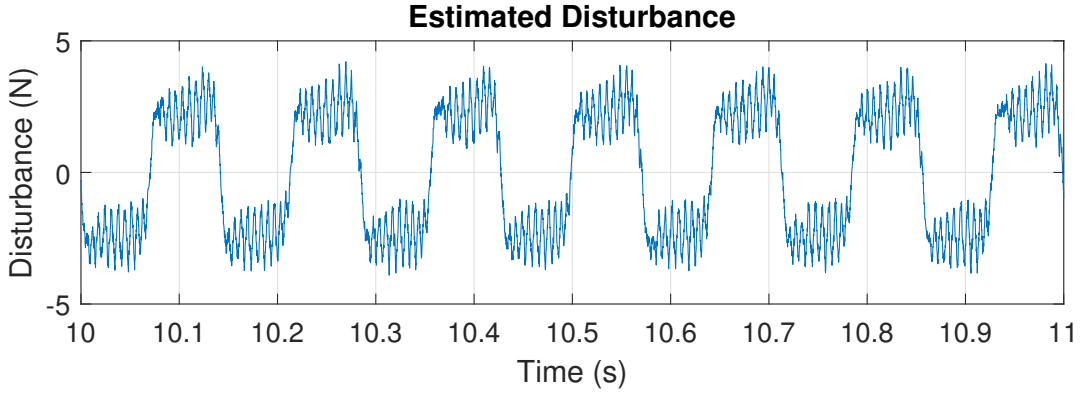

Figure 4.22: Estimated lumped input disturbance obtained using reduced order disturbance observer in position reference tracking experiment with reference at $7Hz$ and normal force of $6N$

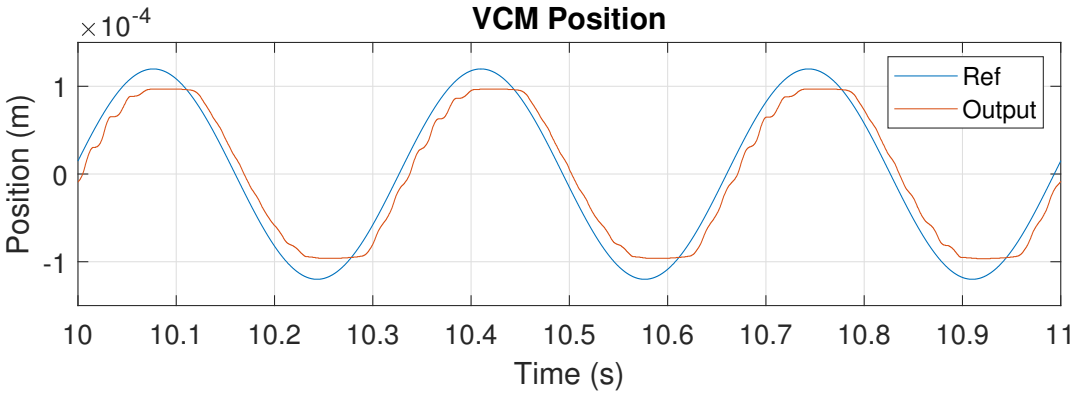

Figure 4.23: Experimental result of position reference tracking of VCM using PI control with reference at $3Hz$ and normal force of $10N$

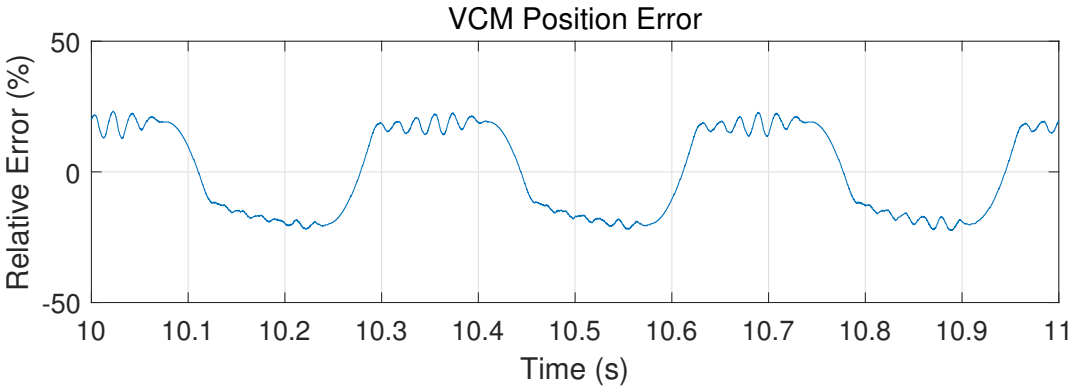

Figure 4.24: Experimental error of position reference tracking of VCM using PI control with reference at $3Hz$ and normal force of $10N$

the output position of VCM is distorted due to disturbance. Fig.4.25 and Fig.4.26 are the experimental results obtained using acceleration based control with the same reference as for PI control. Compared with the results obtained by PI control, the error of position tracking using acceleration based is suppressed significantly. In addition, Fig.4.27 shows the estimated lumped input disturbance given by the reduced order disturbance observer in experiment. The fundamental period of disturbance is the same as that of the reference position signal, which is in agreement with the results of simulation.

Fig.4.28 and Fig.4.29 are the experimental results obtained using PI control to track a sinusoidal wave of the frequency of $5Hz$. The normal force in this case is set

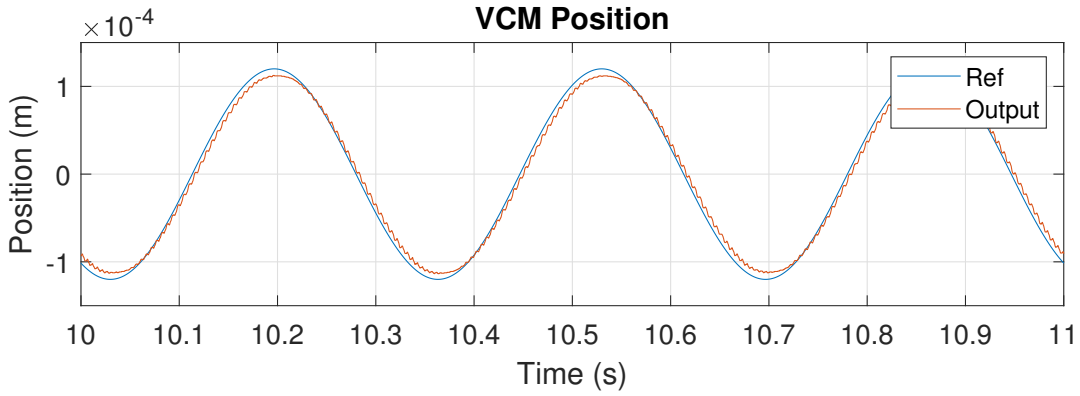

Figure 4.25: Experimental result of position reference tracking of VCM using acceleration based control with reference at $3Hz$ and normal force of $10N$

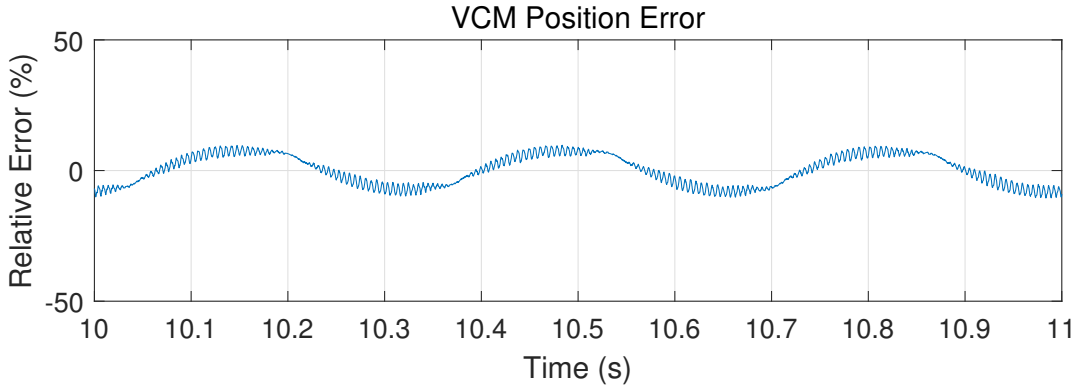

Figure 4.26: Experimental error of position reference tracking of VCM using acceleration based control with reference at $3Hz$ and normal force of $10N$

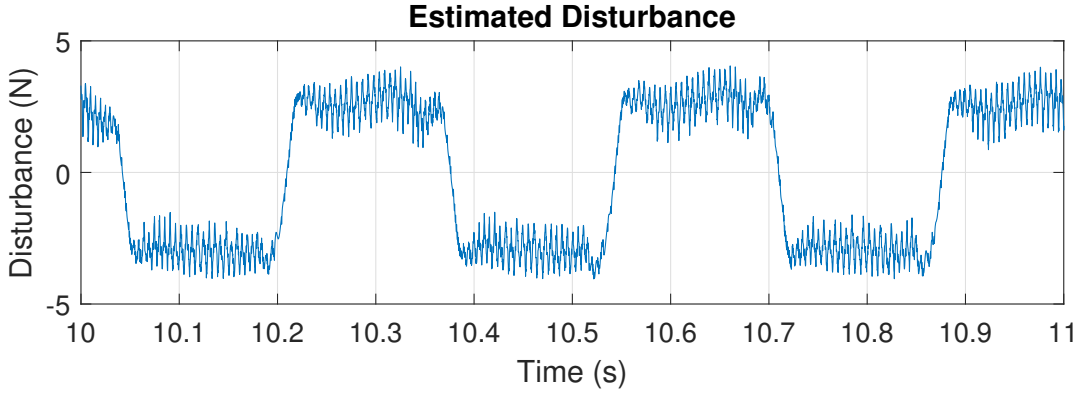

Figure 4.27: Estimated lumped input disturbance obtained using reduced order disturbance observer in position reference tracking experiment with reference at $3Hz$ and normal force of $10N$

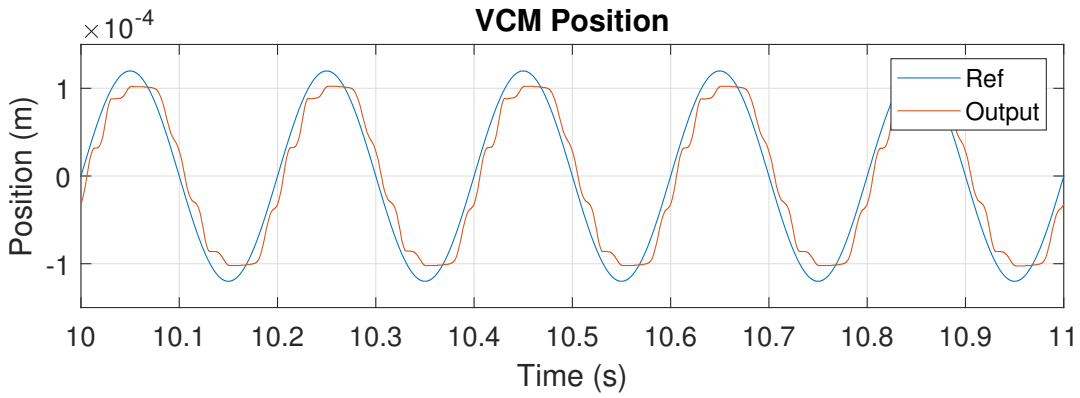

Figure 4.28: Experimental result of position reference tracking of VCM using PI control with reference at $5Hz$ and normal force of $10N$

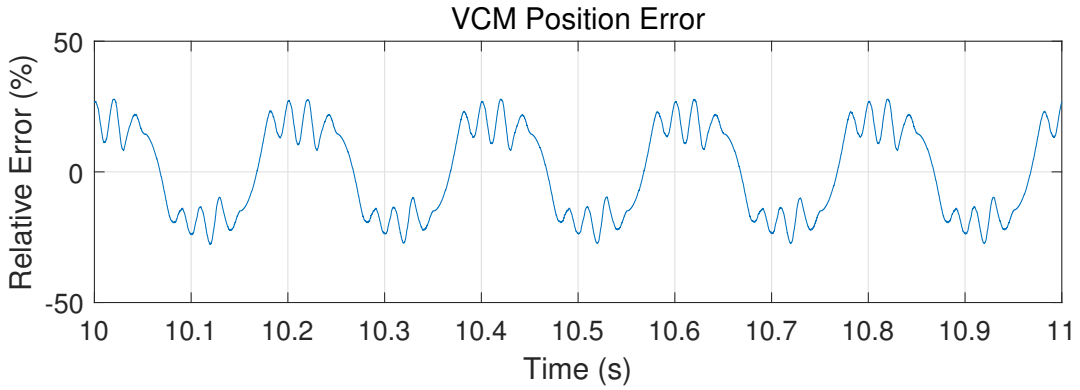

Figure 4.29: Experimental error of position reference tracking of VCM using PI control with reference at $5Hz$ and normal force of $10N$

as $10N$. The desired amplitude in this case is set as $120\mu m$. Fig.4.30 and Fig.4.31 are the experimental results obtained using acceleration based control with the same reference as for PI control. Compared with the results obtained by PI control, the error of position tracking using acceleration based is suppressed as well. In addition, Fig.4.32 shows the estimated lumped input disturbance given by the reduced order disturbance observer in experiment.

Fig.4.33 and Fig.4.34 are the experimental results obtained using PI control to track a sinusoidal wave of the frequency of $7Hz$. The normal force in this case is set as $10N$. The desired amplitude in this case is set as $120\mu m$. Fig.4.35 and Fig.4.36 are the experimental results obtained using acceleration based control with the same

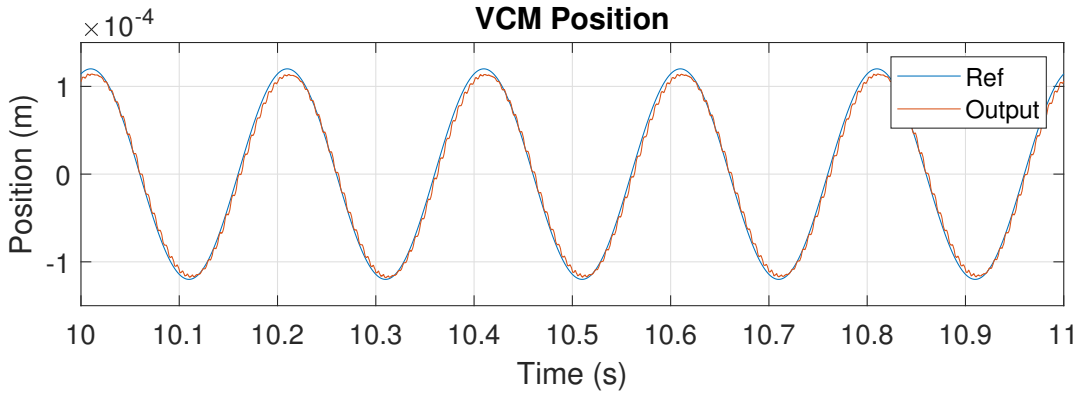

Figure 4.30: Experimental result of position reference tracking of VCM using acceleration based control with reference at $5Hz$ and normal force of $10N$

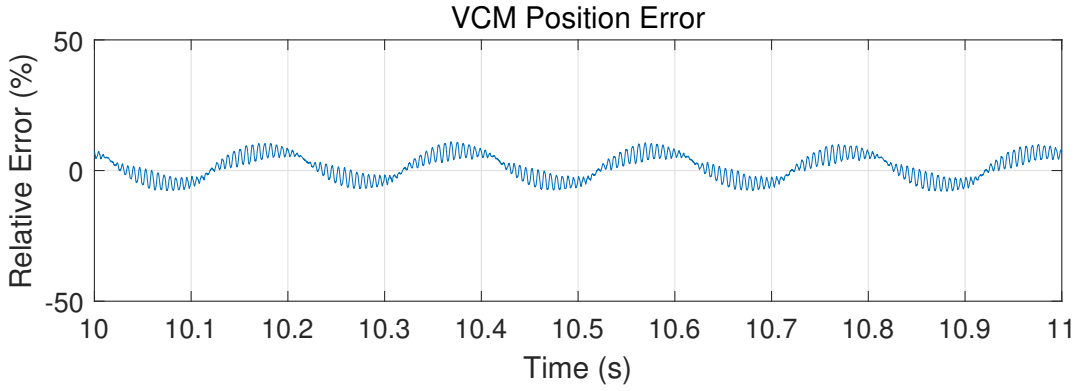

Figure 4.31: Experimental error of position reference tracking of VCM using acceleration based control with reference at $5Hz$ and normal force of $10N$

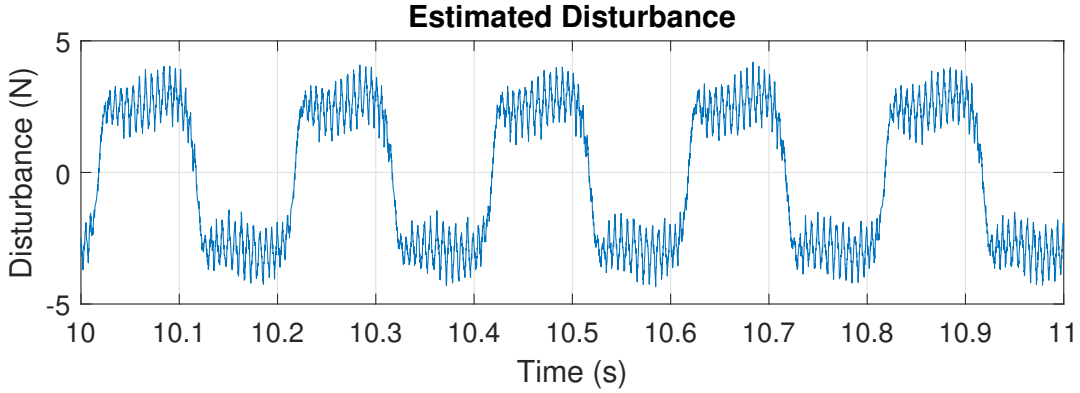

Figure 4.32: Estimated lumped input disturbance obtained using reduced order disturbance observer in position reference tracking experiment with reference at $5Hz$ and normal force of $10N$

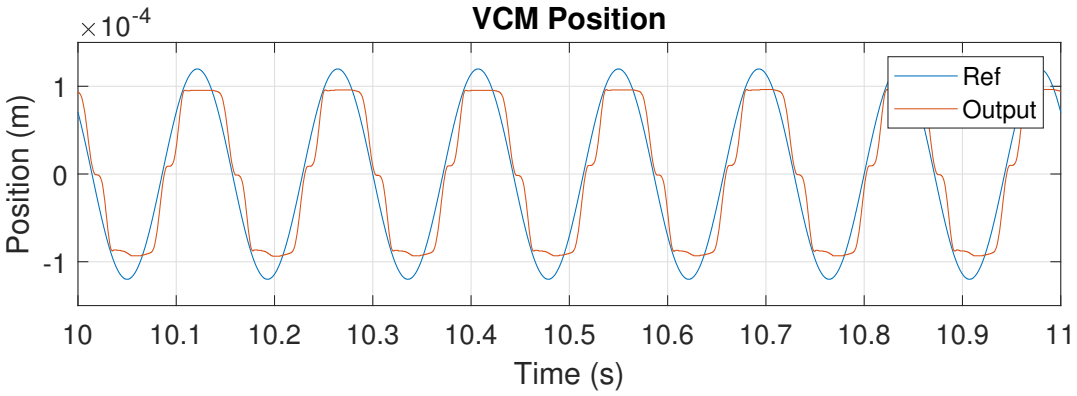

Figure 4.33: Experimental result of position reference tracking of VCM using PI control with reference at $7Hz$ and normal force of $10N$

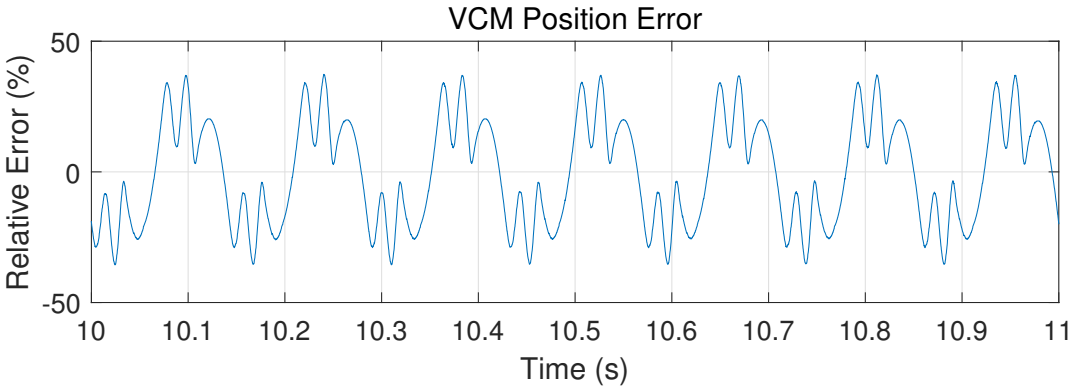

Figure 4.34: Experimental error of position reference tracking of VCM using PI control with reference at $7Hz$ and normal force of $10N$

reference as for PI control. Compared with the results obtained by PI control, the error of position tracking using acceleration based is suppressed as well. In addition, Fig.4.37 shows the estimated lumped input disturbance given by the reduced order disturbance observer in experiment.

In all the experiments above, the acceleration based control always outperforms PI control in terms of the accuracy of reference tracking. The phase lagging of the position signal with respect to the reference is suppressed using acceleration based control.

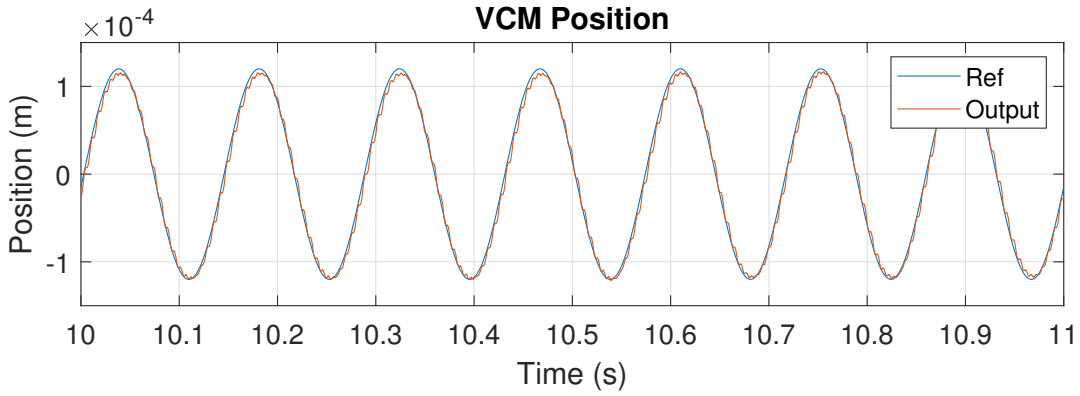

Figure 4.35: Experimental result of position reference tracking of VCM using acceleration based control with reference at $7Hz$ and normal force of $10N$

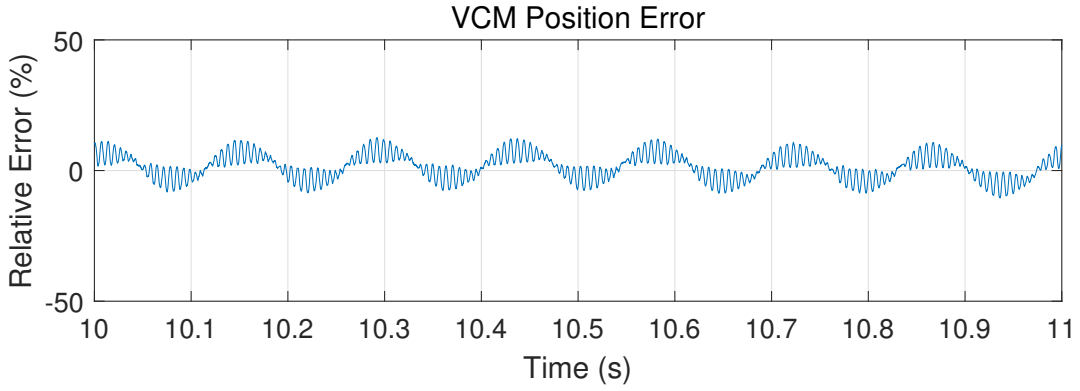

Figure 4.36: Experimental error of position reference tracking of VCM using acceleration based control with reference at $7Hz$ and normal force of $10N$

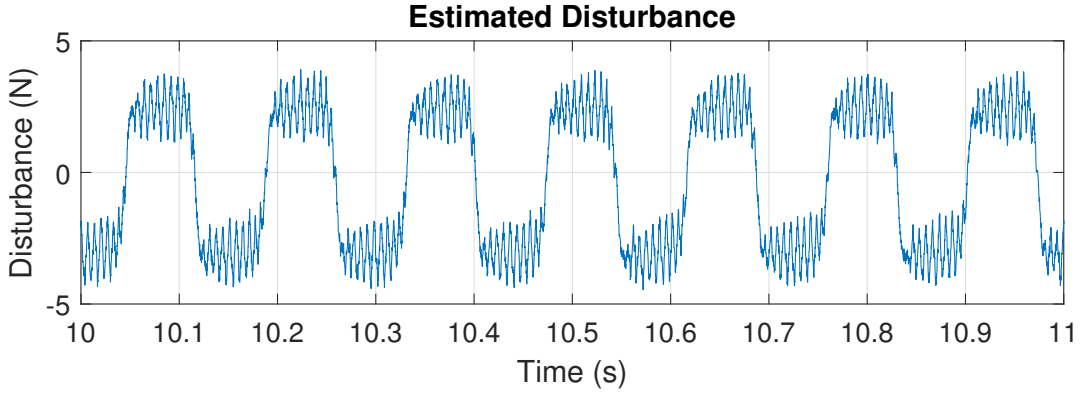

Figure 4.37: Estimated lumped input disturbance obtained using reduced order disturbance observer in position reference tracking experiment with reference at $7Hz$ and normal force of $10N$

4.6 Conclusion

The control of VCM on HFRR can be formulated as a reference tracking problem for a single degree of freedom mechanical system subject to frictional load. In this chapter, we apply acceleration based control method to VCM, where the design of a task controller that synthesise the desired system acceleration and the construction of a disturbance compensation module that estimate and compensate for the input disturbance are involved. The feedback controller is designed to realise finite-time convergence considering the minimisation on the phase difference between the output of the system and the sinusoidal reference. By assuming the relatively slow variation of frictional force and matching condition, the frictional force that distorts the output signal can be compensated through the reduced order disturbance observer at the input of the plant. In both simulations and experiments, the acceleration control with time domain reduced order disturbance observer outperforms traditional PI control significantly in terms of tracking accuracy and phase lagging suppression.

Chapter 5

Internal Model Disturbance Observer Based Control

5.1 Introduction

The lumped disturbances that include external disturbance, parameter uncertainty, and unmodeled dynamics are common to all the industrial systems, which significantly deteriorate the performance and even the stability of control systems [103]. Feedforward control is regarded as an active disturbance attenuation method, which compensates for disturbances at system input. However, the lumped disturbances are unmeasurable in most cases, which makes the implementation of feedforward control difficult. A straightforward solution to the above problem is to estimate the unmeasurable disturbances by using measurable variables such as control input and system output. Then the disturbances can be attenuated through traditional feedforward control method. Such a two-step procedure is referred to as disturbance observer based control. For the control of VCM on HFRR, the unwanted effect to the system output due to frictional load can be regarded as external disturbance, which can be attenuated by applying disturbance observer based control.

There are different disturbance observer techniques proposed so far. In this chapter, we investigate the adaptation of internal model principle to the design of disturbance observer. Internal model principle states that a system can achieve asymptotic

tracking of reference once the generating model of the reference that is represented as the output of an exogenous system is embedded into the controller [104]. The frictional load that dominates the external disturbances to the VCM on HFRR is periodic in a reciprocating motion. Internal model disturbance observer can be constructed based on that observation. Compared with traditional disturbance observer with no explicit assumption on the characteristics of the input disturbance in the frequency domain, the internal model disturbance observer can achieve a higher tracking accuracy and lower harmonics in the error signal. In addition, simulations and experiments to verify the design of internal model disturbance observer are presented.

5.2 Disturbance Observer Based Control

The output of a SISO system considering input disturbance and model uncertainty in s domain can be written as:

$$Y(s) = [G_n(s) + \Delta G(s)] \cdot [U(s) + W(s)] = G_n(s) \cdot [U(s) + D(s)] \tag{5.2.1}$$

where $U(s)$ and $Y(s)$ are plant input and output respectively. $G_n(s)$ and $\Delta G(s)$ are nominal transfer function and uncertainty of the plant. $W(s)$ is the unmeasurable external disturbance. We define the lumped input disturbance as: [103]

$$D(s) = \frac{\Delta G(s)}{G_n(s)} \cdot U(s) + \left[1 + \frac{\Delta G(s)}{G_n(s)}\right] \cdot W(s) \tag{5.2.2}$$

Then the output of the system can be written as:

$$Y(s) = G_n(s) \cdot [U(s) + D(s)] \tag{5.2.3}$$

It is desirable that the effect of the lumped input disturbance $D(s)$ on system output be minimised, which can be done by compensating $D(s)$ at the input of the system as follows:

$$U(s) = U_n(s) + U_d(s) \tag{5.2.4}$$

where U_d should be defined as:

$$U_d(s) = -D(s) \tag{5.2.5}$$

Therefore, the lumped input disturbance should be obtained to allow compensation at system input. According to the definition of $D(s)$, it can be derived as:

$$D(s) = \frac{Y(s)}{G_n(s)} - U(s) \tag{5.2.6}$$

However, for the plant with the proper transfer function, of which the order of the denominator is larger than that of the numerator, the equation above can not be implemented due to the causality issue. Usually, a filter can be introduced to the equation to construct the disturbance observer that estimates the disturbance satisfying the so-called matching condition. The condition states that the disturbance(s) should act on the system via the same channel(s) as the control input(s) or can be transferred to the same channel(s) as the control input(s) by coordinate transform [52] [54]. For mismatched disturbances, an integral action in a feedback control law can be applied to remove offset of the closed-loop system. In this study, we only focus on the estimation and compensation for disturbances that satisfy the matching condition. The expression for disturbance observer in s domain for minimum phase SISO system subjects to matched disturbance is:

$$\hat{D}(s) = Y(s) \cdot \frac{Q(s)}{G_n(s)} - U(s) \cdot Q(s) \tag{5.2.7}$$

where $\hat{D}(s)$ represents the estimate of $D(s)$. The filter $Q(s)$ is usually designed as a low-pass filter such that:

- The relative degree of $Q(s)$, which is the difference between the order of the denominator and the order of the numerator, should be no less than that of the nominal plant model $G_n(s)$. This is done to assure the causality of the disturbance observer.
- In the domain of low-frequency or frequency of interest, the response of $Q(s)$ should approach to unity as far as possible in order to minimise the error of disturbance estimation.

Fig. 5.1 shows the block diagram of the closed-loop system with frequency domain disturbance observer. $Y_r(s)$ and $Y(s)$ are reference signal and the system

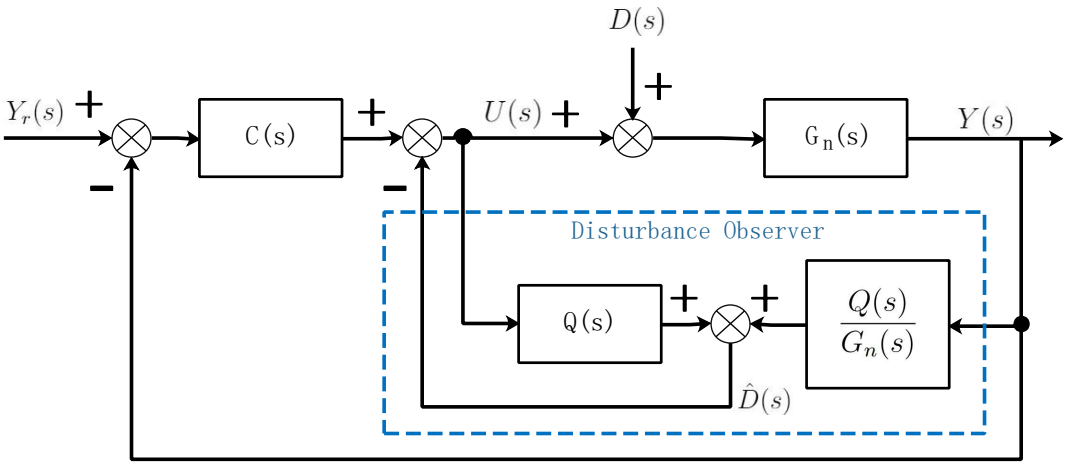

Figure 5.1: Block diagram of frequency domain disturbance observer based control

output. $C(s)$ is the feedback controller. $D(s)$ and $\hat{D}(s)$ are the lumped input disturbance and its estimate given by the disturbance observer. $G_n(s)$ is the nominal plant model. $Q(s)$ is the filter for disturbance observer. As it shown in Fig. 5.1, the disturbance observer based control scheme consists of two parts: a feedback control $C(s)$ designed for the nominal plant and a feedforward control designed for the compensation of the lumped input disturbance. The feedback controller $C(s)$ is designed based on the nominal model of the plant. As the nominal model of the system, in this case, is a linear time-invariant system, there are a variety of powerful linear control design tools that can be used in the design procedure, such as root locus and bode plot. The design specifications such as settling time in step response and phase margin can be applied to quantitatively describe the desired performance of the closed loop system. The output of the closed-loop system with disturbance observer can then be written as:

$$Y(s) = T_{yr}(s)Y_r(s) + T_{yd}(s)D(s) \tag{5.2.8}$$

where T_{yr} represents the relation between the output $Y(s)$ and the reference signal $Y_r(s)$ in terms of transfer function; T_{yd} represents the relation between the output $Y(s)$ and the lumped input disturbance $D(s)$ in terms of transfer function. The expressions for them are:

$$T_{yr}(s) = \frac{C(s)G_n(s)}{1 + C(s)G_n(s)} \tag{5.2.9}$$

$$T_{yd}(s) = \frac{G_n(s)\left[1 - Q(s)\right]}{1 + C(s)G_n(s)} \tag{5.2.10}$$

As the filter $Q(s)$ is a low-pass filter, it follows that:

$$\lim_{\omega \to 0} Q(j\omega) = 1 \tag{5.2.11}$$

Hence, we can show that:

$$\lim_{\omega \to 0} T_{ry}(j\omega) = \lim_{\omega \to 0} \frac{G_n(j\omega)C(j\omega)}{1 + G_n(j\omega)C(j\omega)} \tag{5.2.12}$$

and

$$\lim_{\omega \to 0} T_{dy}(j\omega) = \lim_{\omega \to 0} \frac{G_n(j\omega)\left[1 - Q(j\omega)\right]}{1 + C(j\omega)G_n(j\omega)} \tag{5.2.13}$$

$$= \lim_{\omega \to 0} \frac{G_n(j\omega)\left[1 - 1\right]}{1 + C(j\omega)G_n(j\omega)} = 0 \tag{5.2.14}$$

Therefore, the lumped input disturbance within the passband of the low-pass filter $Q(s)$ can be attenuated significantly. It is obvious that the disturbance observer applying low-pass filter does not take the high frequency component of the lumped input disturbance into account. In fact, it is reasonable to discard high frequency component of disturbance in the design of disturbance observer in most cases as: [53]

- The measurement is corrupted by the noise that typically at high frequency. It is common practice to mitigate the effect of noise by signal filtering. In the case of disturbance estimation, such treatment will lead to the loss of disturbance information at high frequency band.
- The effect of high frequency component of disturbance can be filtered out by the inertia of the plant under control.
- Due to the limited bandwidth of actuator, the high frequency component of disturbance can not be attenuated even it has been estimated accurately by disturbance observer.

5.3 Internal Model Disturbance Observer

5.3.1 Disturbance Observer in Frequency Domain

The nominal transfer function of the plant $G_n(s)$ is given by:

$$G_n(s) = \frac{K_s}{LM \cdot s^3 + (LC + RM) \cdot s^2 + (K_s^2 + RC + LK) \cdot s + RK} \tag{5.3.1}$$

where K_s is motor constant; L is the inductance of motor coil; M is the total mass of the moving components including motor shaft and motor coil; C is the damping coefficient of the moving components; K is spring stiffness; R is the resistance of motor coil. The input of the plant is voltage that applied to the terminals of motor coil. The output of the plant is the position of motor shaft. The transfer function implies a third order system with relative order of 3. Hence, the filter $Q(s)$ should be designed as a low-pass filter with minimum relative order of 3.

As the impulse response of an ideal low-pass filter is infinitely long, it can not be implemented in practice [105]. Therefore, various approximation methods have been introduced to the implementation of analog low-pass filters. The low-pass filters based on well-known approximation methods include Butterworth Filter, Chebyshev Filter and Elliptic Filter [106] [107] [108]. In addition to cut-off frequency, passband ripple and stopband attenuation are used to specify the design requirements of these approximated low-pass filter. For different types of approximation methods, one or more of these attributes are selected for optimisation [109] [110].

Table. 5.1 shows the magnitude responses of different types of analog filter. In the expression for the magnitude response of Butterworth Filter, N represents the order of the filter; Ω_C is the cut-off frequency. In the expression for the magnitude response of Chebyshev Filter I, ε is the ripple factor that determines the amplitude of ripple. The passband ripple is the minimum value of magnitude in passband, which is equal to $\frac{1}{\sqrt{1+\varepsilon^2}}$. Ω_P is the passband edge angular frequency, which is the angular frequency corresponding to $H(j\Omega) = \frac{1}{\sqrt{1+\varepsilon^2}}$. $T_N(x)$ is the Chebyshev polynomial

Filter	Magnitude Response
Butterworth Filter	$\lvert H(j\Omega)\rvert^2 = \frac{1}{1+\left(\frac{\Omega}{\Omega_C}\right)^{2N}}$
Chebyshev Filter I	$\lvert H(j\Omega)\rvert^2 = \frac{1}{1+\varepsilon^2 T_N^2\left(\frac{\Omega}{\Omega_p}\right)}$
Chebyshev Filter II	$\lvert H(j\Omega)\rvert^2 = \frac{1}{1+\varepsilon^2\left[\frac{T_N(\gamma)}{T_N(\lambda)}\right]^2}$
Elliptic Filter	$H(j\Omega) = \frac{1}{1+\varepsilon^2 R_N^2\left(\xi, \frac{\Omega}{\Omega_C}\right)}$

Table 5.1: Comparison of analog filters in terms of magnitude response

of order N given by:

$$T_N(x) = \begin{cases} \cos\left(N\cos^{-1}x\right) & |x| \leq 1 \\ \cosh\left(N\cosh^{-1}x\right) & |x| > 1 \end{cases} \tag{5.3.2}$$

In the expression for the magnitude response of Chebyshev Filter II, we have $\gamma = \frac{\Omega_S}{\Omega_P}$ and $\lambda = \frac{\Omega_S}{\Omega}$, where Ω_S is stopband edge angular frequency. In the expression of Elliptic Filter, R_N is the n-th order elliptic rational function, of which the roots are related to the Jacobi elliptic sine function. ξ is the selectivity factor, which is used to define the ripple in the stopband.

The advantages and disadvantages of each type of the filter presented in Table.5.1 are presented as below:

- Butterworth Filter: it shows maximally flat magnitude response and linear phase response in passband. However, the magnitude response decays slowly above the cut-off frequency [111] [112].

- Chebyshev Filter I: The cut-off is much sharper than that of Butterworth Filter. However, the filter is equiripple in the passband and the phase response is nonlinear.

- Chebyshev Filter II: The cut-off is much sharper than that of Butterworth Filter. However, the filter is equiripple in the stopband and the phase response is nonlinear.

- Elliptic Filter: The cut-off is sharper than that of Chebyshev Filter. However, the filter is equiripple both in the passband and in the stopband. In addition, the phase response is nonlinear that leads to group delay distortion.

When implementing the filter $Q(s)$ for disturbance observer, it is expected that the magnitude of $T_{dy}(j\Omega)$ is always closed to zero in low frequency band. In addition, the phase response of the filter in passband should be linear as the least group delay distortion is desirable for the process of disturbance estimation. Therefore, $Q(s)$ is designed as a third order Butterworth low-pass filter [113] [114]. The transfer function of a third order Butterworth filter is given as:

$$|Q_{but}(j\omega)|^2 = \frac{K_{but}^2}{1 + \left(\frac{j\omega}{j\omega_c}\right)^{2n}} \tag{5.3.3}$$

where the order of the filter $n = 3$. ω_c is the cutoff frequency.

5.3.2 Embedding Internal Model

According to the LuGre friction model that applied to the study, the friction exerts on the shaft of VCM should be a function of velocity. In the case of HFRR control application, the reference trajectory of the shaft of VCM $x_{ref}(t)$ should be a sinusoidal curve defined as:

$$x_{ref}(t) = A_{ref} \cdot sin(2\pi \cdot f_{ref} \cdot t) \tag{5.3.4}$$

where A_{ref} is the desired amplitude; f_{ref} is the desired frequency. Therefore, the desired velocity $v_{ref}(t)$ can be obtained by taking the derivative of the continuous reference trajectory function:

$$v_{ref}(t) = A_{ref} \cdot 2\pi \cdot f_{ref} \cdot cos(2\pi \cdot f_{ref} \cdot t) \tag{5.3.5}$$

The above expression together with LuGre model implies that the resultant friction should contain a component at the desired frequency of motion. However, the value of the friction coefficient for the contacting surface on HFRR is varying along the trajectory of motion. In [115], the researchers find that the data acquired from the

force sensor reflects several harmonic components that superimpose on the vibration corresponding to the fundamental frequency. They use the term momentary coefficient of friction to distinguish them with the standard coefficient of friction corresponding to the fundamental frequency.

To simplify the analysis, we assume the projection of the friction that exerts on the shaft of VCM into the range space of the control disturbance matrix is dominated and periodic. Hence, the disturbance can be expressed as a sum of the fundamental sinusoidal component and its harmonics: [103]

$$d_h(t) = \sum_{k=1}^{N_h} D_k \sin\left(k\omega_0 t + \varphi_k\right) \tag{5.3.6}$$

where ω_0 is the fundamental angular frequency; N_h is the order of the highest harmonic component; φ_k is the phase corresponding to k-th harmonic component. In the case of VCM control for HFRR, the value of ω_0 is equal to the desired angular frequency of vibration. At this point, we have constructed the simplified generating model of disturbance.

The internal model principle states that a system can achieve asymptotic tracking of reference once the generating model of the reference that is represented as the output of an exogenous system is embedded into the controller [104]. As the problem of designing an observer to track the states of the system can be regarded as the dual problem of designing a controller to tracking the reference, the internal model principle can be applied to disturbance observer to eliminate the structured disturbance asymptotically [116]. This can be achieved by embedding the generating model of the disturbance into the low pass filter $Q(s)$ of the disturbance observer [117].

The generating model of the disturbance with fundamental frequency equals to f_0 in s domain can be constructed using resonant terms as that of Proportional Resonant (PR) control. The expression for each resonant term can be expressed as:

$$R_k(s) = \frac{2a_k s}{s^2 + (k\omega_0)^2} \tag{5.3.7}$$

where $\omega_0 = 2\pi f_0$ represents the fundamental angular frequency of the disturbance; k represents the order of the harmonics. The magnitude response of the resonant

term implies that:

$$\lim_{\omega \to k\omega_0} R_k(j\omega) = \infty \tag{5.3.8}$$

Representing the transfer function of a third order Butterworth Filter as:

$$Q_B(s) = \frac{n_0}{d_3 \cdot s^3 + d_2 \cdot s^2 + d_1 \cdot s + d_0} \tag{5.3.9}$$

The resonant term can be embedded into the filter as:

$$Q_{BR_K}(s) = \frac{n_0 + \frac{2a_k s}{s^2 + (k\omega_0)^2}}{d_3 \cdot s^3 + d_2 \cdot s^2 + d_1 \cdot s + d_0 + \frac{2a_k s}{s^2 + (k\omega_0)^2}} \tag{5.3.10}$$

It can be found that due to the introduction of the resonant term, the magnitude response of the modified filter $Q_{BR_K}(s)$ can be given as:

$$Q_{BR_K}(j\omega) \approx \begin{cases} 1, & \omega = k\omega_0 \\ Q_B(s), & \text{elsewhere} \end{cases} \tag{5.3.11}$$

As $Q_B(s)$ is the transfer function of a third order Butterworth Filter, its magnitude response above zero frequency is less than than unity. The introduction of the resonant term can compensate the decrease of magnitude response at the angular frequency $k\omega_0$. In this way, the transfer function $T_{dy}(s)$ that represents the relation between the output of the system and disturbance at the angular frequency $k\omega_0$ is given as:

$$T_{dy}(jk\omega_0) = \frac{G_n(jk\omega_0)\left[1 - Q_{BR_K}(jk\omega_0)\right]}{1 + C(j\omega)G_n(j\omega)} \approx 0 \tag{5.3.12}$$

Therefore, by introducing the resonant term at the frequency corresponding to the period of the input disturbance to the filter, better performance of the closed-loop system in terms of disturbance attenuation can be achieved. For disturbance containing harmonics, the corresponding resonant terms can be combined in series form as: [103]

$$R_h(s) = \prod_{k=1}^{K_h} \left[1 + R_k(s)\right] \tag{5.3.13}$$

where K_h is the order of the highest harmonics considered in design. In digital implementation, due to the limitation on the word length, the ideal resonant terms should be approximated as:

$$MR_k(s) = \frac{2a_k s}{s^2 + 2b_k s + (k\omega_0)^2} \tag{5.3.14}$$

Here, we have $0 < b_k << a_k$ to limit the word length in digital implementation [118]. Hence, the lumped resonant term is approximated as:

$$MR_h(s) = \prod_{k=1}^{K_h} [1 + MR_k(s)] \tag{5.3.15}$$

Finally, considering the issue of digital implementation, the filter used in internal model disturbance observer based on a third order Butterworth Filter can be constructed as:

$$Q_{IM}(s) = \frac{MR_h(s)}{d_{n3} \cdot s^3 + d_{n2} \cdot s^2 + d_{n1} \cdot s + MR_h(s)} \tag{5.3.16}$$

where $d_{nx} = \frac{d_x}{d_0}$ are the normalised coefficients for the original denominator polynomial of the third order Butterworth Filer.

Remark V.1: Conventional disturbance observer makes no explicit assumption on the characteristics of the input disturbance. The Q filter, in this case, is designed based on a classical low pass filter prototype. As a result, the estimated disturbance within the pass-band of the Q filter can be attenuated, which degrades the performance of disturbance estimation. Traditionally, increasing the bandwidth of the Q filter can improve the disturbance estimation accuracy with the price of introducing measurement noise. However, internal model disturbance improves its performance by embedding the generating model of the disturbance without changing the cut-off frequency of the Q filter. In this way, the disturbance estimation accuracy can be improved without sacrificing noise immunity capability.

In our study, for simplicity, we only consider the fundamental component of the disturbance, which is same as the frequency of reciprocating motion of VCM on HFRR.

5.4 Simulations

In simulation, the reference position signal is a sinusoidal wave of the frequency of $5Hz$. The amplitude is set as $100\mu m$. Fig. 5.2 shows the output of VCM in reference tracking using PI control. Fig.5.3 shows the error of position tracking in this case. It can be found that due to the effect of frictional load, the output position

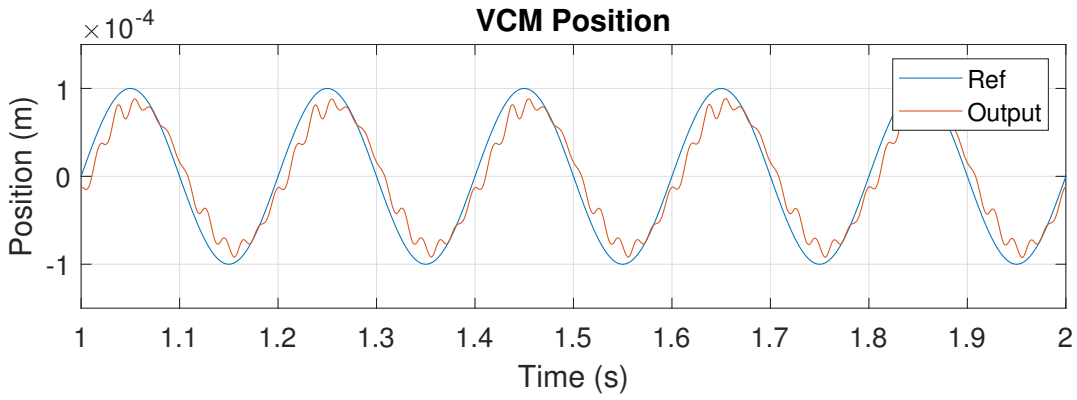

Figure 5.2: Simulated VCM position tracking using PI control

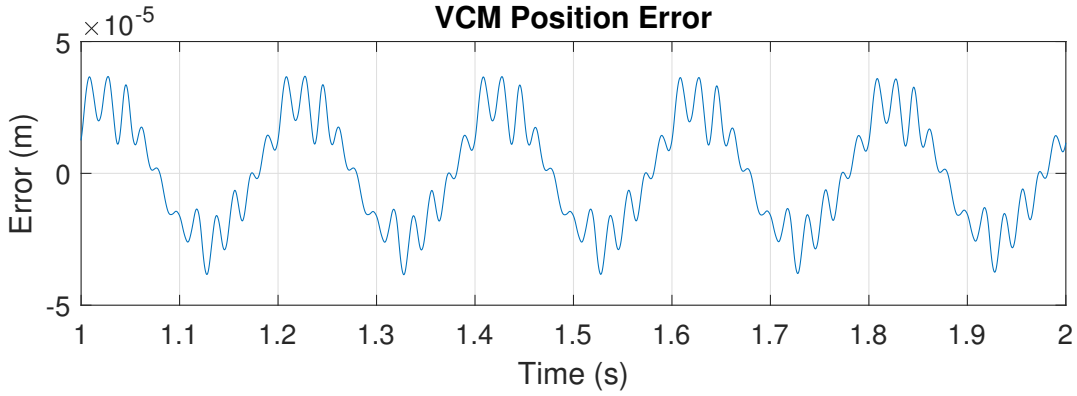

Figure 5.3: Simulated VCM position tracking error using PI control

signal lags the reference and the shape of it is distorted as well. The error of position contains significant harmonics.

Fig.5.4 shows the position tracking of VCM under PI control with disturbance compensation using traditional frequency domain disturbance observer. It can be found it outperforms pure PI control in terms of output error. Fig.5.5 shows the error of position tracking in this case.

Fig.5.6 shows the position tracking of VCM under PI control with disturbance compensation using internal model disturbance observer. It can be found it outperforms the previous one using traditional disturbance observer in terms of output error. Fig.5.7 shows the error of position tracking in this case.

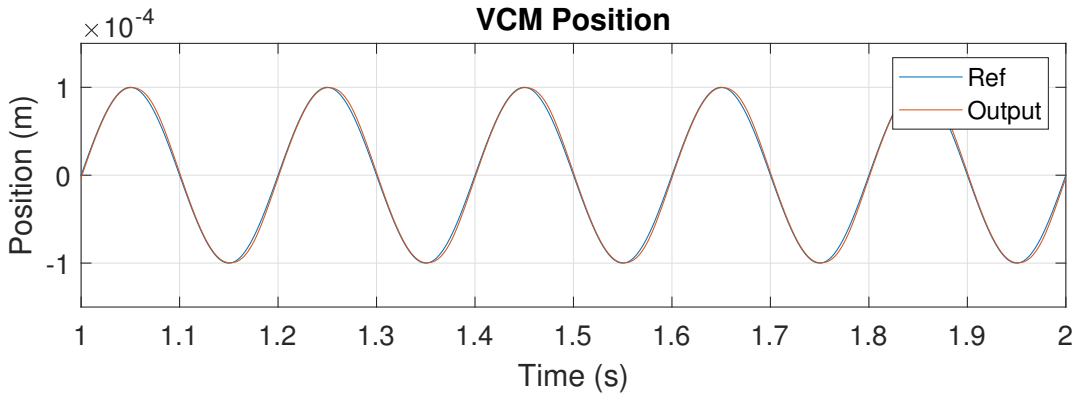

Figure 5.4: Simulated VCM position tracking using traditional disturbance observer for compensation

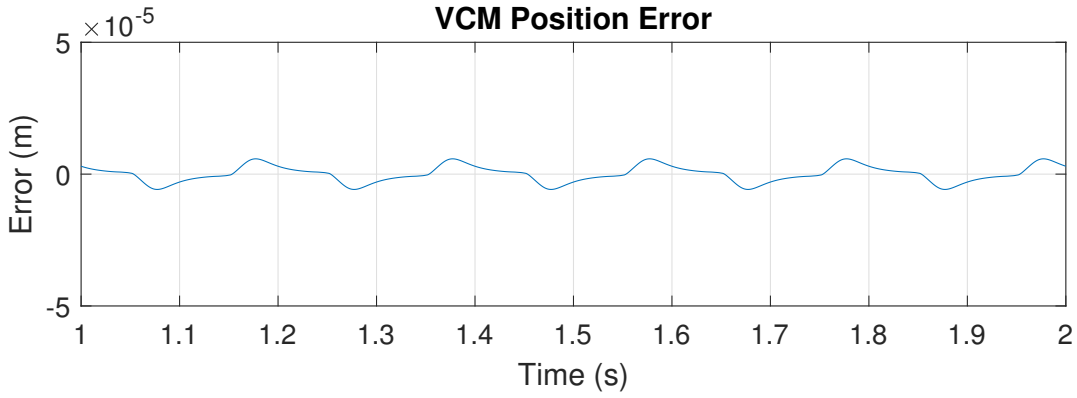

Figure 5.5: Simulated VCM position tracking error using traditional disturbance observer for compensation

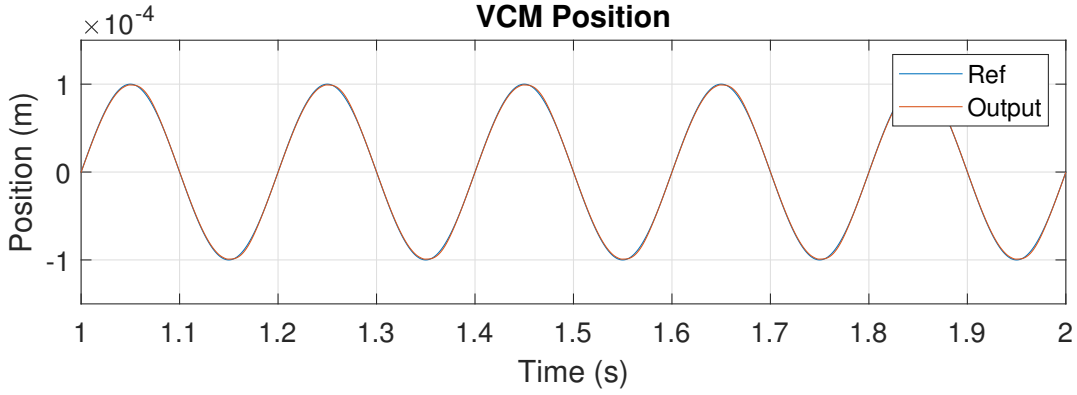

Figure 5.6: Simulated VCM position tracking using internal model disturbance observer for compensation

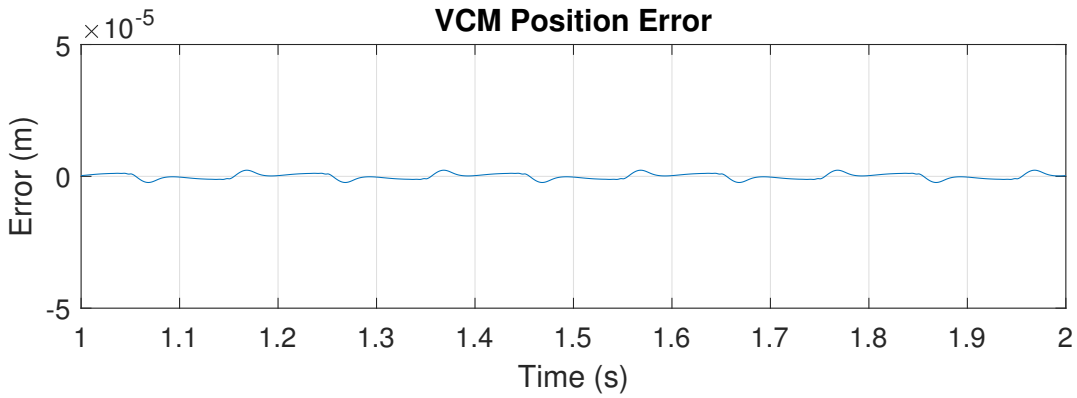

Figure 5.7: Simulated VCM position tracking error using internal model disturbance observer for compensation

5.5 Experiment Results

To simplify the experiments, the types of specimen are kept as same in each test. The settings of remaining experimental conditions applied in experiments are shown in Table. 5.2.

In Table 5.2, there are 18 sets of experimental conditions. The frequency varies from $3Hz$ to $7Hz$. The normal varies from $6N$ to $10N$. The specimens in all experiments are chosen as aluminium plate with petroleum ether (Al&PE) covered on top of them. To make sure the initial conditions such as surface roughness are same in each experiment, both aluminium plate and petroleum ether between contacting surfaces should be replaced at the end of each test. To assess the performance of the proposed control method, comparison among conventional PI control, PI control with compensation by traditional disturbance observer, and PI control with compensation by internal model disturbance observer have been done.

Fig.5.8 and Fig.5.9 are the experimental results obtained using PI control to track a sinusoidal wave of the frequency of $3Hz$. The normal force in this case is set as $6N$. The desired amplitude in this case is set as $120\mu m$. It can be found that the output position of VCM is distorted due to disturbance. Fig.5.10 and Fig.5.11 are the experimental results obtained using traditional disturbance observer compensated PI control with the same reference as for PI control. Compared with the results obtained by PI control, the error of position tracking with compensation given by

Frequency(Hz)	Amplitude(μm)	Normal Force (N)	Control Method
3Hz	$120\mu m$	$6N$	PI Control
3Hz	$120\mu m$	$6N$	PI + DOB Control
3Hz	$120\mu m$	$6N$	PI + IMDOB Control
5Hz	$120\mu m$	$6N$	PI Control
5Hz	$120\mu m$	$6N$	PI + DOB Control
5Hz	$120\mu m$	$6N$	PI + IMDOB Control
7Hz	$120\mu m$	$6N$	PI Control
7Hz	$120\mu m$	$6N$	PI + DOB Control
7Hz	$120\mu m$	$6N$	PI + IMDOB Control
3Hz	$120\mu m$	$10N$	PI Control
3Hz	$120\mu m$	$10N$	PI + DOB Control
3Hz	$120\mu m$	$10N$	PI + IMDOB Control
5Hz	$120\mu m$	$10N$	PI Control
5Hz	$120\mu m$	$10N$	PI + DOB Control
5Hz	$120\mu m$	$10N$	PI + IMDOB Control
7Hz	$120\mu m$	$10N$	PI Control
7Hz	$120\mu m$	$10N$	PI + DOB Control
7Hz	$120\mu m$	$10N$	PI + IMDOB Control

Table 5.2: Experimental conditions for comparisons among PI control, PI control with compensation by classical disturbance observer and PI control with compensation by internal model disturbance observer (DOB is short for disturbance observer; IMDOB is short for internal model disturbance observer.)

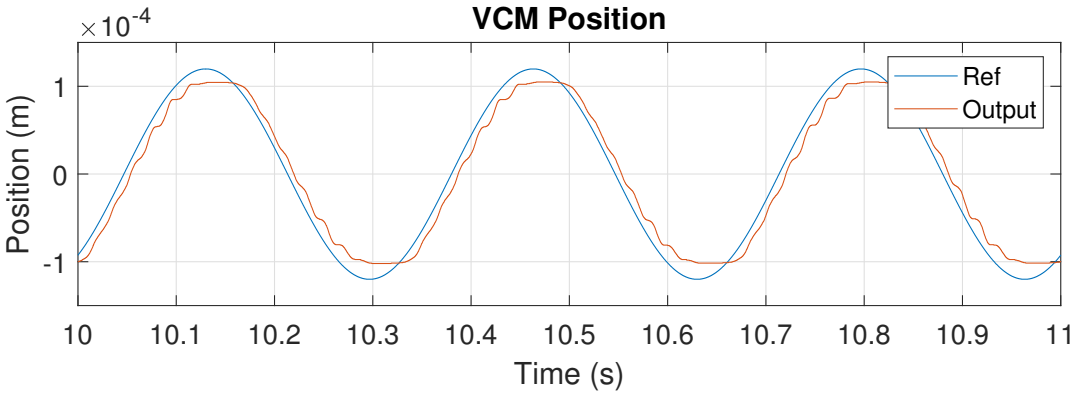

Figure 5.8: Experimental result of position reference tracking of VCM using PI control with reference at $3Hz$ and normal force of $6N$

disturbance observer is suppressed significantly. In addition, Fig.5.12 shows the estimated lumped input disturbance given by the traditional disturbance observer in experiment. The fundamental period of disturbance is the same as that of the reference position signal, which is in agreement with the results of simulation. Fig.5.13 and Fig.5.14 are the experimental results obtained using internal model disturbance observer compensated PI control with the same reference as for PI control. Compared with the results obtained by traditional disturbance observer compensated PI control, the error of position tracking with compensation given by internal model disturbance observer is suppressed even further. In addition, Fig.5.15 shows the estimated lumped input disturbance given by the internal model disturbance observer in experiment.

Fig.5.16 and Fig.5.17 are the experimental results obtained using PI control to track a sinusoidal wave of the frequency of $5Hz$. The normal force in this case is set as $6N$. The desired amplitude in this case is set as $120\mu m$. It can be found that the output position of VCM is distorted due to disturbance. Fig.5.18 and Fig.5.19 are the experimental results obtained using traditional disturbance observer compensated PI control with the same reference as for PI control. Compared with the results obtained by PI control, the error of position tracking with compensation given by disturbance observer is suppressed significantly. In addition, Fig.5.20 shows the estimated lumped input disturbance given by the traditional disturbance observer in

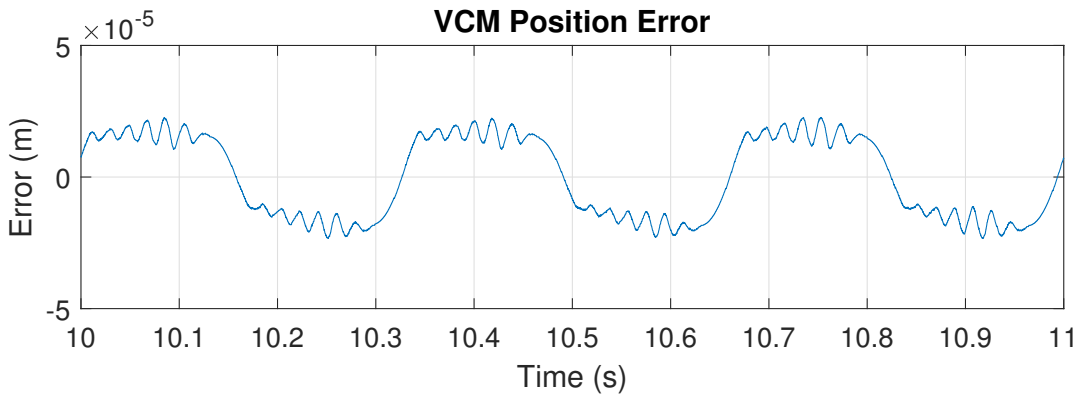

Figure 5.9: Experimental error of position reference tracking of VCM using PI control with reference at $3Hz$ and normal force of $6N$

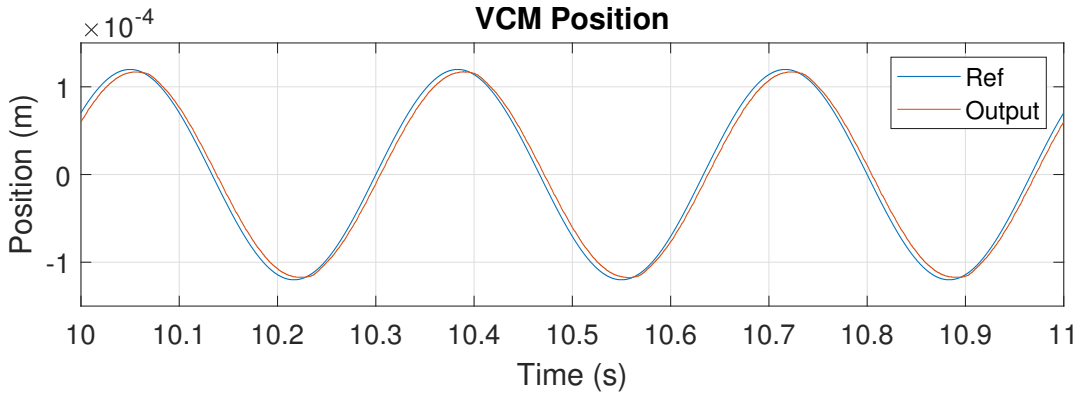

Figure 5.10: Experimental result of position reference tracking of VCM using traditional disturbance observer compensated PI control with reference at $3Hz$ and normal force of $6N$

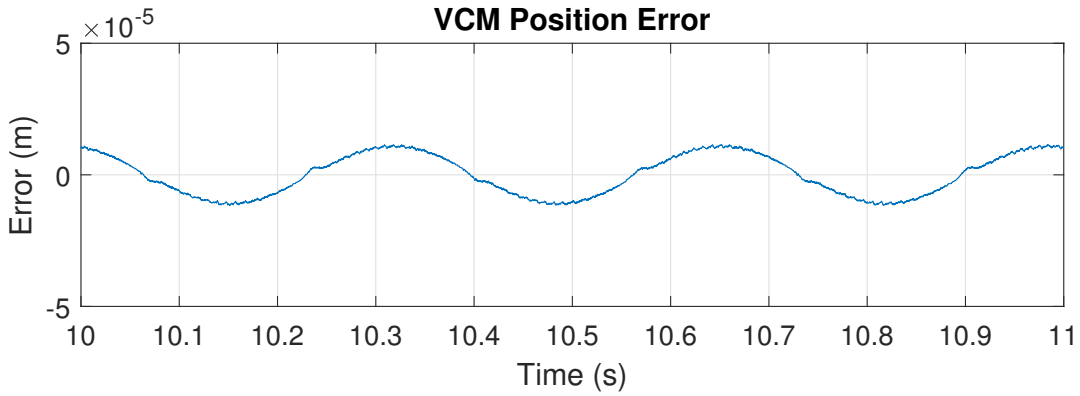

Figure 5.11: Experimental error of position reference tracking of VCM using traditional disturbance observer compensated PI control with reference at $3Hz$ and normal force of $6N$

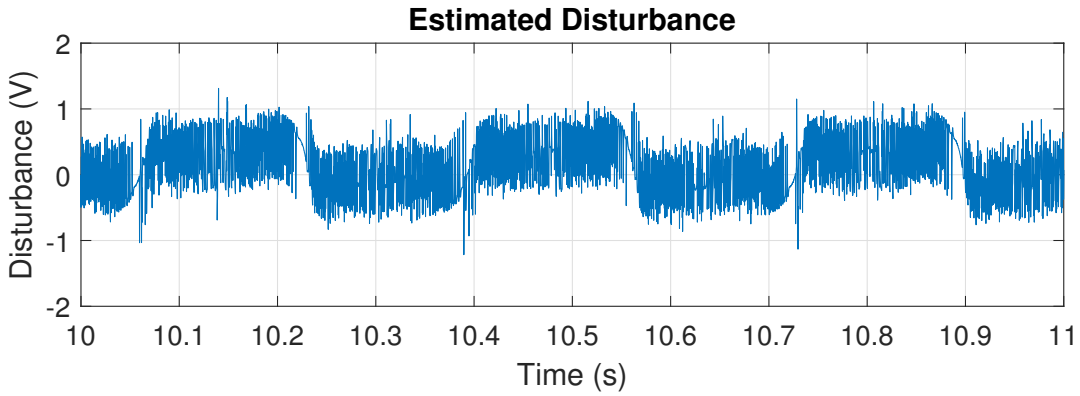

Figure 5.12: Estimated lumped input disturbance obtained using traditional disturbance observer in position reference tracking experiment with reference at $3Hz$ and normal force of $6N$

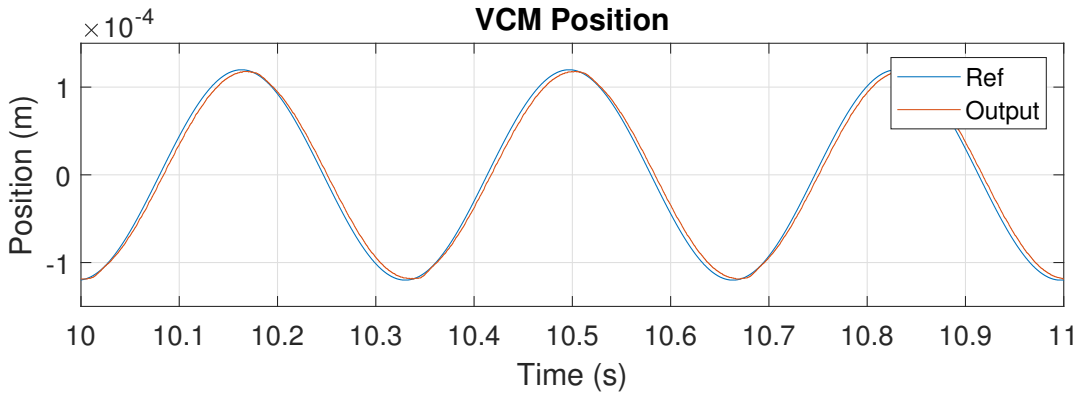

Figure 5.13: Experimental result of position reference tracking of VCM using internal model disturbance observer compensated PI control with reference at $3Hz$ and normal force of $6N$

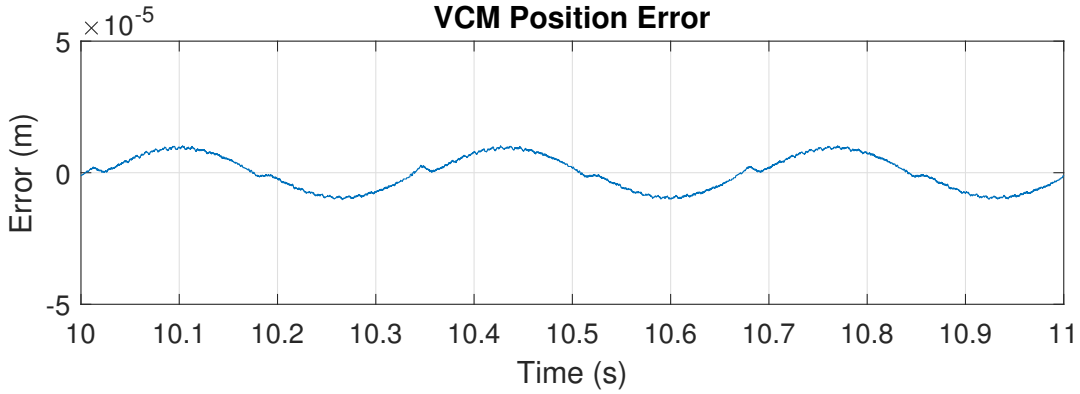

Figure 5.14: Experimental error of position reference tracking of VCM using internal model disturbance observer compensated PI control with reference at $3Hz$ and normal force of $6N$

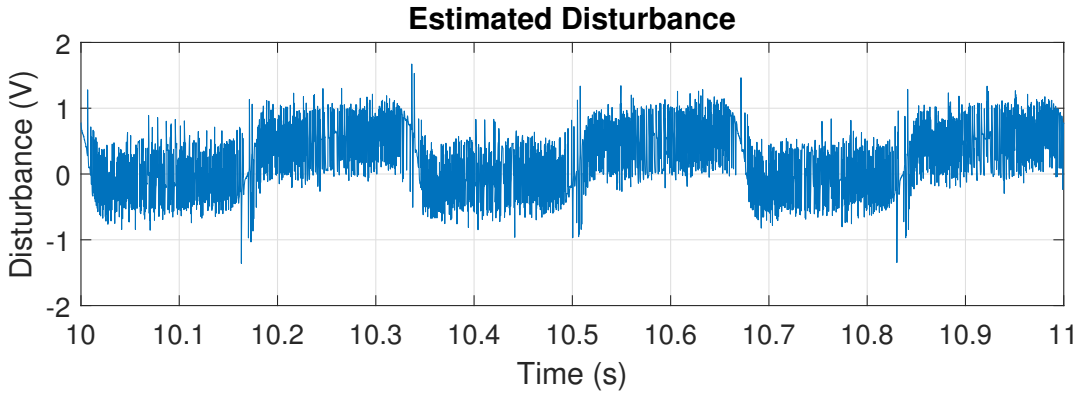

Figure 5.15: Estimated lumped input disturbance obtained using internal model disturbance observer in position reference tracking experiment with reference at $3Hz$ and normal force of $6N$

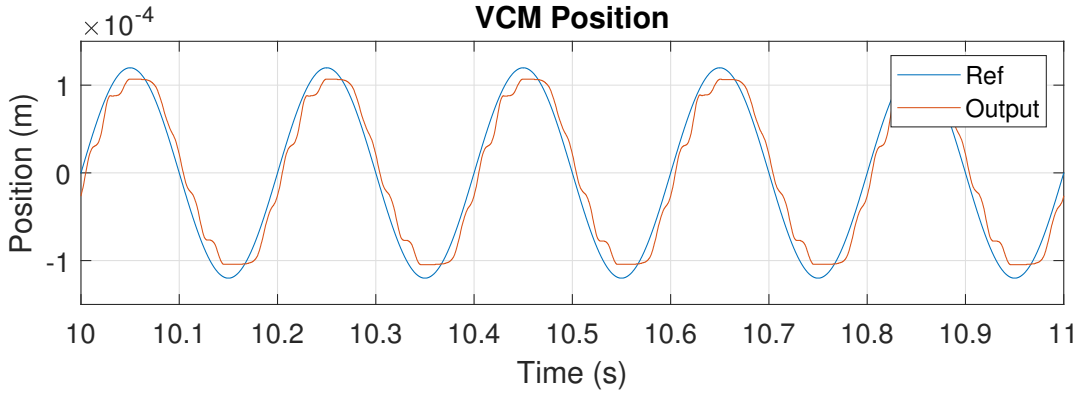

Figure 5.16: Experimental result of position reference tracking of VCM using PI control with reference at $5Hz$ and normal force of $6N$

experiment. The fundamental period of disturbance is the same as that of the reference position signal, which is in agreement with the results of simulation. Fig.5.21 and Fig.5.22 are the experimental results obtained using internal model disturbance observer compensated PI control with the same reference as for PI control. Compared with the results obtained by traditional disturbance observer compensated PI control, the error of position tracking with compensation given by internal model disturbance observer is suppressed even further. In addition, Fig.5.23 shows the estimated lumped input disturbance given by the internal model disturbance observer in experiment.

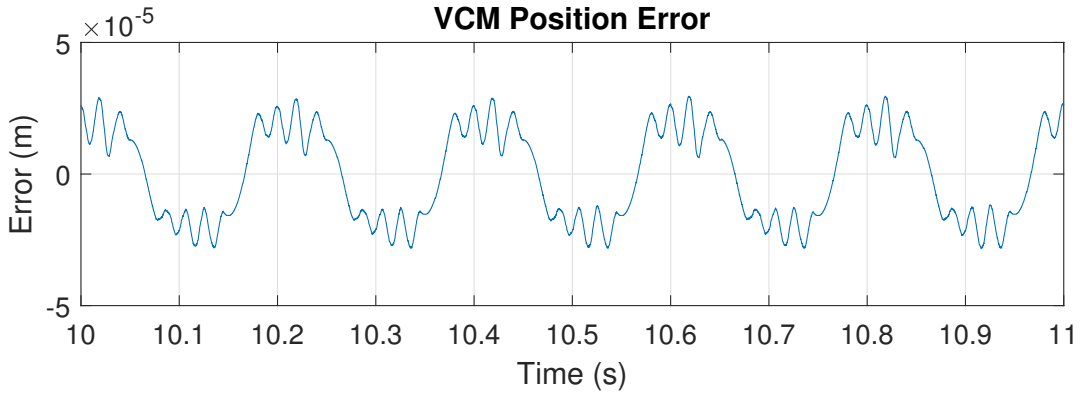

Figure 5.17: Experimental error of position reference tracking of VCM using PI control with reference at $5Hz$ and normal force of $6N$

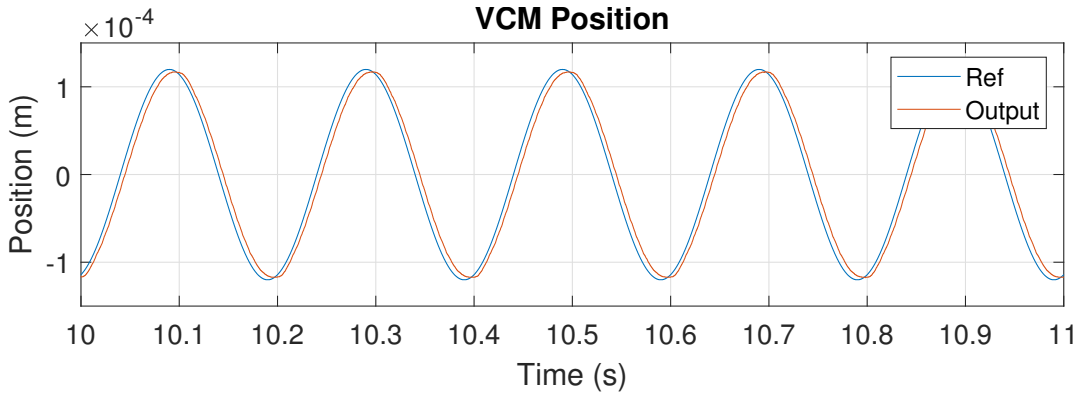

Figure 5.18: Experimental result of position reference tracking of VCM using traditional disturbance observer compensated PI control with reference at $5Hz$ and normal force of $6N$

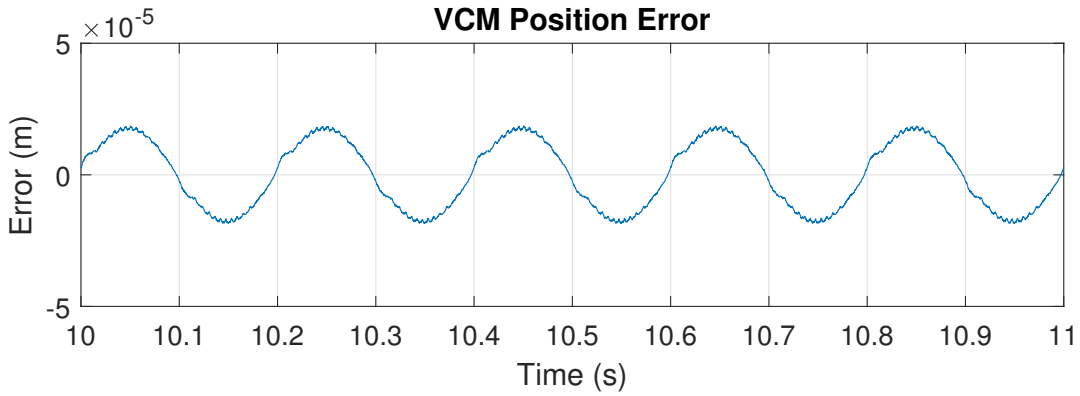

Figure 5.19: Experimental error of position reference tracking of VCM using traditional disturbance observer compensated PI control with reference at $5Hz$ and normal force of $6N$

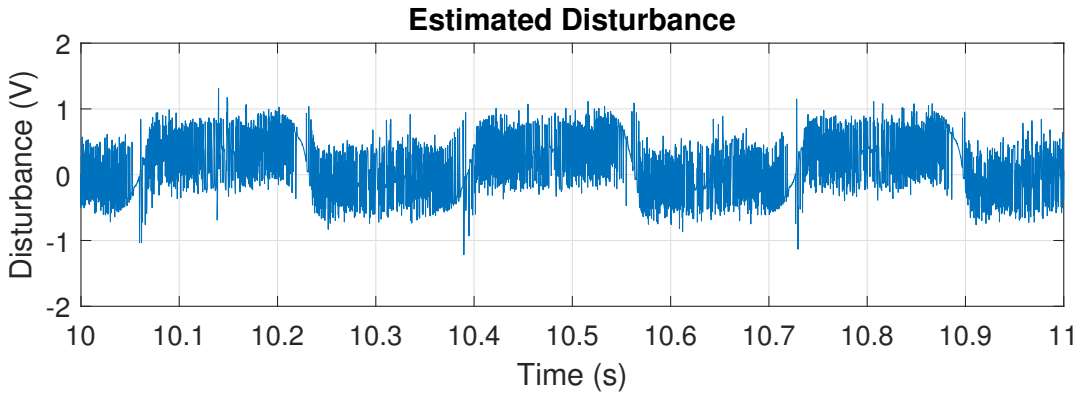

Figure 5.20: Estimated lumped input disturbance obtained using traditional disturbance observer in position reference tracking experiment with reference at $5Hz$ and normal force of $6N$

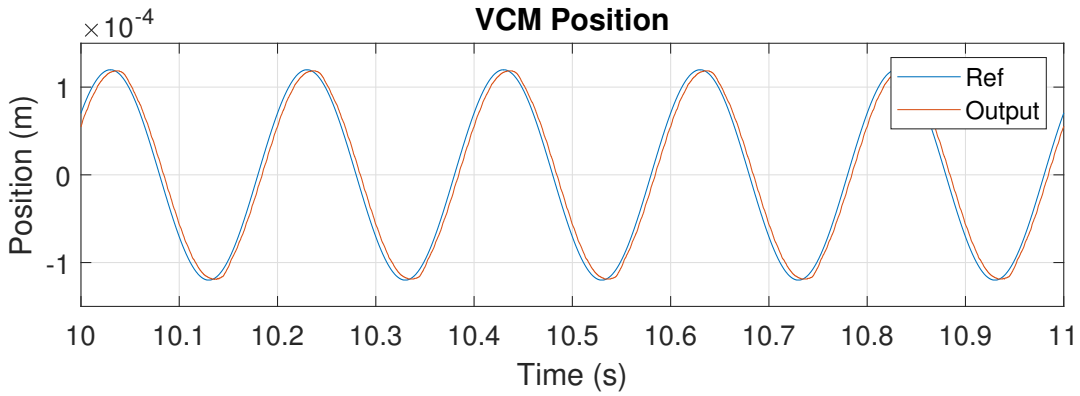

Figure 5.21: Experimental result of position reference tracking of VCM using internal model disturbance observer compensated PI control with reference at $5Hz$ and normal force of $6N$

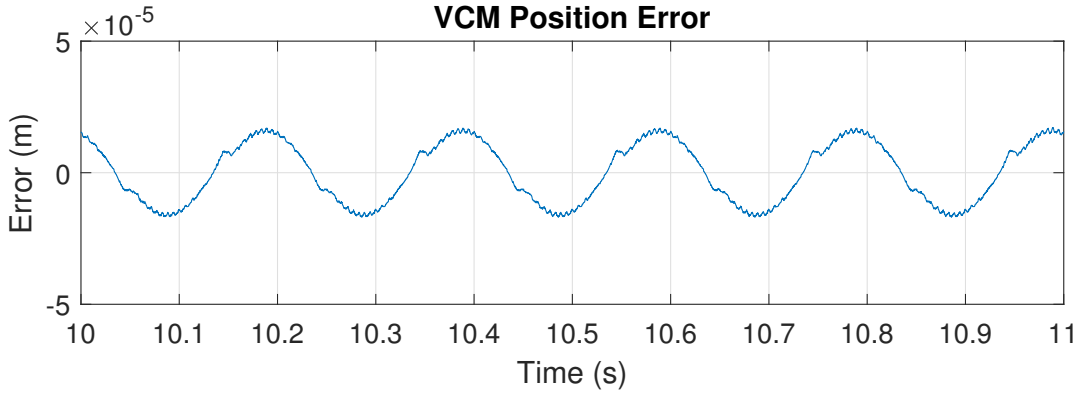

Figure 5.22: Experimental error of position reference tracking of VCM using internal model disturbance observer compensated PI control with reference at $5Hz$ and normal force of $6N$

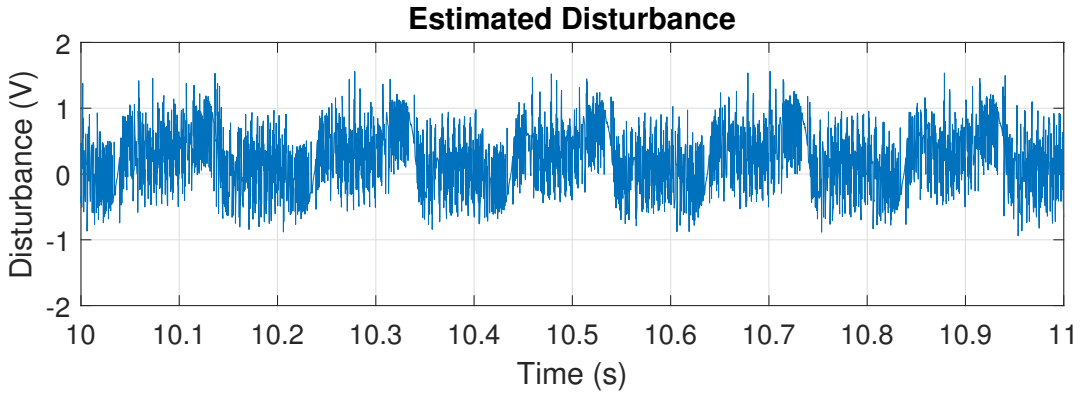

Figure 5.23: Estimated lumped input disturbance obtained using internal model disturbance observer in position reference tracking experiment with reference at $5Hz$ and normal force of $6N$

Fig.5.24 and Fig.5.25 are the experimental results obtained using PI control to track a sinusoidal wave of the frequency of $7Hz$. The normal force in this case is set as $6N$. The desired amplitude in this case is set as $120\mu m$. It can be found that the output position of VCM is distorted due to disturbance. Fig.5.26 and Fig.5.27 are the experimental results obtained using traditional disturbance observer compensated PI control with the same reference as for PI control. Compared with the results obtained by PI control, the error of position tracking with compensation given by disturbance observer is suppressed significantly. In addition, Fig.5.28 shows the estimated lumped input disturbance given by the traditional disturbance observer in experiment. The fundamental period of disturbance is the same as that of the reference position signal, which is in agreement with the results of simulation. Fig.5.29 and Fig.5.30 are the experimental results obtained using internal model disturbance observer compensated PI control with the same reference as for PI control. Compared with the results obtained by traditional disturbance observer compensated PI control, the error of position tracking with compensation given by internal model disturbance observer is suppressed even further. In addition, Fig.5.31 shows the estimated lumped input disturbance given by the internal model disturbance observer in experiment.

Fig.5.32 and Fig.5.33 are the experimental results obtained using PI control to

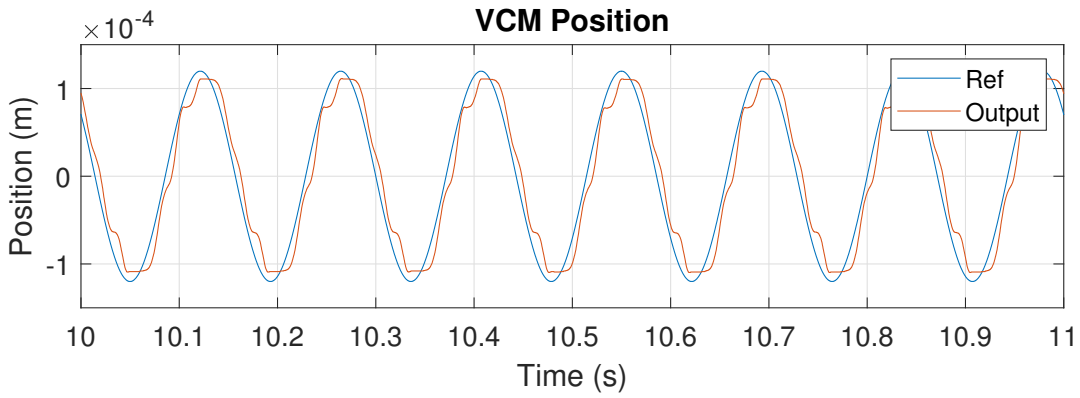

Figure 5.24: Experimental result of position reference tracking of VCM using PI control with reference at $7Hz$ and normal force of $6N$

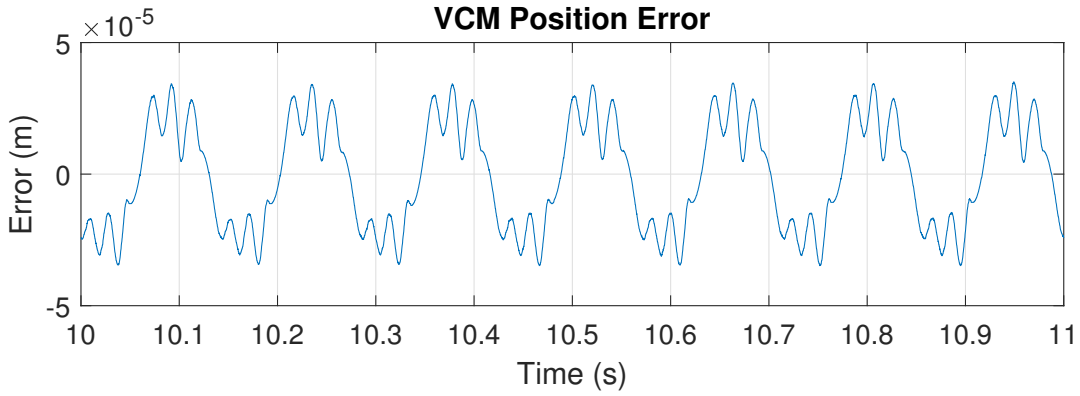

Figure 5.25: Experimental error of position reference tracking of VCM using PI control with reference at $7Hz$ and normal force of $6N$

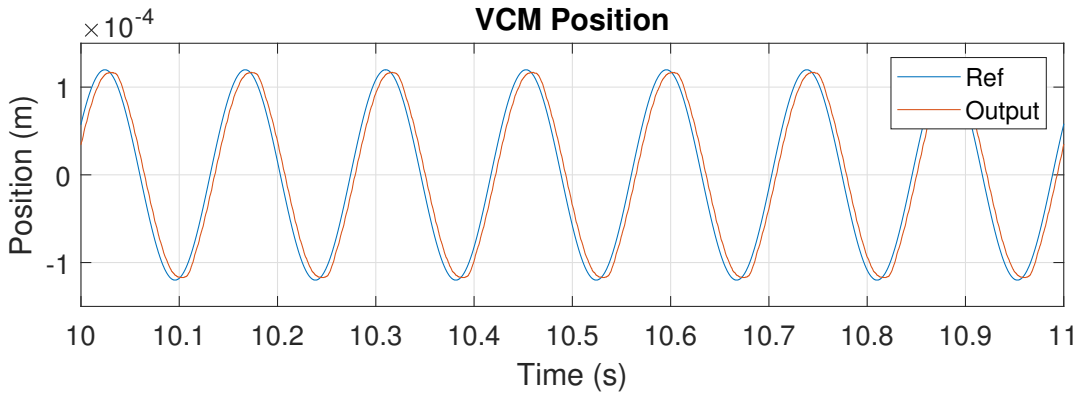

Figure 5.26: Experimental result of position reference tracking of VCM using traditional disturbance observer compensated PI control with reference at $7Hz$ and normal force of $6N$

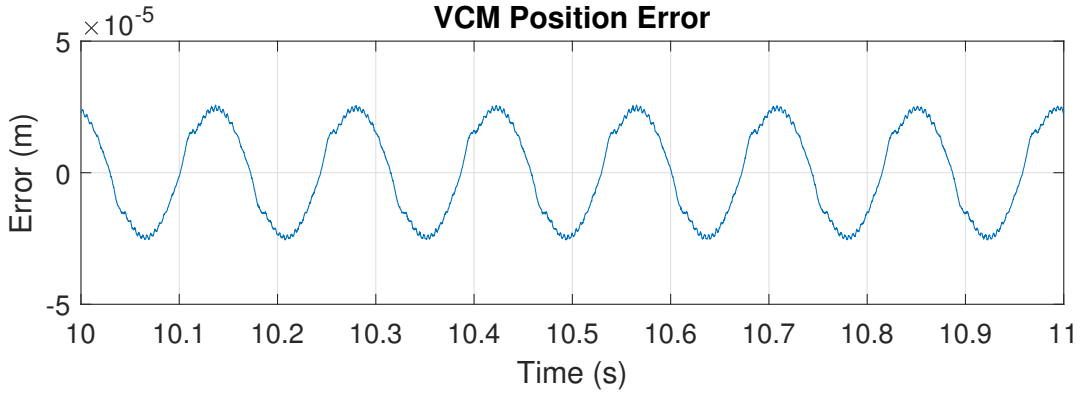

Figure 5.27: Experimental error of position reference tracking of VCM using traditional disturbance observer compensated PI control with reference at $7Hz$ and normal force of $6N$

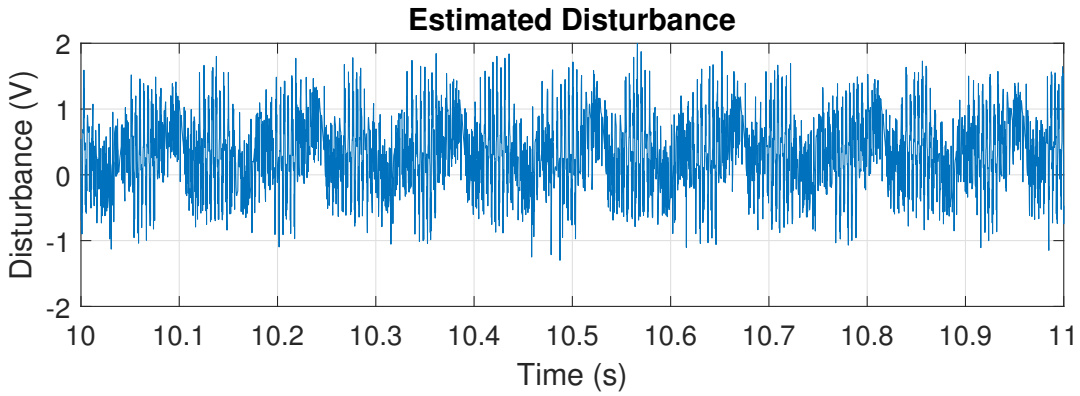

Figure 5.28: Estimated lumped input disturbance obtained using traditional disturbance observer in position reference tracking experiment with reference at $7Hz$ and normal force of $6N$

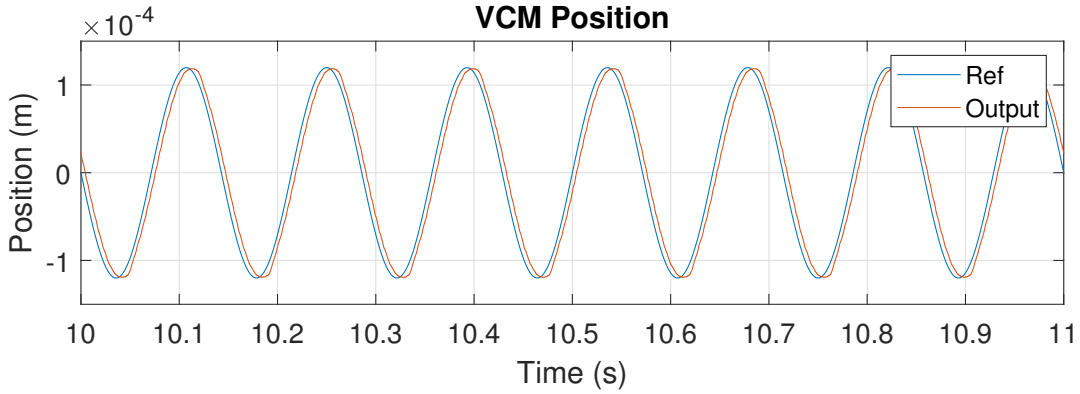

Figure 5.29: Experimental result of position reference tracking of VCM using internal model disturbance observer compensated PI control with reference at $7Hz$ and normal force of $6N$

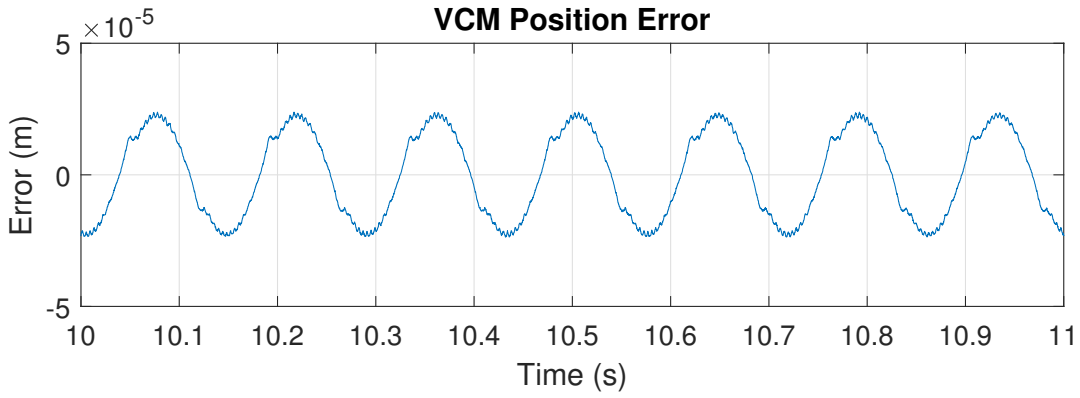

Figure 5.30: Experimental error of position reference tracking of VCM using internal model disturbance observer compensated PI control with reference at $7Hz$ and normal force of $6N$

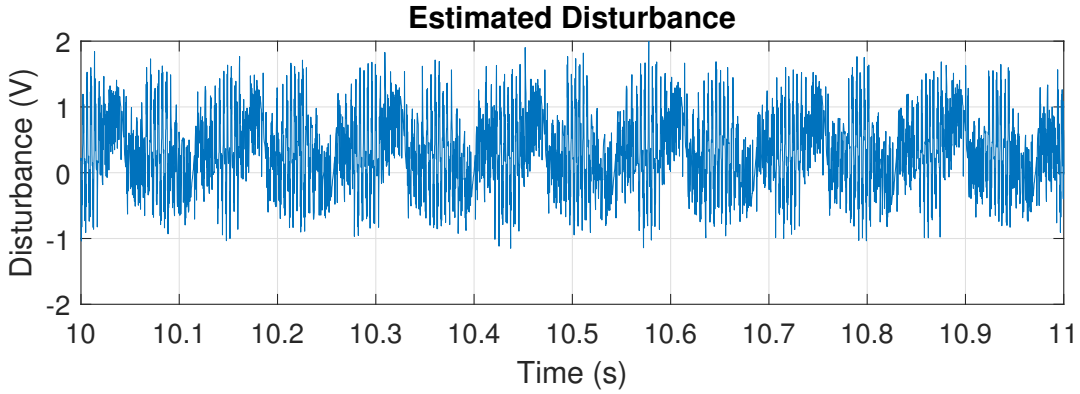

Figure 5.31: Estimated lumped input disturbance obtained using internal model disturbance observer in position reference tracking experiment with reference at $7Hz$ and normal force of $6N$

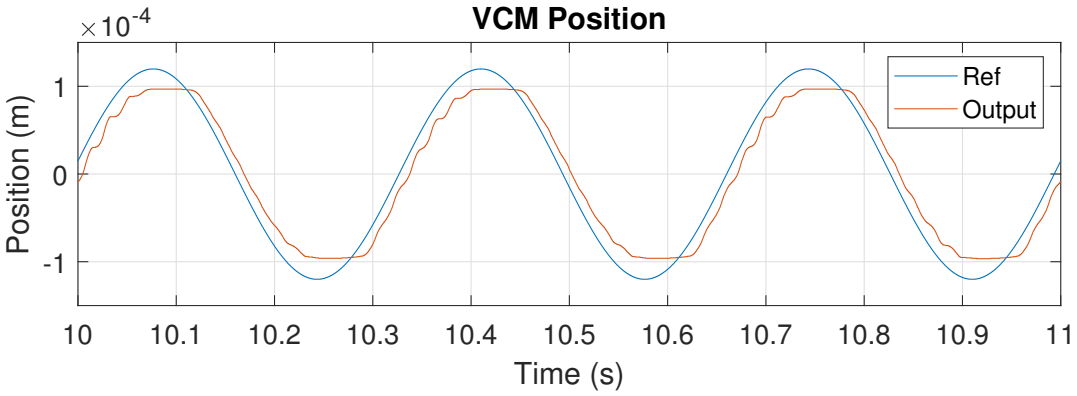

Figure 5.32: Experimental result of position reference tracking of VCM using PI control with reference at $3Hz$ and normal force of $10N$

track a sinusoidal wave of the frequency of $3Hz$. The normal force in this case is set as $10N$. The desired amplitude in this case is set as $120\mu m$. It can be found that the output position of VCM is distorted due to disturbance. Fig.5.34 and Fig.5.35 are the experimental results obtained using traditional disturbance observer compensated PI control with the same reference as for PI control. Compared with the results obtained by PI control, the error of position tracking with compensation given by disturbance observer is suppressed significantly. In addition, Fig.5.36 shows the estimated lumped input disturbance given by the traditional disturbance observer in experiment. The fundamental period of disturbance is the same as that of the reference position signal, which is in agreement with the results of simulation. Fig.5.37 and Fig.5.38 are the experimental results obtained using internal model disturbance observer compensated PI control with the same reference as for PI control. Compared with the results obtained by traditional disturbance observer compensated PI control, the error of position tracking with compensation given by internal model disturbance observer is suppressed even further. In addition, Fig.5.39 shows the estimated lumped input disturbance given by the internal model disturbance observer in experiment.

Fig.5.40 and Fig.5.41 are the experimental results obtained using PI control to track a sinusoidal wave of the frequency of $5Hz$. The normal force in this case is set as $10N$. The desired amplitude in this case is set as $120\mu m$. It can be found that

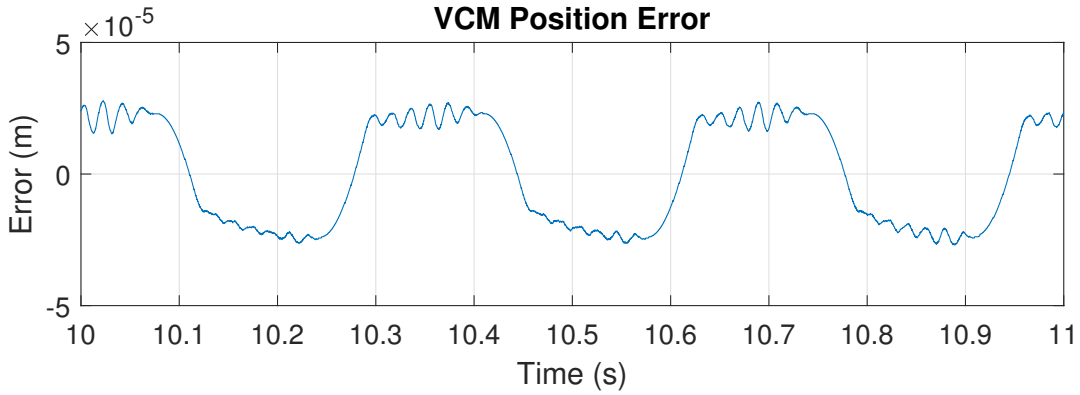

Figure 5.33: Experimental error of position reference tracking of VCM using PI control with reference at $3Hz$ and normal force of $10N$

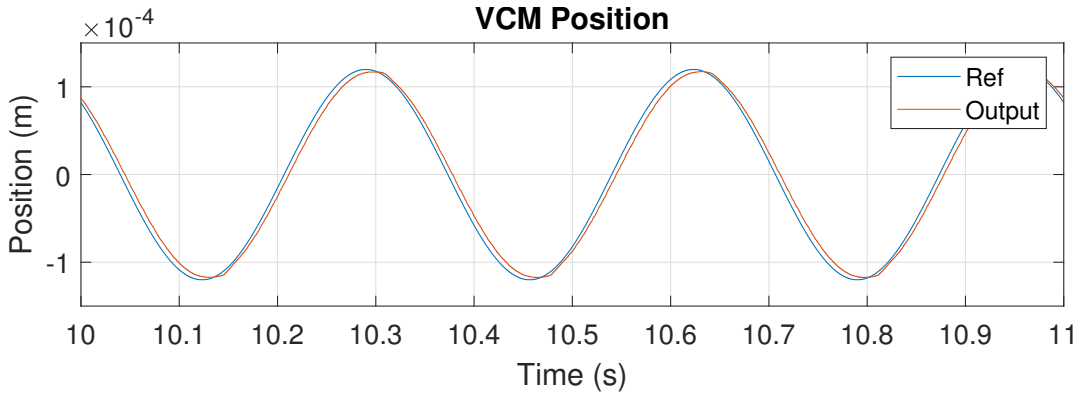

Figure 5.34: Experimental result of position reference tracking of VCM using traditional disturbance observer compensated PI control with reference at $3Hz$ and normal force of $10N$

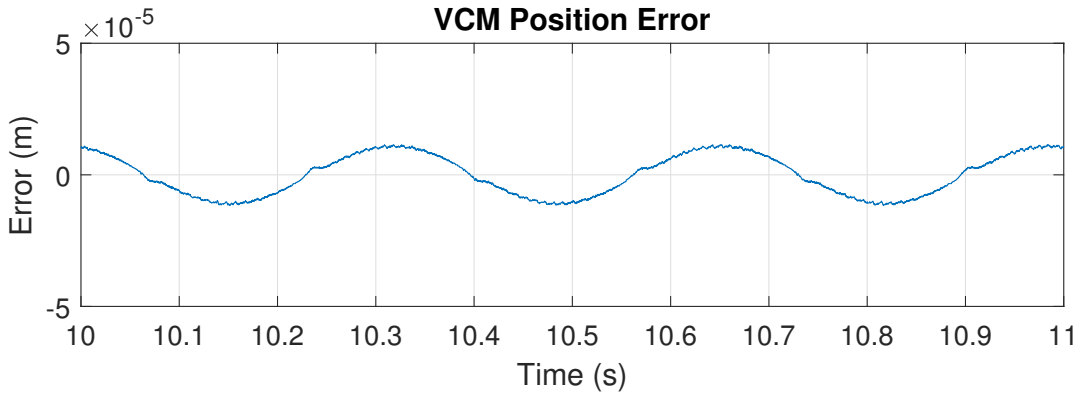

Figure 5.35: Experimental error of position reference tracking of VCM using traditional disturbance observer compensated PI control with reference at $3Hz$ and normal force of $10N$

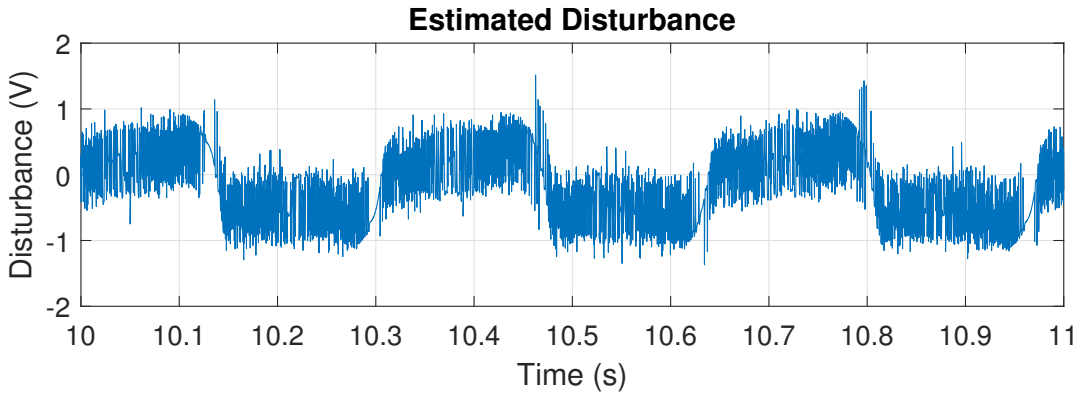

Figure 5.36: Estimated lumped input disturbance obtained using traditional disturbance observer in position reference tracking experiment with reference at $3Hz$ and normal force of $10N$

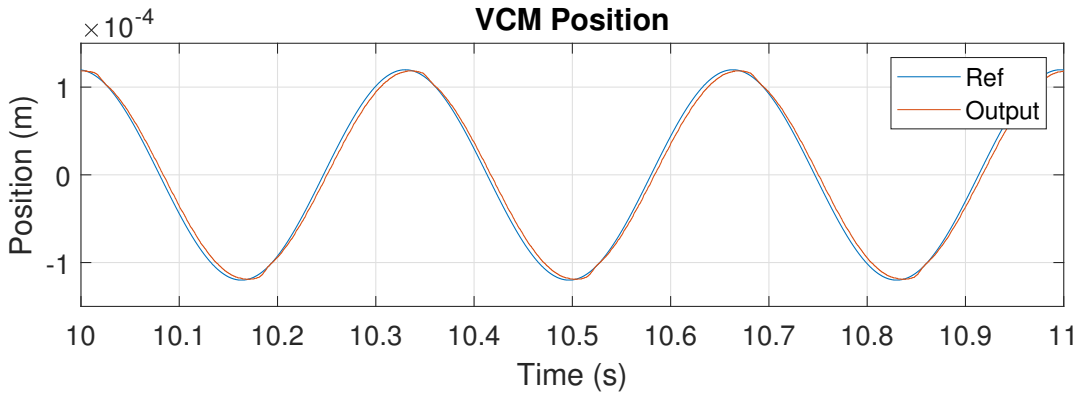

Figure 5.37: Experimental result of position reference tracking of VCM using internal model disturbance observer compensated PI control with reference at $3Hz$ and normal force of $10N$

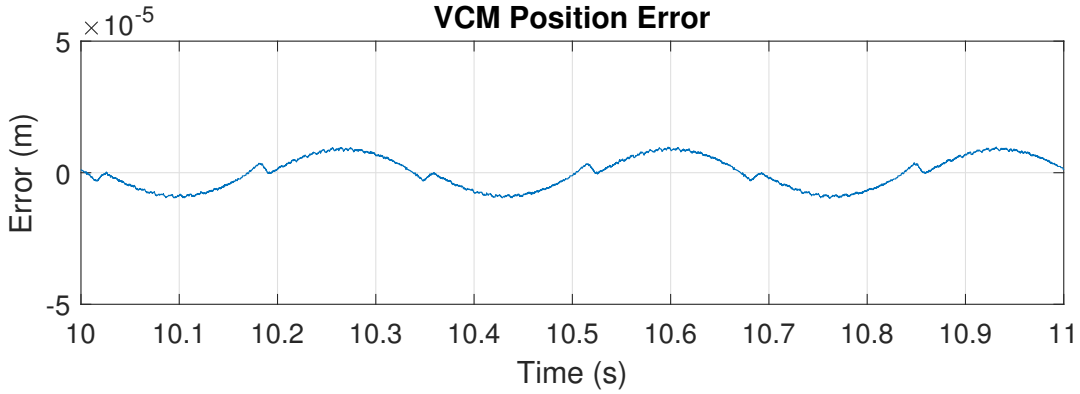

Figure 5.38: Experimental error of position reference tracking of VCM using internal model disturbance observer compensated PI control with reference at $3Hz$ and normal force of $10N$

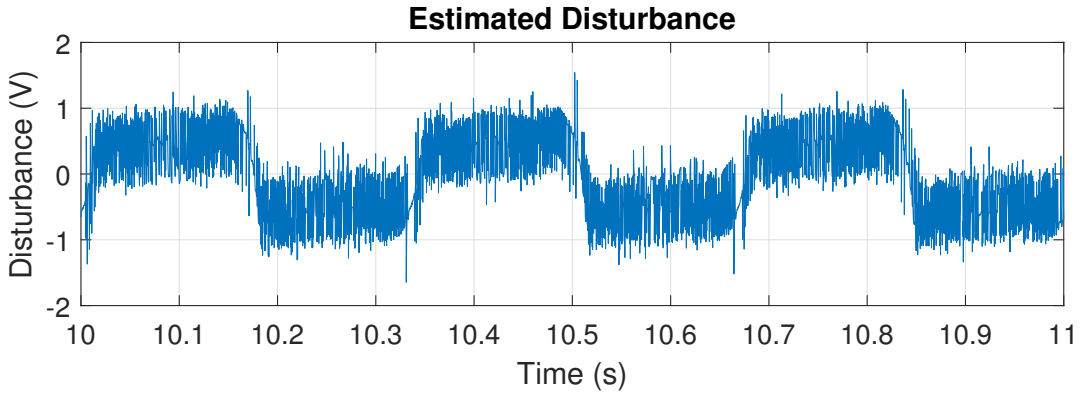

Figure 5.39: Estimated lumped input disturbance obtained using internal model disturbance observer in position reference tracking experiment with reference at $3Hz$ and normal force of $10N$

the output position of VCM is distorted due to disturbance. Fig.5.42 and Fig.5.43 are the experimental results obtained using traditional disturbance observer compensated PI control with the same reference as for PI control. Compared with the results obtained by PI control, the error of position tracking with compensation given by disturbance observer is suppressed significantly. In addition, Fig.5.44 shows the estimated lumped input disturbance given by the traditional disturbance observer in experiment. The fundamental period of disturbance is the same as that of the reference position signal, which is in agreement with the results of simulation. Fig.5.45 and Fig.5.46 are the experimental results obtained using internal model disturbance observer compensated PI control with the same reference as for PI control. Compared with the results obtained by traditional disturbance observer compensated PI control, the error of position tracking with compensation given by internal model disturbance observer is suppressed even further. In addition, Fig.5.47 shows the estimated lumped input disturbance given by the internal model disturbance observer in experiment.

Fig.5.48 and Fig.5.49 are the experimental results obtained using PI control to track a sinusoidal wave of the frequency of $7Hz$. The normal force in this case is set as $10N$. The desired amplitude in this case is set as $120\mu m$. It can be found that the output position of VCM is distorted due to disturbance. Fig.5.50 and Fig.5.51

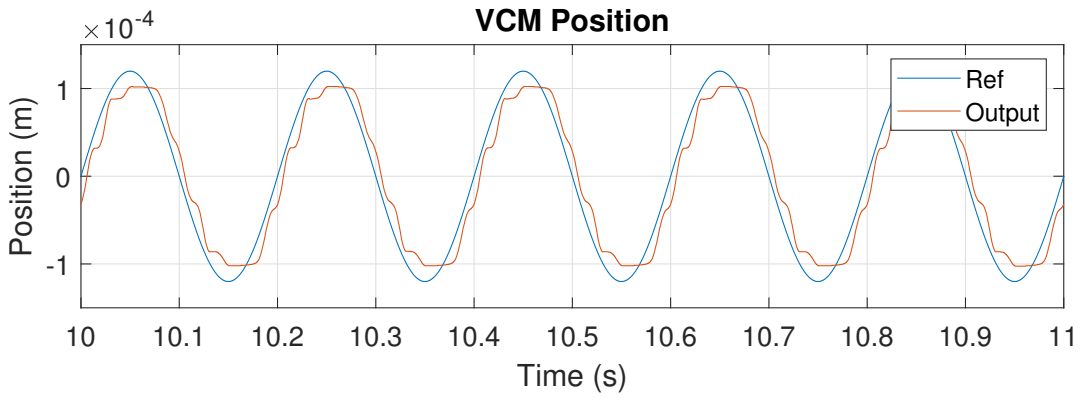

Figure 5.40: Experimental result of position reference tracking of VCM using PI control with reference at $5Hz$ and normal force of $10N$

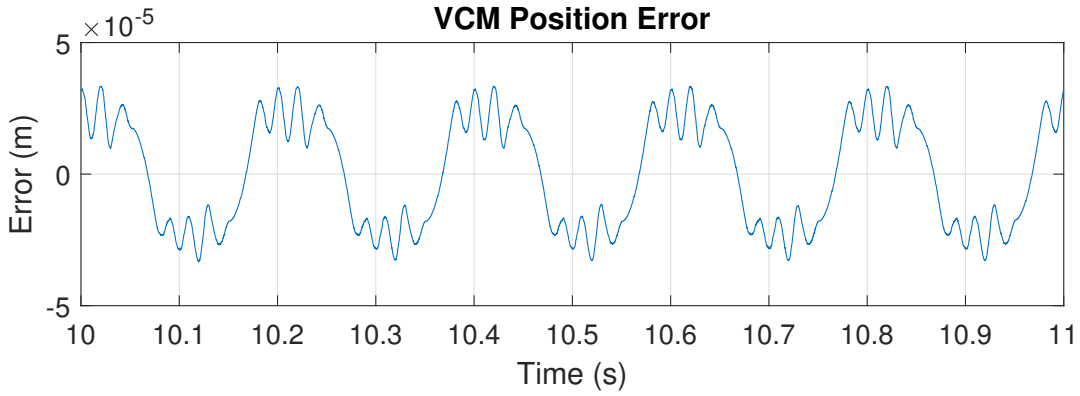

Figure 5.41: Experimental error of position reference tracking of VCM using PI control with reference at $5Hz$ and normal force of $10N$

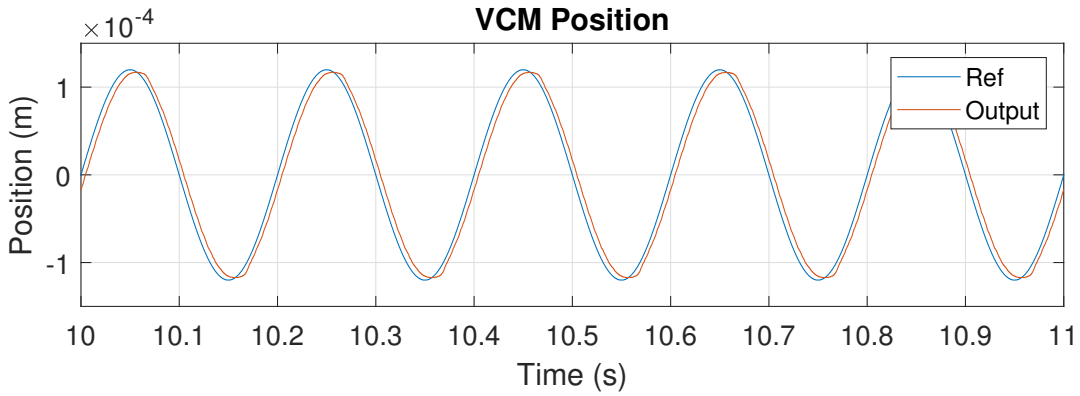

Figure 5.42: Experimental result of position reference tracking of VCM using traditional disturbance observer compensated PI control with reference at $5Hz$ and normal force of $10N$

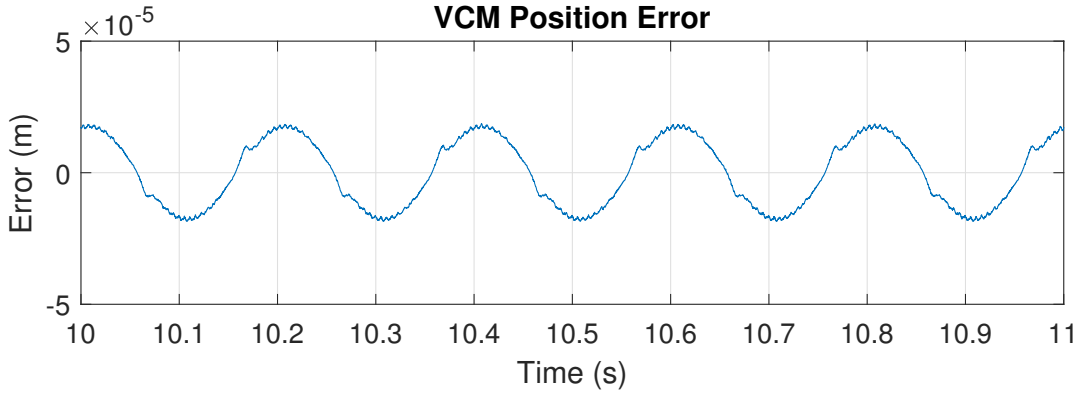

Figure 5.43: Experimental error of position reference tracking of VCM using traditional disturbance observer compensated PI control with reference at $5Hz$ and normal force of $10N$

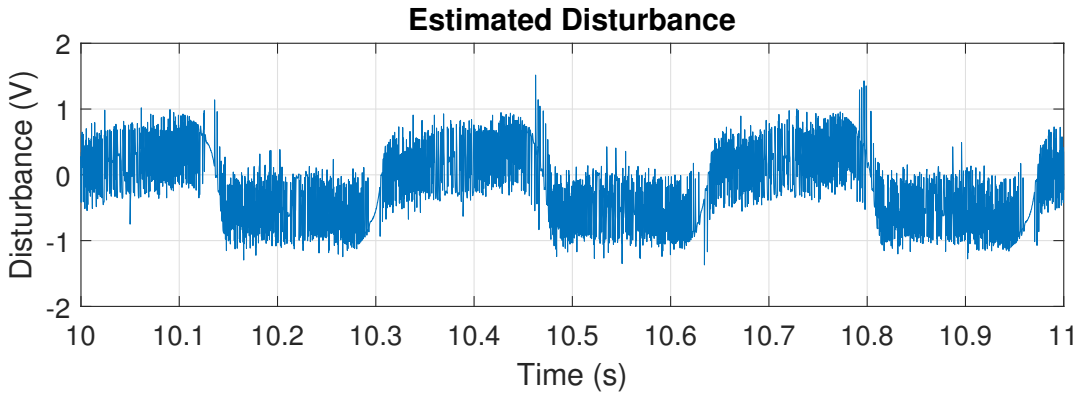

Figure 5.44: Estimated lumped input disturbance obtained using traditional disturbance observer in position reference tracking experiment with reference at $5Hz$ and normal force of $10N$

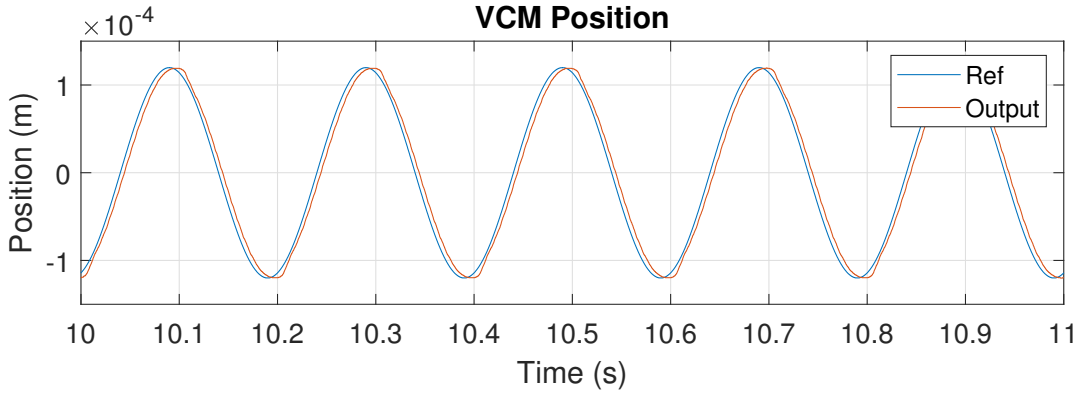

Figure 5.45: Experimental result of position reference tracking of VCM using internal model disturbance observer compensated PI control with reference at $5Hz$ and normal force of $10N$

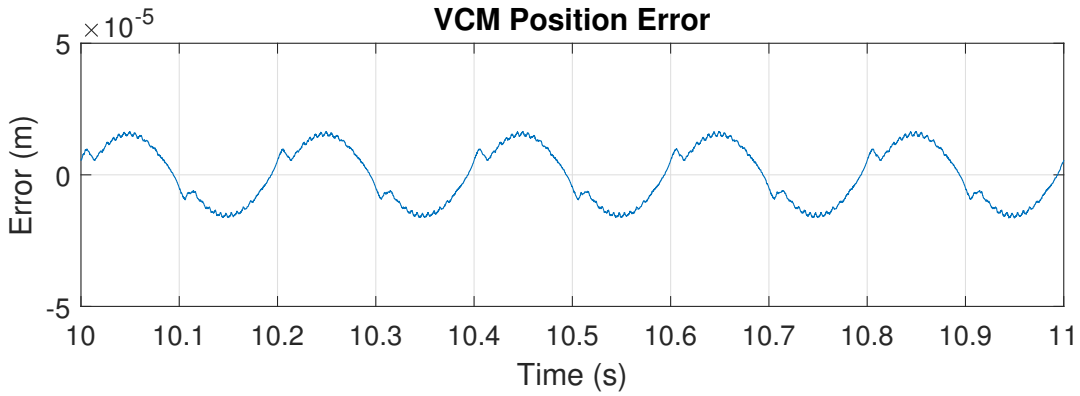

Figure 5.46: Experimental error of position reference tracking of VCM using internal model disturbance observer compensated PI control with reference at $5Hz$ and normal force of $10N$

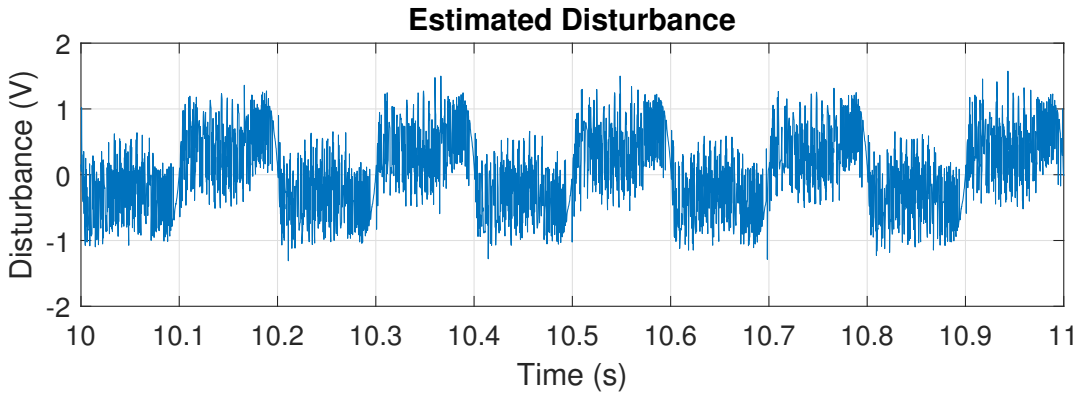

Figure 5.47: Estimated lumped input disturbance obtained using internal model disturbance observer in position reference tracking experiment with reference at $5Hz$ and normal force of $10N$

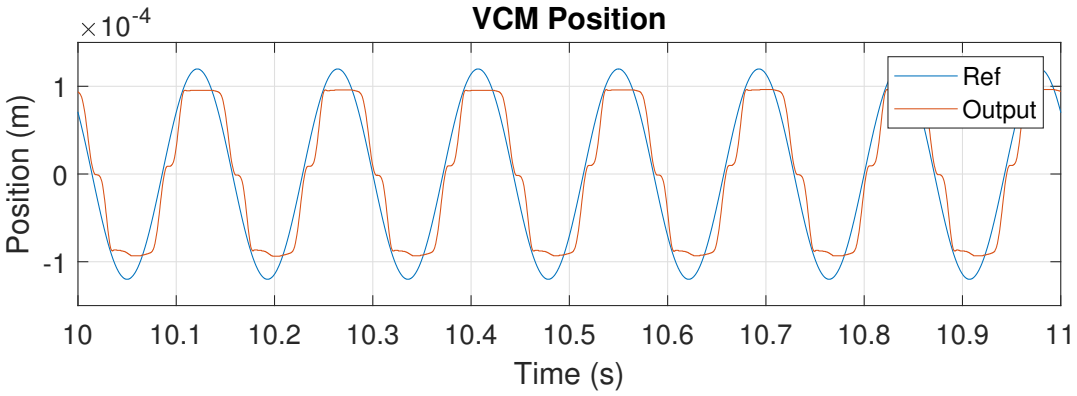

Figure 5.48: Experimental result of position reference tracking of VCM using PI control with reference at $7Hz$ and normal force of $10N$

are the experimental results obtained using traditional disturbance observer compensated PI control with the same reference as for PI control. Compared with the results obtained by PI control, the error of position tracking with compensation given by disturbance observer is suppressed significantly. In addition, Fig.5.52 shows the estimated lumped input disturbance given by the traditional disturbance observer in experiment. The fundamental period of disturbance is the same as that of the reference position signal, which is in agreement with the results of simulation. Fig.5.53 and Fig.5.54 are the experimental results obtained using internal model disturbance observer compensated PI control with the same reference as for PI control. Compared with the results obtained by traditional disturbance observer compensated PI control, the error of position tracking with compensation given by internal model disturbance observer is suppressed even further. In addition, Fig.5.55 shows the estimated lumped input disturbance given by the internal model disturbance observer in experiment.

Fig.5.56 and Fig.5.57 are the relative errors in percentage given by different control methods under different experimental conditions. The internal model disturbance observer compensated PI controller outperforms the others in terms of relative error suppression. In addition, it can be found that for any control method, the relative error will increase with increasing frequency of reference signal.

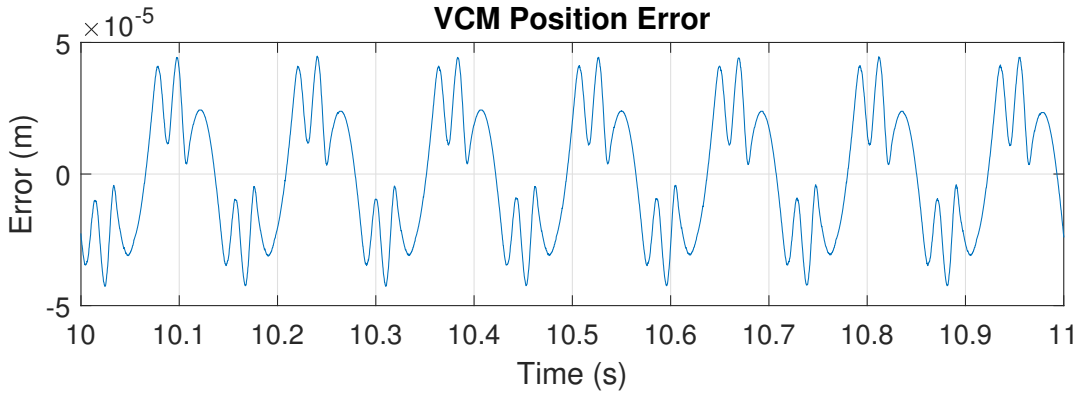

Figure 5.49: Experimental error of position reference tracking of VCM using PI control with reference at $7Hz$ and normal force of $10N$

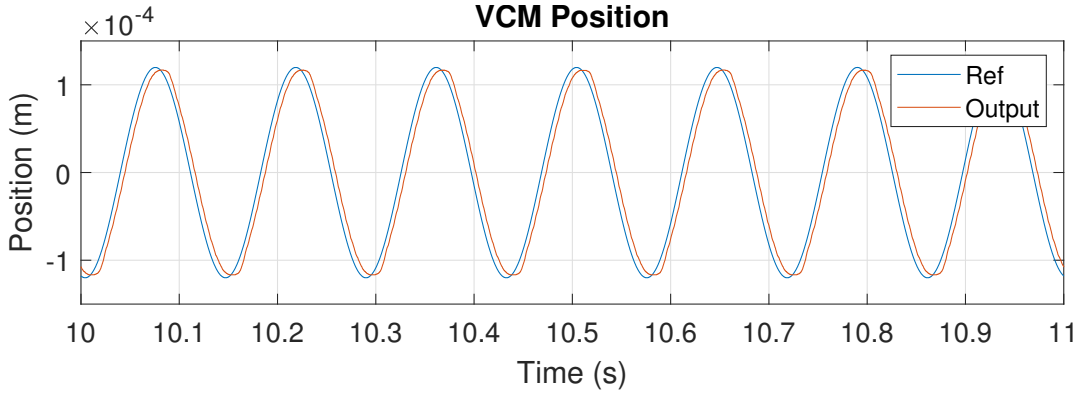

Figure 5.50: Experimental result of position reference tracking of VCM using traditional disturbance observer compensated PI control with reference at $7Hz$ and normal force of $10N$

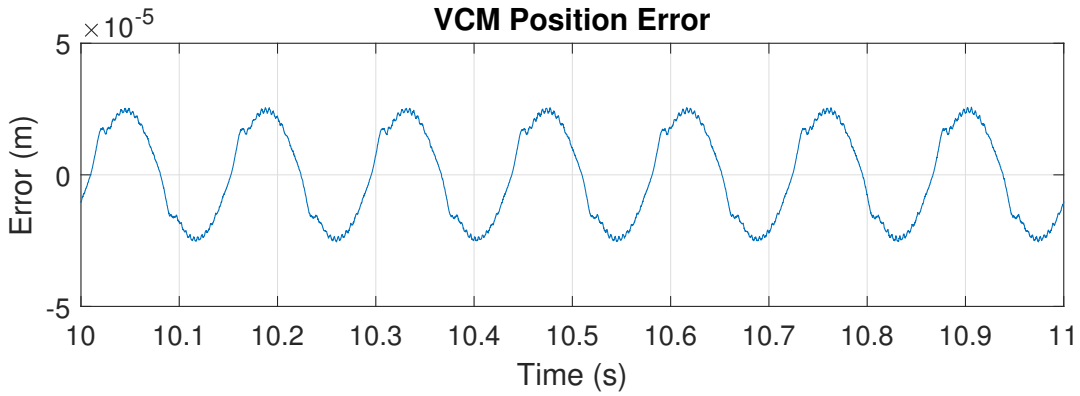

Figure 5.51: Experimental error of position reference tracking of VCM using traditional disturbance observer compensated PI control with reference at $7Hz$ and normal force of $10N$

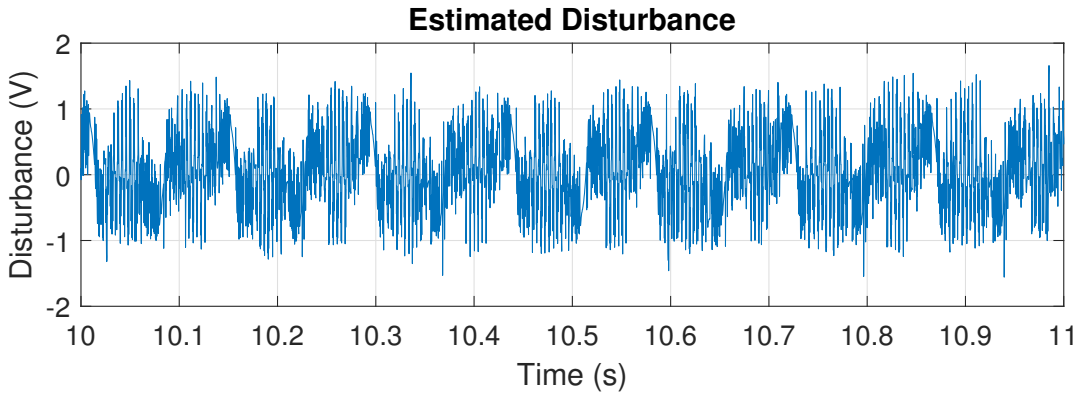

Figure 5.52: Estimated lumped input disturbance obtained using traditional disturbance observer in position reference tracking experiment with reference at $7Hz$ and normal force of $10N$

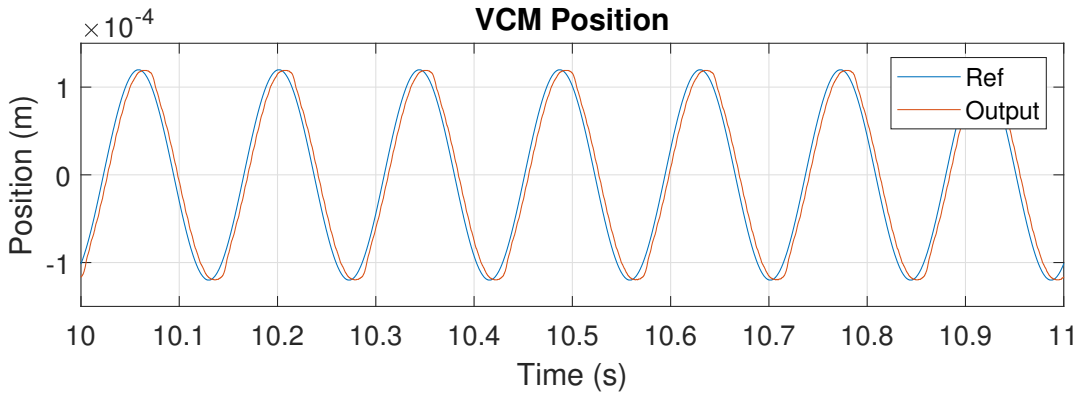

Figure 5.53: Experimental result of position reference tracking of VCM using internal model disturbance observer compensated PI control with reference at $7Hz$ and normal force of $10N$

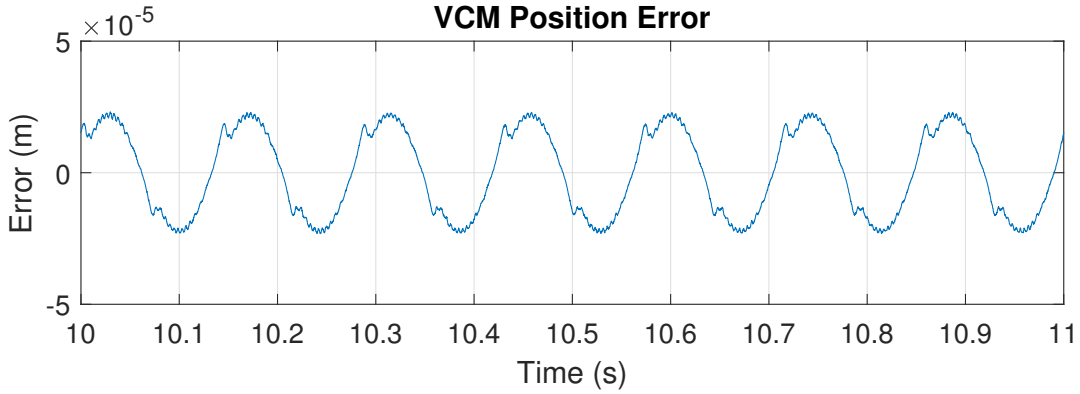

Figure 5.54: Experimental error of position reference tracking of VCM using internal model disturbance observer compensated PI control with reference at $7Hz$ and normal force of $10N$

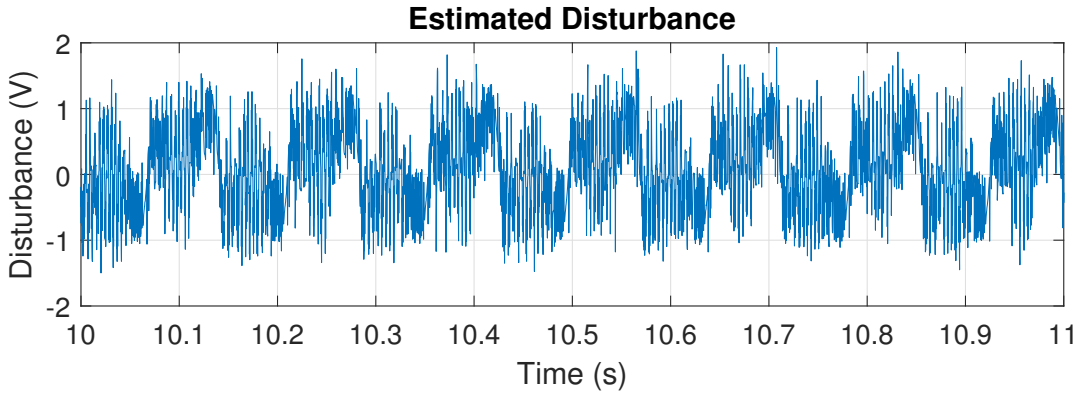

Figure 5.55: Estimated lumped input disturbance obtained using internal model disturbance observer in position reference tracking experiment with reference at $7Hz$ and normal force of $10N$

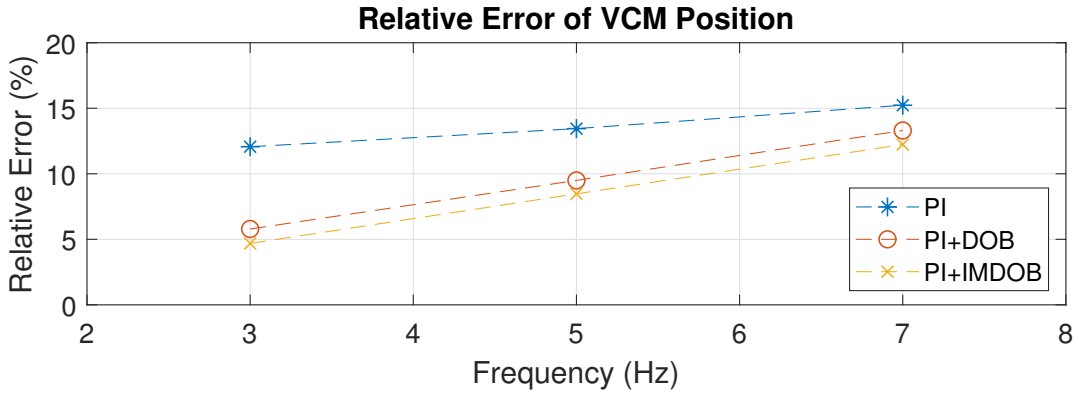

Figure 5.56: Relative errors given by different control methods in position reference tracking experiments with normal force of $6N$

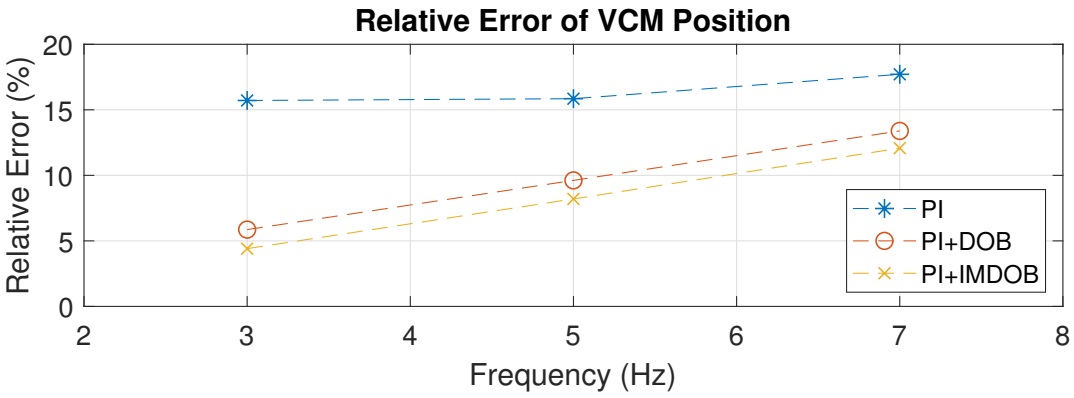

Figure 5.57: Relative errors given by different control methods in position reference tracking experiments with normal force of $10N$

5.6 Conclusion

The frictional load that dominates the external disturbances to the VCM on HFRR is periodic in a reciprocating motion. By exploiting such periodicity attribute, internal model disturbance observer can be constructed by embedding the generating model of frictional load projected to the input of the plant. Compared with traditional disturbance observer with no explicit assumption on the characteristics of the input disturbance in the frequency domain, the internal model disturbance observer can achieve a higher tracking accuracy. Both simulations and experiments show that the traditional PI control with compensation provided by internal model disturbance observer outperforms that with compensation provided by traditional disturbance observer in terms of minimising the tracking error in reciprocating motions.

Chapter 6

Conclusions and Future Work

This chapter has summarised the obtained results of this thesis and contributions. The suggestions for future investigations are also listed.

6.1 Conclusions

This thesis is aimed to propose the motion control methods for VCM on HFRR in Pin-on-disk reciprocating tribotest in order to solve the problem of unsatisfactory tracking accuracy due to frictional load. In this thesis, the following works are presented:

- The model of HFRR is constructed by combining the model of VCM and that of friction. A DSP-based experimental platform has been built and shown in detail. The programs for both PC and DSP are developed through automatic C code generation for embedded processors function in MATLAB/SIMULINK environment.

- Direct amplitude control is proposed to deal with the amplitude keeping problem of HFRR subjects to frictional load, which takes the error of the amplitude of the position signal as the performance index rather than tracking error. It includes an STFT based amplitude regulator module and an offset compensator. The analysis shows that the error of amplitude of position signal of the closed loop system converges to zero by applying the proposed control. The

proposed control method is verified through experiments. It outperforms conventional control in terms of amplitude keeping and harmonics suppression.

- Acceleration based control method is applied to VCM on HFRR, where the design of a task controller that synthesise the desired system acceleration and the construction of a disturbance compensation module that estimate and compensate for the input disturbance are involved. By assuming the relatively slow variation of frictional force and matching condition, the frictional force that distorts the output signal can be compensated through the reduced order disturbance observer at the input of the plant. Both simulation and experiment results show that acceleration based control outperforms conventional control in terms of tracking error and phase lagging in the case of tracking sinusoidal reference.

- The frictional load that dominates the external disturbances to the VCM on HFRR is periodic in reciprocating motions. By exploiting such periodicity attribute, internal model disturbance observer can be constructed by embedding the generating model of frictional load projected to the input of the plant. Compared with traditional disturbance observer with no explicit assumption on the characteristics of the input disturbance in the frequency domain, the internal model disturbance observer can achieve a higher tracking accuracy. In both simulation and experiments, the internal model disturbance observer based control outperforms traditional frequency domain disturbance observer based control in terms of tracking accuracy.

- The developed direct amplitude controller and acceleration based controller have been successfully deployed to the company product: Sodium-potassium alloy fretting wear tribotester, which is used to study the principle of fretting wear within the coolant pump of the nuclear reactor. As the key component VCM on HFRR is also applied to electromagnetic exciter and positioning stage, the developed control methods are possible to be used in such applications. In addition, the research conducted so far does not examine schemes on different combinations between feedback controllers and feedforward dis-

turbance compensators. For example, the combination of acceleration based control and internal model disturbance observer.

6.2 Future Work

The possible future work are listed based on the following ideas:

- The model of HFRR in this thesis introduces LuGre friction model with time-invariant parameters. However, the variation of the friction coefficient can be observed in experiments. The time-varying attribute of model parameters can be considered in future work in order to reflect the dynamics of HFRR more precisely.

- The direct amplitude control method does not take the disturbance explicitly into consideration when designing the algorithm. Disturbance attenuation techniques can be combined with the proposed method to further improve the performance of direct amplitude control in future work.

- The acceleration based control method applies the reduced order disturbance observer with the assumption that the rate of change of the input disturbance is relatively slow. It is worth studying different designs of disturbance observer within the framework of acceleration based control, as the reduced order disturbance observer, in this case, does not fully investigate the characteristics of the disturbance.

- The internal model disturbance observer only takes the fundamental frequency of friction into consideration for simplicity. It is worth studying the impact of including resonant terms corresponding to harmonics in the future study on the design of internal model disturbance observer.

References

[1] I. Hutchings and P. Shipway. *Tribology Friction and Wear of Engineering Materials*. Butterworth-Heinemann, 50 Hampshire Street, 5th Floor, Cambridge, MA 02139, United States, 2017.

[2] Bharat Bhushan. *Modern Tribology Handbook*, volume 1. CRC pree LLC, USA, 1 edition, December 2000.

[3] K. G. Budinski. *Guide to Friction, Wear and Erosion Testing*. ASTM International, 100 Barr Harbor Drive, PO Box C700, West Conshohocken, 2007.

[4] Bharat Bhushan. *Introduction to Tribology*. A John Wiley & Sons, Ltd., John Wiley & Sons Ltd, The Atrium, Southern Gate, Chichester, West Sussex, PO19 8SQ, United Kingdom, 2013.

[5] INFINEUM INTERNATIONAL. *Testing the test*, 2013.

[6] Kouseki Sugiyama, Masataka Kajiwara, Masahiro Fukumoto, Makihiko Mori, Shinichi Goto, and Tomoko Watanabe. Lubricity of liquefied gas assessment of multi-pressure/temperature high-frequency reciprocating rig (mpt-hfrr) -dme fuel for diesel. In *SAE Technical Paper*. SAE International, 06 2004.

[7] *Diesel fuel-Assessment of lubricity using the high frequency reciprocating rig (HFRR)*. Number 12156-1:2016. 2016.

[8] PCS Instruments. *HFRR High Frequency Reciprocating Rig (Brochure)*, 2019. v1.

[9] S. Wu, Z. Jiao, L. Yan, R. Zhang, J. Yu, and C. Chen. Development of a direct-drive servo valve with high-frequency voice coil motor and advanced digital controller. *IEEE/ASME Transactions on Mechatronics*, 19(3):932–942, June 2014.

[10] E. Csencsics, M. Thier, R. Hainisch, and G. Schitter. System and control design of a voice coil actuated mechanically decoupling two-body vibration isolation system. *IEEE/ASME Transactions on Mechatronics*, 23(1):321–330, Feb 2018.

[11] E. Asadi, A. Khajepour, and M. B. Khamesee. A new low-profile electromagnetic-pneumatic actuator for high-bandwidth applications. *IEEE/ASME Transactions on Mechatronics*, 23(5):2207–2217, Oct 2018.

[12] H2W Technologies. *Understanding the Basics of a Voice Coil Actuator*, 2018.

[13] A. Maddahi, N. Sepehri, and W. Kinsner. Fractional-order control of hydraulically powered actuators: Controller design and experimental validation. *IEEE/ASME Transactions on Mechatronics*, 24(2):796–807, April 2019.

[14] X. Hu, L. Cao, Y. Luo, A. Chen, E. Zhang, and W. J. Zhang. A novel methodology for comprehensive modeling of the kinetic behavior of steerable catheters. *IEEE/ASME Transactions on Mechatronics*, 24(4):1785–1797, Aug 2019.

[15] H. Yu, T. Chen, and C. Liu. Adaptive fuzzy logic proportional-integral-derivative control for a miniature autofocus voice coil motor actuator with retaining force. *IEEE Transactions on Magnetics*, 50(11):1–4, Nov 2014.

[16] J. . Seok and S. . Kim. Vcm controller design with enhanced disturbance decoupling for precise automated manufacturing processes. *IET Electric Power Applications*, 6(8):575–582, Sep. 2012.

[17] H. Guo, D. Wang, and J. Xu. Research on a high-frequency response direct drive valve system based on voice coil motor. *IEEE Transactions on Power Electronics*, 28(5):2483–2492, May 2013.

[18] Y. Gao. Active disturbance-rejection control of voice coil motor based on rbf neural network. In *2011 International Conference on Consumer Electronics, Communications and Networks (CECNet)*, pages 3895–3898, April 2011.

[19] G. Guo and D. Wu. Modified dual-stage controller for dealing with secondary-stage actuator saturation. *IEEE Transactions on Magnetics*, 39(6):3587–3592, Nov 2003.

[20] G. Herrmann, M. C. Turner, and I. Postlethwaite and. Practical implementation of a novel anti-windup scheme in a hdd-dual-stage servo-system. *IEEE/ASME Transactions on Mechatronics*, 9(3):580–592, Sep. 2004.

[21] H. R. Rapley and W. C. Messner. Designing controllers for two stage disk drive actuator systems using the pq method and the sbode plot. *IEEE Transactions on Magnetics*, 37(2):944–948, March 2001.

[22] U. Boettcher, B. Raeymaekers, R. A. de Callafon, and F. E. Talke. Dynamic modeling and control of a piezo-electric dual-stage tape servo actuator. *IEEE Transactions on Magnetics*, 45(7):3017–3024, July 2009.

[23] R. Oboe, A. Beghi, P. Capretta, and F. C. Soldavini. A simulation and control design environment for single-stage and dual-stage hard disk drives. *IEEE/ASME Transactions on Mechatronics*, 7(2):161–170, June 2002.

[24] Y. Choi and J. Jeong. A novel damping scheduling scheme for proximate time optimal servomechanisms in hard disk drives. *IEEE Transactions on Magnetics*, 42(3):468–472, March 2006.

[25] B. Hredzak, G. Herrmann, and G. Guo. A proximate-time-optimal-control design and its application to a hard disk drive dual-stage actuator system. *IEEE Transactions on Magnetics*, 42(6):1708–1715, June 2006.

[26] J. Zheng, M. Fu, Y. Wang, and C. Du. Nonlinear tracking control for a hard disk drive dual-stage actuator system. *IEEE/ASME Transactions on Mechatronics*, 13(5):510–518, Oct 2008.

[27] H. Li, C. Du, and Y. Wang. Optimal reset control for a dual-stage actuator system in hdds. *IEEE/ASME Transactions on Mechatronics*, 16(3):480–488, June 2011.

[28] R. A. de Callafon, R. Nagamune, and R. Horowitz. Robust dynamic modeling and control of dual-stage actuators. *IEEE Transactions on Magnetics*, 42(2):247–254, Feb 2006.

[29] T. B. Goh, , B. M. Chen, and and. Design and implementation of a hard disk drive servo system using robust and perfect tracking approach. *IEEE Transactions on Control Systems Technology*, 9(2):221–233, March 2001.

[30] C. Du and L. Xie. An improved mixed h/sub 2//h/sub /spl infin// control design for hard disk drives. *IEEE Transactions on Control Systems Technology*, 13(5):832–839, Sep. 2005.

[31] S. Lee and C. Chung. Active high-frequency vibration rejection in hard disk drives. *IEEE/ASME Transactions on Mechatronics*, 11(3):339–345, June 2006.

[32] C. S. Chang and T. S. Liu. Lqg controller for active vibration absorber in optical disk drive. *IEEE Transactions on Magnetics*, 43(2):799–801, Feb 2007.

[33] Y. Li, R. Horowitz, and R. Evans. Vibration control of a pzt actuated suspension dual-stage servo system using a pzt sensor. *IEEE Transactions on Magnetics*, 39(2):932–937, March 2003.

[34] Y. Chen and C. Fuh. Application of voice coil motors in active dynamic vibration absorbers. *IEEE Transactions on Magnetics*, 41(3):1149–1154, March 2005.

[35] J. Zheng and G. Guo. Identification and decentralized control of a dual-actuator hard disk drive system. *IEEE Transactions on Magnetics*, 41(9):2515–2521, Sep. 2005.

[36] M. Kobayashi and R. Horowitz. Track seek control for hard disk dual-stage servo systems. *IEEE Transactions on Magnetics*, 37(2):949–954, March 2001.

[37] C. W. Lee and S. M. Suh. Model prediction based dual-stage actuator control in discrete-time domain. *IEEE Transactions on Magnetics*, 47(7):1830–1836, July 2011.

[38] S. Hara, T. Hara, L. Yi, and M. Tomizuka. Novel reference signal generation for two-degree-of-freedom controllers for hard disk drives. *IEEE/ASME Transactions on Mechatronics*, 5(1):73–78, March 2000.

[39] Y. Li and R. Horowitz. Mechatronics of electrostatic microactuators for computer disk drive dual-stage servo systems. *IEEE/ASME Transactions on Mechatronics*, 6(2):111–121, June 2001.

[40] T. Yan and R. Lin. Experimental modeling and compensation of pivot nonlinearity in hard disk drives. *IEEE Transactions on Magnetics*, 39(2):1064–1069, March 2003.

[41] C. Du, L. Xie, and J. Zhang. Compensation of vcm actuator pivot friction based on an operator modeling method. *IEEE Transactions on Control Systems Technology*, 18(4):918–926, July 2010.

[42] G. Herrmann and S. S. Ge and. Practical implementation of a neural network controller in a hard disk drive. *IEEE Transactions on Control Systems Technology*, 13(1):146–154, Jan 2005.

[43] P. P. San, B. Ren, S. S. Ge, T. H. Lee, and J. Liu. Adaptive neural network control of hard disk drives with hysteresis friction nonlinearity. *IEEE Transactions on Control Systems Technology*, 19(2):351–358, March 2011.

[44] C. Y. Lai, F. L. Lewis, V. Venkataramanan, X. Ren, S. S. Ge, and T. Liew. Disturbance and friction compensations in hard disk drives using neural networks. *IEEE Transactions on Industrial Electronics*, 57(2):784–792, Feb 2010.

[45] C. Lin and H. Li. A novel adaptive wavelet fuzzy cerebellar model articulation control system design for voice coil motors. *IEEE Transactions on Industrial Electronics*, 59(4):2024–2033, April 2012.

[46] C. Lin and H. Li. Adaptive dynamic sliding-mode fuzzy cmac for voice coil motor using asymmetric gaussian membership function. *IEEE Transactions on Industrial Electronics*, 61(10):5662–5671, Oct 2014.

[47] C. Hsu and Y. Chen. Microcontroller-based b-spline neural position control for voice coil motors. *IEEE Transactions on Industrial Electronics*, 62(9):5644–5654, Sep. 2015.

[48] S. Chen and C. Lee. Digital signal processor based intelligent fractional-order sliding-mode control for a linear voice coil actuator. *IET Control Theory Applications*, 11(8):1282–1292, 2017.

[49] Liang-Liang Xie and Lei Guo. How much uncertainty can be dealt with by feedback? *IEEE Transactions on Automatic Control*, 45(12):2203–2217, 2000.

[50] H. Pan, W. Sun, H. Gao, and X. Jing. Disturbance observer-based adaptive tracking control with actuator saturation and its application. *IEEE Transactions on Automation Science and Engineering*, 13(2):868–875, 2016.

[51] Ian R. Petersen and Roberto Tempo. Robust control of uncertain systems: Classical results and recent developments. *Automatica*, 50(5):1315 – 1335, 2014.

[52] S. Li, J. Yang, W. Chen, and X. Chen. *Disturbance Observer Based Control Methods and Applications*. CRC Press, Taylor & Francis Group, 6000 Broken Sound Parkway NW, Suite 300 Boca Raton, 2016.

[53] W. Chen, J. Yang, L. Guo, and S. Li. Disturbance-observer-based control and related methods—an overview. *IEEE Transactions on Industrial Electronics*, 63(2):1083–1095, Feb 2016.

[54] B. Barmish and G. Leitmann. On ultimate boundedness control of uncertain systems in the absence of matching assumptions. *IEEE Transactions on Automatic Control*, 27(1):153–158, February 1982.

[55] K. Ohishi, M. Nakao, K. Ohnishi, and K. Miyachi. Microprocessor-controlled dc motor for load-insensitive position servo system. *IEEE Transactions on Industrial Electronics*, IE-34(1):44–49, 1987.

[56] Kiyoshi Ohishi, Kouhei Ohnishi, and Kunio Miyachi. Torque speed regulation of dc motor based on load torque estimation method. pages 1209 – 1218, Dec 1983.

[57] J. Han. From pid to active disturbance rejection control. *IEEE Transactions on Industrial Electronics*, 56(3):900–906, 2009.

[58] C. Johnson. Further study of the linear regulator with disturbances–the case of vector disturbances satisfying a linear differential equation. *IEEE Transactions on Automatic Control*, 15(2):222–228, 1970.

[59] Q. Zhong and A. Kuperman. Design of ude-based controllers from their two-degree-of-freedom nature. *International Journal of Robust and Nonlinear Control*, 21(17):1994–2008, 2011.

[60] J. She, M. Fang, Y. Ohyama, H. Hashimoto, and M. Wu. Improving disturbance-rejection performance based on an equivalent-input-disturbance approach. *IEEE Transactions on Industrial Electronics*, 55(1):380–389, 2008.

[61] Emre Sariyildiz and Kouhei Ohnishi. A Guide to Design Disturbance Observer. *Journal of Dynamic Systems, Measurement, and Control*, 136(2), 12 2013. 021011.

[62] Wen-Hua Chen, D. J. Ballance, P. J. Gawthrop, and J. O'Reilly. A nonlinear disturbance observer for robotic manipulators. *IEEE Transactions on Industrial Electronics*, 47(4):932–938, 2000.

[63] L. Jiang, Q. H. Wu, and J. Y. Wen. Decentralized nonlinear adaptive control for multimachine power systems via high-gain perturbation observer. *IEEE Transactions on Circuits and Systems I: Regular Papers*, 51(10):2052–2059, 2004.

[64] L. B. Freidovich and H. K. Khalil. Performance recovery of feedback-linearization-based designs. *IEEE Transactions on Automatic Control*, 53(10):2324–2334, 2008.

[65] L.Xing and H.Zhou. Research and application of voice coil actuator. *Micromotors*, 2011.

[66] S.Huang and Z.Feng. Parameter self-optimizing pid control for linear motor of the mf type. *Aviation Precision Manufacturing Technology*, 14(5), Oct 2005.

[67] T. Piatkowski. Dahl and lugre dynamic friction models-the analysis of selected properties. *Mechanism and Machine Theory*, 73:91 – 100, 2014.

[68] Péter Korondi. *Robot Applications*. BME-MOGI, 4-6 Bertalan Lajos Street, Budapest 1111, Hungary, 2014.

[69] W. Rong, S. Liang, L. Wang, S. Zhang, and W. Zhang. Model and control of a compact long-travel accurate-manipulation platform. *IEEE/ASME Transactions on Mechatronics*, 22(1):402–411, Feb 2017.

[70] T. Zhang, M. Tran, and H. Huang. Admittance shaping-based assistive control of sea-driven robotic hip exoskeleton. *IEEE/ASME Transactions on Mechatronics*, 24(4):1508–1519, Aug 2019.

[71] C. Canudas de Wit, H. Olsson, K. J. Astrom, and P. Lischinsky. A new model for control of systems with friction. *IEEE Transactions on Automatic Control*, 40(3):419–425, Mar 1995.

[72] S. Huang, W. Liang, and K. K. Tan. Intelligent friction compensation: A review. *IEEE/ASME Transactions on Mechatronics*, 24(4):1763–1774, Aug 2019.

[73] D. Aslan and Y. Altintas. Prediction of cutting forces in five-axis milling using feed drive current measurements. *IEEE/ASME Transactions on Mechatronics*, 23(2):833–844, April 2018.

[74] A. Yuen and Y. Altintas. Constrained trajectory generation and control for a 9-axis micromachining center with four redundant axes. *IEEE/ASME Transactions on Mechatronics*, 23(1):402–412, Feb 2018.

[75] Texas Instruments. *TMS320F2837xD Dual-Core Delfino Microcontrollers Technical Reference Manual*, December 2017.

[76] Texas Instruments. *LAUNCHXL-F28379D Overview User's Guide*, March 2019.

[77] Texas Instruments. *DRV8305 Three Phase Gate Driver With Current Shunt Amplifiers and Voltage Regulator*, February 2016.

[78] Texas Instruments. *BOOSTXL-DRV8305EVM User's Guide*, June 2017.

[79] MicroE System. *Mercury II 1600 The Next Generation of High Performance Encoders*, 2011. Rev. i.

[80] MicroE System. *Sensor Installation Manual and Reference Guide*, 2018. Rev. 180131.

[81] Texas Instruments. *AM26C32 Quadruple Differential Line Receiver datasheet*, October 2018.

[82] Jinan Yihua Tribology Testing Technology Co. Ltd. *User's Guide for MGW-001*, June 2017.

[83] Jinan Yihua Tribology Testing Technology Co. Ltd. *User's Guide for MXW-1*, August 2018.

[84] Texas Instruments. *Code Composer Studio User's Guide*, 2020.

[85] Texas Instruments. *controlSUITE Brochure Comprehensive. Intuitive. Optimized. Real-world software for real-time control.*, 2010.

[86] Texas Instruments. *C2000Ware Quick Start Guide*, Dec 2019.

[87] MathWorks. *Embedded Coder Support Package for Texas Instruments C2000 Processors User's Guide*, March 2020.

[88] MathWorks. *Embedded Coder Support Package for Texas Instruments C2000 Processors Reference*, March 2020.

[89] MathWorks. *Instrument Control Toolbox User's Guide*, March 2020.

[90] T. Glad and L. Ljung. *Control Theory Multivariable and Nonlinear Methods*. Taylor & Francis Group, 29 West 35th Street, New York, NY, 10001, 2000.

[91] D. N. Zmood and D. G. Holmes. Stationary frame current regulation of pwm inverters with zero steady-state error. *IEEE Transactions on Power Electronics*, 18(3):814–822, May 2003.

[92] S. Fukuda and T. Yoda. A novel current-tracking method for active filters based on a sinusoidal internal model [for pwm invertors]. *IEEE Transactions on Industry Applications*, 37(3):888–895, May 2001.

[93] S. C. Kuo. *Automatic Control Systems*. Prentice Hall, Upper Saddle River, NJ, USA, 1975.

[94] L. D. Flora and H. A. Grundling. Time domain sinusoidal acceleration controller for an electrodynamic shaker. *IET Control Theory Applications*, 2(12):1044–1053, December 2008.

[95] K.P.S. Rana. Fuzzy control of an electrodynamic shaker for automotive and aerospace vibration testing. *Expert Systems with Applications*, 38(9):11335 – 11346, 2011.

[96] K. Ohnishi, M. Shibata, and T. Murakami. Motion control for advanced mechatronics. *IEEE/ASME Transactions on Mechatronics*, 1(1):56–67, March 1996.

[97] A. Sabanovic and K. Ohnishi. *Motion Control Systems*. John Wiley & Sons (Asia) Pte Ltd, 2 Clementi Loop, 02-01, Singapore 129809, 2011.

[98] E. Sariyildiz, R. Oboe, and K. Ohnishi. Disturbance observer-based robust control and its applications: 35th anniversary overview. *IEEE Transactions on Industrial Electronics*, 67(3):2042–2053, March 2020.

[99] B. Gopinath. On the control of linear multiple input-output systems. *The Bell System Technical Journal*, 50(3):1063–1081, March 1971.

[100] V. Radisavljevic-Gajic. Full- and reduced-order linear observer implementations in matlabsimulink [lecture notes]. *IEEE Control Systems Magazine*, 35(5):91–101, Oct 2015.

[101] Robert Bickel and Masayoshi Tomizuka. Passivity-Based Versus Disturbance Observer Based Robot Control: Equivalence and Stability. *Journal of Dynamic Systems, Measurement, and Control*, 121(1):41–47, 03 1999.

[102] E. Sariyildiz, H. Sekiguchi, T. Nozaki, B. Ugurlu, and K. Ohnishi. A stability analysis for the acceleration-based robust position control of robot manipulators via disturbance observer. *IEEE/ASME Transactions on Mechatronics*, 23(5):2369–2378, Oct 2018.

[103] M. Elkayam, S. Kolesnik, and A. Kuperman. Guidelines to classical frequency-domain disturbance observer redesign for enhanced rejection of periodic uncertainties and disturbances. *IEEE Transactions on Power Electronics*, 34(4):3986–3995, April 2019.

[104] B.A. Francis and W.M. Wonham. The internal model principle of control theory. *Automatica*, 12(5):457–465, March 1976.

[105] Julius O. Smith. *Spectral Audio Signal Processing*. `http://-ccrma.stanford.edu/~jos/sasp/`, accessed ¡date¿. online book, 2011 edition.

[106] W.Cauer. Artificial network, May 1934. US Patent 1,958,742.

[107] W.Cauer. Electric wave filter, January 1935. US Patent 1,989,545.

[108] W.Cauer. Unsymmetrical electric wave filter, July 1936. US Patent 2,048,426.

[109] S. Mneney. *An Introduction to Digital Signal Processing: A Focus on Implementation*. River Publishers, PO box 1657, Algade 42, 9000 Aalborg, Denmark, 2008.

[110] D. Elliott. *Handbook of Digital Signal Processing Engineering Applications*. Academic Press, INC, 24-28 Oval Road, London, NW1 7DX, 1987.

[111] S. Y. Gadelovits, Q. Zhong, V. Kadirkamanathan, and A. Kuperman. Ude-based controller equipped with a multi-band-stop filter to improve the voltage quality of inverters. *IEEE Transactions on Industrial Electronics*, 64(9):7433–7443, Sep. 2017.

[112] S. Butterworth. On the theory of filter amplifiers. *Experimental Wireless and the Wireless Engineer*, 7(4):536–541, May 1930.

[113] I. Aharon, D. Shmilovitz, and A. Kuperman. Uncertainty and disturbance estimator-based controllers design under finite control bandwidth constraint. *IEEE Transactions on Industrial Electronics*, 65(2):1439–1449, 2018.

[114] I. Aharon, D. Shmilovitz, and A. Kuperman. Phase margin oriented design and analysis of ude-based controllers under actuator constraints. *IEEE Transactions on Industrial Electronics*, 65(10):8133–8141, 2018.

[115] P. Rehbein and J. Wallaschek. Friction and wear behaviour of polymer/steel and alumina/alumina under high-frequency fretting conditions. *Wear*, 216(2):97 – 105, 1998.

[116] K. Elliott. *Modern Control Engineering*. Prentice Hall, One Lake Street, Upper Saddle River, New Jersey 07458, 2010.

[117] Y. Joo, G. Park, J. Back, and H. Shim. Embedding internal model in disturbance observer with robust stability. *IEEE Transactions on Automatic Control*, 61(10):3128–3133, 2016.

[118] L. F. A. Pereira, J. V. Flores, G. Bonan, D. F. Coutinho, and J. M. G. da Silva. Multiple resonant controllers for uninterruptible power supplies—a systematic robust control design approach. *IEEE Transactions on Industrial Electronics*, 61(3):1528–1538, 2014.